NTNU – Trondheim
Norwegian University of
Science and Technology

Numerical Simulations of Docol 600 DL Steel Plates Subject to Blast Loading

Kristoffer H Andersen
Fredrik Børsum Hernandez

Civil and Environmental Engineering
Submission date: June 2013
Supervisor: Tore Børvik, KT
Co-supervisor: Vegard Aune, KT
Knut G. Rakvåg, KT

Norwegian University of Science and Technology
Department of Structural Engineering

Department of Structural Engineering
Faculty of Engineering Science and Technology
NTNU- Norwegian University of Science and Technology

ACCESSIBILITY

OPEN

MASTER THESIS 2013

SUBJECT AREA: Computational Mechanics	DATE: 10 June 2013	NO. OF PAGES: 228 14 + 186 + 28

TITLE:

Numerical Simulations of Docol 600 DL Steel Plates Subject to Blast Loading

Numeriske Simuleringer av Docol 600 DL Stålplater Utsatt for Eksplosjonslast

BY:

Kristoffer Hunnestad Andersen
Fredrik Børsum Hernandez

SUMMARY:
The main objective in this study was to investigate how the deformation of Docol 600 DL steel plates subject to blast loading can be accurately recreated with different numerical simulations. An initial experiment was undertaken employing a gas gun to simulate the blast loads. The experiments failed to properly emulate a proper blast load, but the experiment served as an initial benchmark for calibration of the numerical models.

Focus shifted on to simulating experiments performed at Raufoss in 2010 by Rakvåg. Experiments on quadratic 400mm by 400mm, 2mm thick Docol 600 DL steel plates were performed for standoffs at 300mm, 400mm, 450mm and 550mm. Material models for the steel plates were determined from previous work done at SIMLab.

Numerical simulations in LS-DYNA and IMPETUS were utilized with a pure Lagrangian approach, an uncoupled Eulerian-Lagrangian approach, a coupled Eulerian-Lagrangian and a discrete particle method. The pure Lagrangian simulations were based on data from the CONWEP standard, thus it failed to properly describe the charge geometry and consequently misrepresented the properties of the blast load. The uncoupled and coupled Eulerian-Lagrangian simulations properly described the charge geometry, but a requirement of a sufficiently fine discretization of the Eulerian mesh rendered full 3D simulations with a high computational demand. A 2D to 3D mapping technique in the Eulerian domain was successfully completed to reduce the computational time. The discrete particle approach yielded the most accurate results while being the easiest to define numerically.

Employing the different numerical techniques revealed that the main source of error in recreating expected deformation lies in the capability of properly describing the blast load conditions.

RESPONSIBLE TEACHER: Professor Tore Børvik

SUPERVISOR(S): Professor Tore Børvik, PhDc Vegard Aune and PhDc Knut Rakvåg

CARRIED OUT AT: SIMLab, Department of Structural Engineering, NTNU

Institutt for konstruksjonsteknikk
Fakultet for ingeniørvitenskap og teknologi
NTNU- Norges teknisk- naturvitenskapelige universitet

TILGJENGELIGHET

ÅPEN

MASTEROPPGAVE 2013

FAGOMRÅDE:	DATO:	ANTALL SIDER: 228
Beregningsmekanikk	10 Juni 2013	14 + 186 + 28

TITTEL:

Numeriske Simuleringer av Docol 600 DL Stålplater Utsatt for Eksplosjonslast

Numerical Simulations of Docol 600 DL Steel Plates Subject to Blast Loading

UTFØRT AV:

Kristoffer Hunnestad Andersen
Fredrik Børsum Hernandez

SAMMENDRAG:

Hensikten med denne oppgaven var å undersøke hvordan deformasjonen av Docol 600 DL stålplater utsatt for eksplosjonslast kan bli nøyaktig gjenskapt ved bruk av forskjellige numeriske teknikker. Et innledende forsøk ble gjennomført ved bruk av en gasskanon til å simulere eksplosjonslast. Forsøkene var mislykket i den forstand at de ikke klarte å gjenskape et realistisk lastbilde, men eksperimentene ble brukt for å kalibrere den numeriske modellen.

Fokuset ble flyttet til simulering av eksperimenter gjennomført på Raufoss i 2010 av Rakvåg. Eksperimentene ble gjennomført på kvadratiske 400mm x 400mm, 0,7mm tykke Docol 600 DL stålplater med en avstand til eksplosivene på 300mm, 400mm, 450mm og 550mm. Materialmodell for stålet ble bestemt fra tidligere arbeider gjort ved SIMLab.

Numeriske simuleringer i LS-DYNA og IMPETUS ble brukt for å simulere oppførselen av stålplatene med med en ren Lagrange teknikk, en ukoblet Euler-Lagrange metode, koblede Euler-Lagrange simuleringer og en diskret partikkelmetode. De rene Lagrangeanalysene ble basert på data fra CONWEP, og feilet dermed på å beskrive geometrien på eksplosivene og feilaktig representerte derfor eksplosjonslasten. De ukoblede og koblede analysene beskrev geometrien av eksplosivene nøyaktig, men et krav om en fin diskretisering av Euler-domene førte til økt behov for datakraft. En vellykket 2D til 3D kartlegging av løsningsvariable i Euler-domenet ble gjennomført for å redusere regnetiden. Partikkelmetoden ga de mest nøyaktige resultatene samtidig som den var den enkleste å ta i bruk.

Ved å gjøre simuleringer med de ulike numeriske metodene kom det fram at den største feilkilden ved å gjenskape opplevd komponentoppførsel lå i å definere lastparameterene fra eksplosjonslasten nøyaktig.

FAGLÆRER: Professor Tore Børvik

VEILEDER(E): Professor Tore Børvik, PhDc Vegard Aune og PhDc Knut Rakvåg

UTFØRT VED: SIMLab, Institutt for konstruksjonsteknikk, NTNU.

Department of Structural Engineering
FACULTY OF ENGINEERING SCIENCE AND TECHNOLOGY
NTNU – Norwegian University of Science and Technology

MASTER'S THESIS 2013
for
Kristoffer Hunnestad Andersen and Fredrik Børsum Hernandez

Numerical Simulations of Docol 600 DL Steel Plates Subject to Blast Loading

The main objective in this study is to investigate how the deformation of Docol 600 DL steel plates can be accurately recreated with different numerical simulations. Both experimental and numerical studies are to be carried out.

The main topics in this research project will be as follows:

1. A study of current literature: The blast load phenomena, blast load design, finite element theory, fluid-structure interaction, the numerical implementation of arbitrary Lagrangian-Eulerian finite element analysis, material models and the discrete particle method.
2. Laboratory experiments: A gas-cannon at SIMLab is to be employed for testing the deformation of Docol 600 DL steel plates subject to blast loading. Experimental data is also to be reported from experiments performed at Raufoss in 2010.
3. Material experiments: Necessary material data sufficient for numerical analyses is to be acquired from performed material experiments performed at SIMLab.
4. Numerical analyses: Non-linear finite element numerical simulations of the experiments at NTNU and the experiments at Raufoss are to be performed. The numerical simulation techniques employed should contain a Lagrangian approach, an uncoupled Lagrangian-Eulerian approach, a coupled Lagrangian-Eulerian approach and the discrete particle method.
5. Validation and documentation: The simulations are to be compared against the available experimental data extracted from the experiments.

This thesis must be written according to current requirements and submitted to the Department of Structural Engineering, NTNU, no later than June 10th, 2013

Supervisors: Professor Tore Børvik, PhDc Vegard Aune and PhDc Knut G. Rakvåg NTNU, January 14th, 2013

Tore Børvik
Professor

Acknowledgements

This thesis is written for the Structural Impact Laboratory (SIMLab) at the Norwegian University of Science and Technology (NTNU) during our tenth and last semester. This thesis is written in collaboration with the Norwegian Defence Estates Agency (NDEA) represented by our councilor Tore Børvik. SIMLab works on developing methods and tools for the virtual product development of structures exposed to impact and collisions. The Structural Impact Laboratory is a Center for Research-based Innovation (CRI) appointed by the Research Council of Norway. CRI-SIMLab's main objective is to develop a technology platform for safe and cost effective structures in aluminium, high-strength steels and polymers through advances in research areas such as materials, solution techniques and structures. Its research partners include the Dept. of Structural Engineering at NTNU, the Dept of Material Science and Engineering at NTNU and SINTEF. SIMLab have a close collaboration with its Industrial partners that include Hydro Aluminium, Renault, Audi, Statoil, SSAB Swedish Steel, BMW, Toyota Motor Europe and Benteler Aluminium Systems and its public partners; the Norwegian Defence Estates Agency and the Norwegian Public Roads Administration.

Working on this thesis have offered a great educational experience, and a chance for us to employ the knowledge we have acquired during our five years here at NTNU. It have been an enjoyable task, but at times both frustrating and hectic.

We would like to thank our project supervisors Professor Tore Børvik, PhDc Vegard Aune and PhDc Knut Gaarder Rakvåg at SIMLab for guidance and the invaluable assistance during these twenty weeks. They have provided us with the necessary theoretical background and critique during weekly sessions

We would also like to thank Dr. Ing Torodd Berstad and Dr. David Morin for assistance with LS-DYNA, Dr. Lars Olovsson and the staff at IMPETUS Afea for guidance and an excellent course in their finite element software, Hilde Stakvik Eide, Emil Arne Melby and Trond Auestad for assistance with the experiments and PhDc Lauren Stewart at the University of California, San Diego for providing us with a good theoretical background through the course SE207 Introduction to Blast Loading and Design.

Lastly we would like to thank Simen Hellgren Holtberget who has endured our countless discussions in the office, Remi André Kjørlaug for assistance with

LATEX and our friends who have offered their critique and thoughts.

Trondheim, 10 Juni, 2013.

Kristoffer H. Andersen Fredrik Hernandez

Kristoffer Hunnestad Andersen Fredrik Børsum Hernandez

Abstract

The main objective in this study was to investigate how the deformation of Docol 600 DL steel plates subject to blast loading can be accurately recreated with different numerical simulations. An initial experiment was undertaken employing a gas gun to simulate the blast loads. The experiments failed to properly emulate a proper blast load, but the experiment served as an initial benchmark for calibration of the numerical models.

Focus shifted on to simulating experiments performed at Raufoss in 2010 by Rakvåg. Experiments on quadratic 400mm by 400mm, 2mm thick Docol 600 DL steel plates were performed for standoffs at 300mm, 400mm, 450mm and 550mm. Material models for the steel plates were determined from previous work done at SIMLab.

Numerical simulations in LS-DYNA and IMPETUS were utilized with a pure Lagrangian approach, an uncoupled Eulerian-Lagrangian approach, a coupled Eulerian-Lagrangian and a discrete particle method. The pure Lagrangian simulations were based on data from the CONWEP standard, thus it failed to properly describe the charge geometry and consequently misrepresented the properties of the blast load. The uncoupled and coupled Eulerian-Lagrangian simulations properly described the charge geometry, but a requirement of a sufficiently fine discretization of the Eulerian mesh rendered full 3D simulations with a high computational demand. A 2D to 3D mapping technique in the Eulerian domain was successfully completed to reduce the computational time. The discrete particle approach yielded the most accurate results while being the easiest to define numerically.

Employing the different numerical techniques revealed that the main source of error in recreating expected deformation lies in the capability of properly describing the blast load conditions.

Contents

Nomenclature

ALE	Arbitrary Lagrangian-Eulerian
CEL	Coupled Eulerian Lagrangian
CL	Cockroft-Latham fracture criterion
CRI	Center for Research-based Innovation
DIC	Digital Image Correlation
EOS	Equation Of State
FEA	Finite Element Analysis
FSI	Fluid Structure Interaction
HE	High explosives
IED	Improvised Explosive Devices
JC	Johnson-Cook material model
MDOF	Multi Degree Of Freedom system
MME	Multi-Material Eulerian
MPP	Massively Parallel Processing
NDEA	Norwegian Defence Estates Agency
PDE	Partial Differential Equations
SIMLab	Structural Impact Laboratory
SMP	Symmetric Multiprocessing
UEL	Uncoupled Eulerian Lagrangian
α	Angle of incidence (Blast design)
α	Thermal expansion coefficient (Material parameter)
$\boldsymbol{\chi}$	ALE coordinates
$\boldsymbol{D}, \boldsymbol{R^{int}}, \boldsymbol{R^{ext}}$	Displacement, internal force and external force vector

$\boldsymbol{F}$	Deformation gradient
$\boldsymbol{M}, \boldsymbol{C}, \boldsymbol{K}$	Mass, damping and stiffness matrix
$\boldsymbol{u}$	Material point displacement
$\boldsymbol{X}$	Material coordinates
χ	Taylor-Quinnery coefficient
Δt	Time step
Δt_{cr}	Stable time increment
Δx^e	Characteristic length of an element
Δ_{exp}	Permanent center plate-deflection in experiment
Δ_{max}	Maximum center plate-deflection in numerical simulation
Δ_{perm}	Permanent center plate-deflection in numerical simulation
$\dot{\epsilon}$	Strain-rate
$\dot{\epsilon}_{0p}$	Reference strain-rate
ϵ^e, ϵ^p	Elastic and plastic strain
ϵ_{eq}	Equivalent plastic strain
$\frac{Df}{Dt}$	Material time derivative
γ	Ratio between C_p and C_v
$\hat{\Omega}$	ALE referential domain
$\hat{u}, \hat{v}, \hat{a}$	Mesh displacement, velocity and acceleration
$\{\boldsymbol{\alpha}\}$	Vector describing kinematic hardening
$\{\boldsymbol{\sigma}\}$	Total stress vector
$\{\boldsymbol{D}\}, \left\{\dot{\boldsymbol{D}}\right\}, \left\{\ddot{\boldsymbol{D}}\right\}$	Displacement, velocity and acceleration vector
$\{d\boldsymbol{\epsilon}^{\boldsymbol{e}}\}$	Elastic strain increment vector

$\{d\boldsymbol{\epsilon}^{\boldsymbol{p}}\}$	Plastic strain increment vector
$\{d\boldsymbol{\epsilon}\}$	Total strain increment vector
$\Omega_0, \Omega, \Gamma_0, \Gamma$	Reference and current configuration and respective boundaries
ω_{max}	Maximum system eigenfrequency
$\phi^n_{j+\frac{1}{2}}(x)$	Interpolation function
$\phi\,(X,t)$	Function describing motion or deformation of body
ρ	Density of the flow medium
σ	Cauchy stress tensor
σ_0	Yield stress
σ_{eq}	Equivalent stress
θ	Temperature
a_0	Speed of sound in surrounding fluid
a_j	Convective velocity or the velocity of the contact discontinuity at node j
b	Body force (Constitutive equations)
b	Decay coefficient (Friedlander equation)
c	Convective velocity
C_d	Dilatational wave speed in the material
C_p, C_v	Specific heat capacity at constant pressure and volume
$C_{r\alpha}$	Reflection coefficient, function of P_{so} and the angle of incidence α
D	Rate of deformation, the velocity strain $D = \mathrm{sym}(\nabla v)$
$d, \dot{d}, \ddot{d}$	Displacement, velocity and acceleration
F	Yield function

f_j^{ϕ}	Flux or the so-called transport volume of between two adjacent elements
i_s^+, i_s^-	Positive and negative specific impulse
$i_{r,exp}, i_{so,exp}$	Reflected and side-on impulse from the experiment
i_r, i_{so}	Reflected and side-on impulse
J	The determinant of the Jacobian between spatial and material coordinates
k	Thermal conductivity of the material
L^e	Characteristic length of the smallest element
M	Molar mass
M_s	Ratio between shock front velocity U and a_0
n	Number of molecules
N_p	Number of particles used in IMPETUS
P	Nominal stress (the transpose of the first Piola-Kirchoff stress)
P	Pressure
P_r, P_{so}	Peak reflected and side-on pressure
$P_{r,exp}, P_{so,exp}$	Peak reflected and side-on pressure from the experiment
P_{so}^+, P_{so}^-	Positive and negative phase peak side-on pressure
$P_{stat}, P_{dyn}, P_{stag}$	Static, dynamic and stagnant Pressure
q	Collection of internal variables in the constitutive model
Q_i, C_i	Material parameters in Voce
Q_{EXP}	Detonation heat of the explosive in questions. (found in the UFC)
Q_{TNT}	Detonation heat (found in the UFC)

R	Standoff distance (Blast parameter)
R	Universal gas constant (gas physics)
r_p	Molecular radius
S	Second Piola-Kirchhoff (PK2) stress
s	Specific heat source term
T	Absolute temperature
T^+, T^-	Duration of positive and negative phase of a blast wave
t_a	Arrival time of a blast wave
U	Flow velocity
V	Volume
v	Velocity field
v_{rms}	Root-mean-square acceleration
w	The hyperelastic potential of the reference configuration
W_p	Scalar describing the isotropic hardening
W_{cr}	The critical value of the plastic work per unit volume until fracture
W_{EXP}	Weight of the explosive subject to comparison
W_k	Total translational kinetic energy of all the molecules in the system
w_k	Specific translational kinetic energy per unit volume
W_{TNT}	TNT equivalent weight
Z	Scaled distance
A,B,C,m,n	Material constants in JC

Chapter 1

Introduction

Accidental explosions or terrorist attacks serves as a serious reminder of how devastating a blast load scenario can become in account of the loss of civilian lives and structural failure. International peace-keeping operations deal with the explosion phenomena on a daily basis and it is evident that protection against such incidents is of uttermost importance.

Traditionally protective buildings are made out of concrete that is able to withstand enormous blast loads and a wide variety of weaponry. A big drawback of the concrete-based protective system is the massive weight that makes it more or less stationary and ill-suited for mobile systems. This has sparked an interest in developing light-weight protective structural components such as thin steel and aluminium plates and panels.

Previous work on typical blast load scenarios have been done in abundance. This is mainly driven by the military industry that possesses large available resources. The problem with carrying out a full scale explosive test is the limited value of the results as the experiment specimen often is destroyed together with the testing equipment. The focus has therefore shifted from live experiments to numerical simulations, both for the reduced cost and the quality of the output data that becomes available. The affordability of computing power today allows engineers to use numerical simulations to predict the ultimate loads and deformations of structural components with great accuracy. However, the numerical simulations mainly done by the finite element codes require the physics behind the problem to be properly defined. The highly complicated physical processes behind the problems have led to a variety of different numerical techniques for simulating blast loads ranging from applying simple pressure loads to fully coupled gas-structure interaction-simulations and discrete particle-based approaches. The choice of what type of simulation to choose for a particular problem will rely on several questions; how accurate does the result of the simulation have to be? Is the benefit of a complicated simulation enough to offset the increased computational time and added risk of user errors? How accurate are the advanced numerical simulations compared to the simple ones?

Numerical simulations of blast load scenarios are well investigated in research articles and are the subject of several theses. The papers by Alia and Souli [2] and Chafi et. al [16] investigated the multi-material Eulerian approach and its applicability to describe air-blasts, whereas the results showed a good agreement between numerical and experimental data. A comparison between the coupled Eulerian-Lagrangian (CEL) formulation and particle method was performed by Olovsson et. al in [42], which indicated that the particle method is a viable alternative to describe fluid behaviour to the already established continuum-based approaches. A study on the effects of fluid-structure interaction (FSI) employing the CEL technique was performed by Subramaniam et. al in [52]. In this study it was observed that the FSI effects becomes insignificant when the ratio between structural velocity and particle velocity of the incident blast pressure wave starts approaching zero. Another study on FSI effects performed by Nian et. al [38] indicated that the differences between including and not including FSI diminishes in cases of structures with large stiffness and/or large mass.

This introduction will not try to give a review of all the previous work that has been done, but rather highlight some of the more relevant work related to this thesis performed at SIMLab. In his 2009 thesis, Rakvåg [44] investigated the combined blast and fragment loading on steel plates. In 2011, Hallset and Haagenruud [27] continued some of this work, further investigating the effects of blast loading on perforated plates. Both these theses involved advanced fully coupled Eulerian-Lagrangian simulations with successful results. Other studies performed by Børvik et. al [13] investigated the differences between a Pure Lagrangian, an uncoupled Eulerian-Lagrangian and a coupled Eulerian-Lagrangian approach to recreate a blast load scenario. The study showed that even though some of the analyses were more complex, they did not necessary provide more accurate results when compared to full scale experiments.

This thesis will focus on the numerical simulations of lightweight steel plates that are subject to blast loads. A collection of different approaches and numerical simulations will be employed to investigate what simulation techniques that is best-suited in respect of accuracy, computational effort and user-friendliness to recreate a specified blast load scenario.

A short overview of each chapter is presented below.

Chapter 2 - Theory. Relevant theory to this study, including: explosives, blast physics and mathematical treatment, pressure, blast design and reflection effects, material model and parameters, numerical methods, Lagrangian FEA, Eulerian FEA, Arbitrary Lagrangian-Eulerian (ALE) FEA and the discrete particle method.

Chapter 3 - Materials. Material parameters and how they are determined for the forthcoming numerical analyses are presented.

Chapter 4 - Experimental Work. Description and procedure of the experiments performed on the steel plates. Both the experiments at NTNU and the experiments at Raufoss are presented.

Chapter 5 - Experimental Results. The results of the different experiments described in chapter 4 are presented and processed.

Chapter 6 - Preliminary Numerical Study. A mesh sensitivity study for the forthcoming numerical simulations is completed. A cross platform validation between LS-DYNA and IMPETUS are performed together with a calibration of numerical parameters for the multi-material Eulerian analyses.

Chapter 7 - Numerical Methods. Numerical simulations of the different blast load scenarios are performed with a range of different techniques including a pure Lagrangian approach, a multi-material Eulerian formulation, an uncoupled Eulerian-Lagrangian simulation, a coupled Eulerian-Lagrangian simulation and a particle based approach.

Chapter 8 - Comparison and Discussion of Numerical Results. Comparison of the results from the simulations performed in the previous chapter is presented. Further discussion and critique of the different numerical techniques.

Chapter 9 - Concluding Remarks. Summary of results and conclusions.

Chapter 10 - Further Work. Recommended work to further investigate the challenges encountered in this thesis.

Chapter 2

Theory

2.1 The Blast Phenomenon

In this section the theory behind blast physics and explosives is presented.

2.1.1 Explosives

Explosive threats can be divided in to five main categories [51]:

- Military Weapons
- Improvised Explosive Devices (IED)
- Terrorist Threats
- Accidental Explosions
- Advanced Explosives

Millitary Weapons and IEDs are often used in combat situations where there is a lack of a controlled environment. They range from general purpose bombs to fragmentation and penetration bombs. The effect and usage of these depend primarily on the target and the desired effect. The terrorist threats can range from package type bombs to vehicle-borne suicide bombs.

There are an abundance of different types of high explosives (HE). Different types of explosives are compared by converting to a TNT-equivalent mass by employing a ratio of explosive-specific energies. These ratios are determined from a series of empirical testing and are therefore somewhat approximate [51]. Table 2.1 shows the TNT equivalent factors for different explosives.

Table 2.1: Explosives characteristics [51]

Explosive	TNT eqv. mass
Liquid Nitroglycerin	1.481
Pentolite	1.400
C-4	1.190-1.370
HMX	1.256
Semtex	1.250
RDX	1.185
Comp B (0.6RDX, 0.4TNT)	1.148
TNT	1.000
Blasting Gel	1.000
Dynamite	0.900
ANFO (94 % ammoniumnitrate, 6% fuel oil)	0.870
60% nitroglycerin dynamite	0.600

2.1.2 Blast Physics

The more general term explosion is defined by [5] as an event undergoing a rapid chemical or nuclear reaction with the production of noise, heat, and violent expansion of gases. Further, [10] defines an explosion as a process where combustion of a premixed gas cloud is causing a rapid increase of pressure. This increase in pressure can originate from nuclear reactions, HE, loss of containment in containers with high pressure and several others sources. It is evident that the keyword rapid is a determining factor.

2.1.2.1 The Explosive Process

For HE, the explosive process can typically be broken down in to 5 sub-events [50].

Initiation	The explosion reaction, often referred to as the combustion phase, generates a hot gas at a high pressure.
Expansion	The surrounding air is forced out of the volume it occupies. The layer of air surrounding the gaseous products is compressed. The expelled layer contains most of the energy released by the explosion.

Disequilibrium	Disequilibrium is created between the compressed air inside the blast wave and the air in front of it, this causes the blast wave to move outwards from the center of the explosion. The pressure decreases as the wavefront travels further from the explosive source.
Suction	The momentum of the gas causes it to over-expand, resulting in the pressure to often fall below atmospheric. The negative phase applies a decelerating force on the surrounding gas molecules, resulting in a reversal of flow back towards the center.
Equilibrium	Eventually, equilibrium is restored.

2.1.2.2 The Blast Wave

During the expansion phase of an explosive process, the blast wave is exerted from the source. The term blast wave includes both sonic compression waves, shock waves and rarefaction waves [10]. The waves have quite different characteristics and are illustrated in figure 2.1.

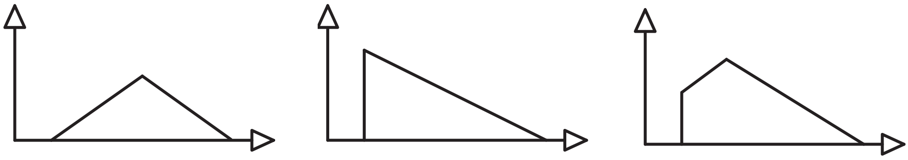

(a) Sonic compression - rarefaction wave

(b) Shock - rarefaction wave

(c) Shock - sonic compression - rarefaction wave

Figure 2.1: Type of waves

What kind of blast wave that is created from a specified explosion depends primarily on two factors; what type of explosions are present (how is the energy released from the explosive) and the distance from the explosive source. For strong explosions, a shock wave followed by a rarefaction wave as illustrated in figure 2.1b is typical. Usually for weak explosions, a sonic compression wave followed by a rarefaction wave is the most common (figure 2.1a) [10].

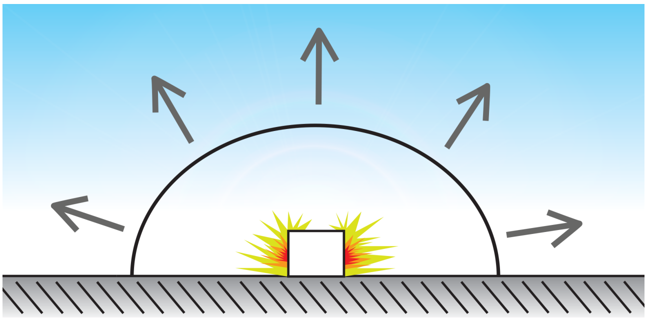

Figure 2.2: Blast wave moving outwards from the source

In studying air blast theory, one should become accustomed to thinking about a blast wave as a degenerate shock wave rather than describing a blast wave as a strong acoustic wave. One should be aware of the following notions of whom none of them are consistent with acoustic theory [4]:

- Of waves moving faster than sound.
- Of finite large pressure, density and temperature changes.
- Of finite particle velocities associated with the waves.
- Of wave fronts across which changes in various blast parameters are so rapid they are usually considered discontinuous ”jump” conditions.

Regardless of the source of the initial disturbance, the compressibility of air will lead to a creation of an almost discontinuous ”shock-up” of pressure, temperature and density. The resulting shock-front moves supersonically and the transmission of blast waves in air is therefore described as a non-linear process involving non-linear equations of motion [4].

The idealized blast wave is produced from a spherical symmetric source, such that the properties of the blast wave are only functions of the distance from the charge itself and the time elapsed since detonation. An ideal pressure gauge which in no way interferes with the blast follows all points of variations in pressure records the history of absolute pressure at a fixed distance R. Such conditions would produce the following pressure time history [4]:

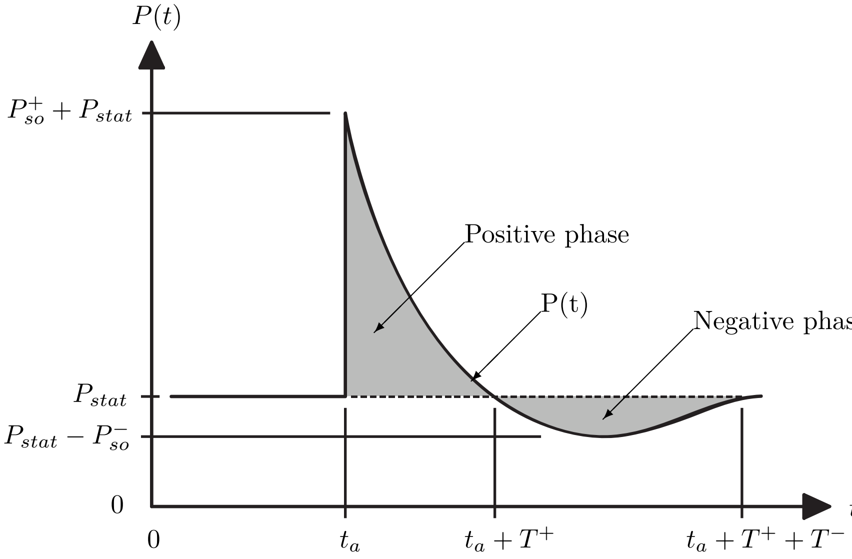

Figure 2.3: Idealized blast wave [4]

Where P_{so}^{+} is the positive peak side-on pressure, P_{so}^{-} is the negative peak side-on pressure, t_a is the arrival time, T^{+} is the duration of the positive phase and T^{-} is the duration of the negative phase. P_{stat} is the static pressure.

Various representation of this curve on an continuous form is presented in [10] and [50]. For practical design purposes, the shape is usually taken as a triangle with the negative phase being neglected. The most commonly used approximation to describe a pressure time-history on a continuous format is the Friedlander Equation [10, 50]:

$$P\left(t\right) = P_{stat} + P_{so}^{+}\left(1 - \frac{t}{T^{+}}\right)e^{\frac{-bt}{T^{+}}} \tag{2.1}$$

Where the decay coefficient b must be determined from empirical testing. Note that the Friedlander equation does not neglect the negative phase.

2.1.2.3 Impulse

The specific impulse is defined as:

$$i_s^+ = \int\limits_{t_a}^{t_a+T^+} [P\,(t) - P_{stat}]dt \tag{2.2}$$

$$i_s^- = \int\limits_{t_a+T^+}^{t_a+T^++T^-} [P\,(t) - P_{stat}]dt \tag{2.3}$$

Where i_s^+ is the positive specific impulse and i_s^- is the negative specific impulse. The different impulses are illustrated in figure 2.4.

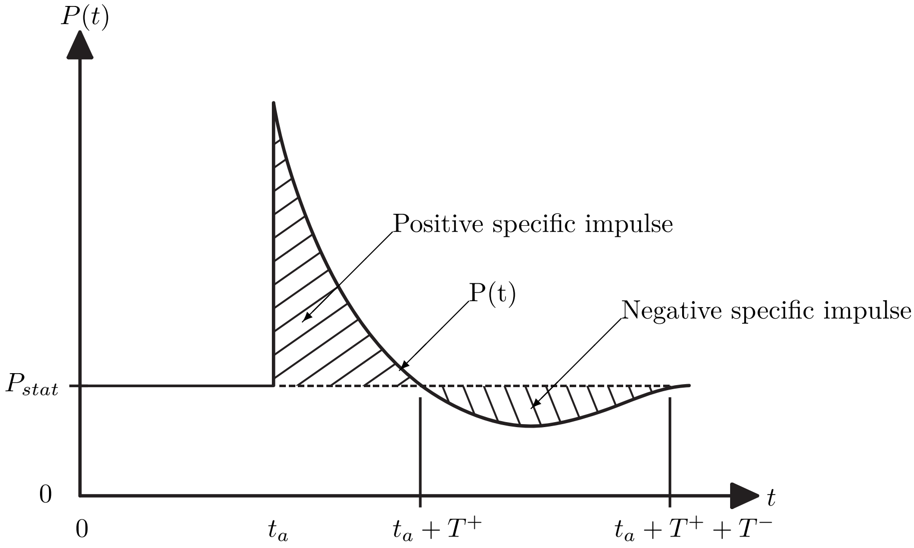

Figure 2.4: Impulse [4]

In classical mechanics, impulse is the integral of force with respect to time. When blasts are considered, the specific impulse is the integral of pressure with respect to time, but is simply referred to as the impulse.

2.1.2.4 Pressure

The pressure increase produced by the passing of a blast wave needs to be accurately represented and described. In fluid dynamics, it is often referred to different types of pressures with the terms static pressure P_{stat}, dynamic pressure P_{dyn} and stagnation pressure P_{stag} [10]. The static pressure is what we often refer to as the atmospheric pressure or the constant pressure present at the blast site. The dynamic pressure is the pressure increase that we attribute to the blast wave. The dynamic pressure can also be expressed as follows:

$$P_{dyn} = \frac{\rho U^2}{2} \tag{2.4}$$

Where ρ is the density of the flow medium and U is the flow velocity. The stagnation pressure is the sum of the dynamic pressure and the static pressure

$$P_{stag} = P_{stat} + P_{dyn} \tag{2.5}$$

When the blast wave passes a point, we have two different types of pressures present. The side-on pressure P_{so} is the pressure measured perpendicular to the propagation of the blast wave, and the reflected pressure P_r is measured parallel to propagation direction in the opposite direction of the direction of movement. The two different type of pressure are illustrated in figure 2.5.

Because of the connection between the wavefront velocity U to the pressure increase produced by a blast in equation (2.4), studies have been carried out to find empirical correlations between U and P_{so}. The most widely used in the US military are the equations derived by Rankine & Hugoniot for blast waves at room temperature. The P_{so} can be calculated from [49, 21].

$$\frac{P_{so}}{P_{stat}} = \frac{2\gamma {M_s}^2 - (\gamma - 1)}{\gamma + 1} \tag{2.6}$$

Where γ is the ratio between the specific heat capacities at constant pressure C_p and the specific heat capacity at constant volume C_v respectively $\gamma = \frac{C_p}{C_v}$. M_s is the ratio between the velocity of the shock front U and the speed of sound in the surrounding fluid a_0, $M_s = \frac{U}{a_0}$. For normal atmospheric conditions; $\gamma = 1.4$. This leads to the following equation:

$$U = \sqrt{\left(\frac{6P_{so} + 7P_{stat}}{7P_{stat}}\right)} a_0 \tag{2.7}$$

Where U is the wavefront velocity, P_{so} is the side-on pressure and P_{stat} is the static pressure. This can further be derived in to an equation for the expected peak dynamic pressure P_{dyn} [49, 21].

$$P_{dyn} = \frac{5P_{so}^2}{2\left(P_{so} + 7P_{stat}\right)} \tag{2.8}$$

An upper limit to the applied blast load is obtained if the surface it hits head on is infinitely rigid [4]. All flow behind the wave is stopped and the pressures are considerably larger compared to the side-on pressure. For shock waves weak enough that air behaves as a perfect gas, there is derived a relation between the peak reflected pressure P_r and the peak side-on pressure P_{so}:

$$\bar{P}_r = 2\bar{P}_{so} + \frac{\left(\gamma + 1\right)\bar{P}_{so}^2}{\left(\gamma - 1\right)\bar{P}_{so} + 2\gamma} \tag{2.9}$$

$$\bar{P}_r = \frac{P_r}{P_{stat}} \tag{2.10}$$

$$\bar{P}_{so} = \frac{P_{so}}{P_{stat}} \tag{2.11}$$

If $\gamma = 1.4$ is assumed constant and combined with equation (2.11) and (2.10):

$$P_r = 2P_{so}\left[\frac{7P_{stat} + 4P_{so}}{7P_{stat} + P_{so}}\right] \tag{2.12}$$

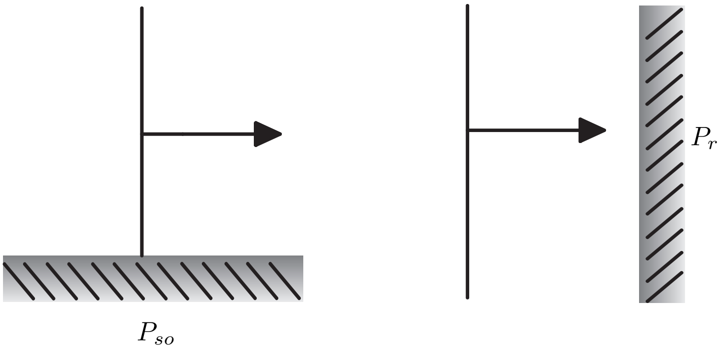

(a) Side-on pressure **(b)** Reflected pressure

Figure 2.5: Side-on and reflected pressure described [4]

At low values of P_{so}, the reflected pressure approaches the acoustic limit of twice the incident overpressure. For strong shocks, equation (2.12) would approach the upper limit of $\bar{P}_r = 8\bar{P}_{so}$ [5]. In practice γ is not constant because air ionizes and dissociates as the shock strength increases, this will lead to an even greater upper limit of equation (2.12). It is also important to note that this is for an infinitely rigid wall. As a structure subject to a blast load is deformed, the target area will be subject to deformation that in turn will alter the pressures. In reality, the reflected pressures will often be a value in between the upper and lower limits. Generally, a typical reflected shock wave will compare to a regular blast wave as illustrated in figure 2.6. Note that the positive duration typically is not altered between side-on and reflected pressures.

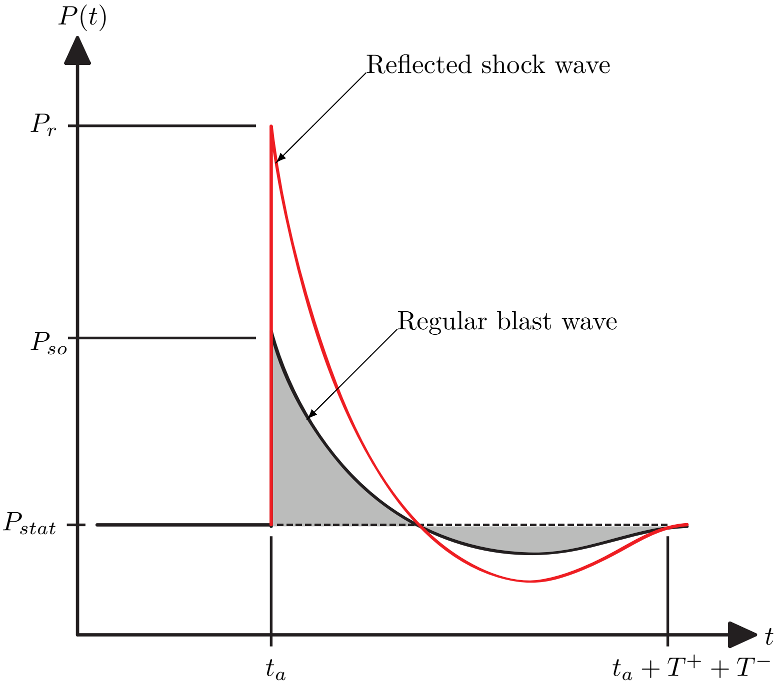

Figure 2.6: Reflected side-on pressure [23]

As explained previously, the reflected pressure on an infinitely rigid wall represent the upper limit of P_r. If the blast approaches the structure at an oblique angle, the reflected pressure will be values in between P_r and P_{so}. The oblique reflection is classified as either a regular or a mach reflection [5]. To treat the regular reflection in a design perspective, the P_r is scaled with a reflection coefficient $C_{r\alpha}$ that is a function of P_{so} and the angle of incidence α (see figure 2.7). The values for $C_{r\alpha}$ can be found in CONWEP, the UFC or other similar standards [49].

$$P_r = C_{r\alpha} P_{so} \tag{2.13}$$

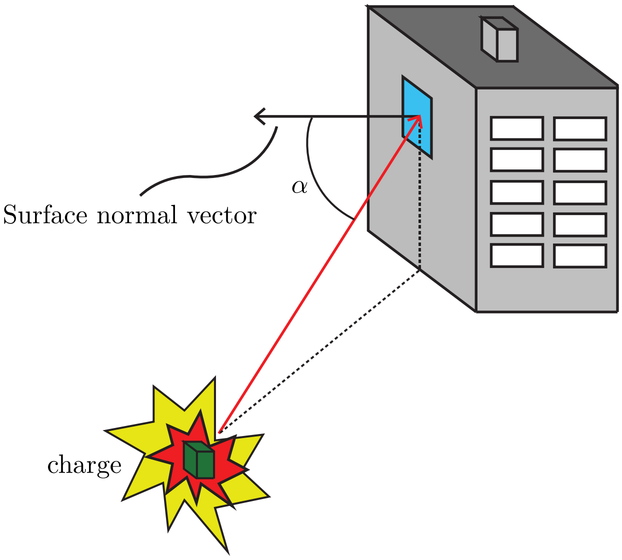

Figure 2.7: Angle of incidence

There exist some critical angle of incidence that is dependent on shock strength, below which regular reflection cannot occur [4]. When the incident is below this value, one might encounter a mach reflection. The mach reflection is treated somewhat differently because of the complex nature of the problem. When a charge detonates close to the surface, the reflected waves will bounce off the ground and fuse with the original incident wave to form a mach front. This effect is illustrated in figure 2.8 [48].

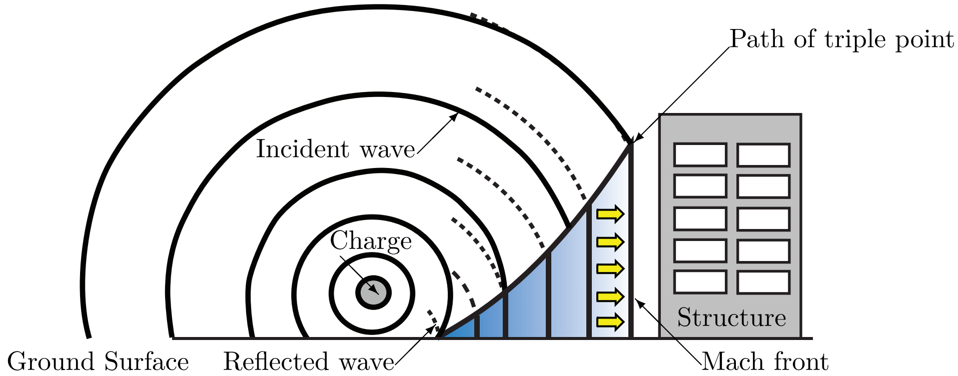

Figure 2.8: The mach reflection

The point where the incident waves and reflected waves fuse is called the triple point. A practical effect of a mach reflection is that the pressure and the positive impulse close to the triple point are considerably greater than those that would have been formed if the burst was placed on the ground itself [4].

2.1.2.5 Blast Design

For practical design purposes it exists standards such as CONWEP or the UFC that estimate the expected peak pressure, impulse and other various blast load parameters as a function of charge weight, standoff and other surrounding factors. These values are determined by a long series of empirical testing, and serve as a good tool for a simplified validation of what numbers one could expect to see in an experiment or explosive incident. A big drawback of the standards is that it is often impossible to achieve the exact same conditions as performed experiments because the explosive parameters are affected by a wide range of different circumstances, thus the values will be estimates.

To be able to compare different types of explosive incidents for blast design purposes, one usually converts the explosive mass to a TNT equivalent mass. This can be expressed as a function of the heat of detonation of the various materials as follows [23]:

$$W_{TNT} = \left(\frac{Q_{EXP}}{Q_{TNT}}\right) W_{EXP} \tag{2.14}$$

where

W_{TNT}	is the TNT equivalent weight
Q_{EXP}	is the heat of detonation of the explosive in question. (found in the UFC)
Q_{TNT}	is the heat of detonation of TNT. (found in the UFC)
W_{EXP}	is the weight of the explosive that is subject to comparison

Several problems arise when converting to TNT equivalent mass, as the scaling factor itself is a function of standoff and charge weight as shown in [31]. Note that equation (2.14) is the effective charge weight that is primarily related to the blast output parameters for unconfined detonations. The effective charge weight produced by the confinement effects of the explosion will differ.

When the TNT equivalent mass is found, the scaled distance is found by employing the following equation:

$$Z \equiv \frac{R}{W_{TNT}^{\frac{1}{3}}} \tag{2.15}$$

where

Z	is the scaled distance
R	is the standoff distance
W_{TNT}	is the explosive weight in TNT equivalents.

The scaled distance can then be compared, as a smaller scaled distance will typically lead to a higher pressure, impulse and consequently more force to the subjected surroundings.

The estimated blast load parameters can then be found from plots in the standards such as the one in figure 2.9.

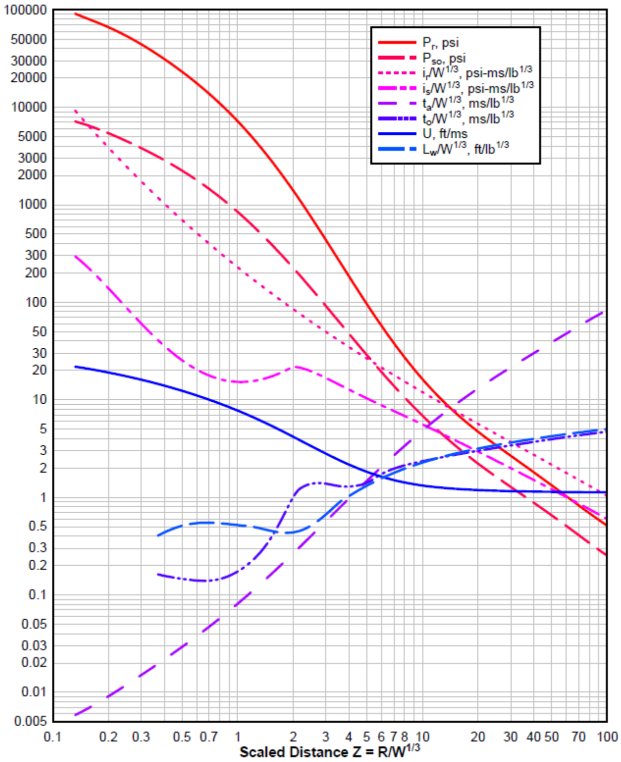

Figure 2.9: Positive phase shock wave parameters for a spherical TNT explosion in free air at sea level [23]

2.2 Constitutive Equation

In order to represent the elastic-plastic material behaviour of the steel plates, a constitutive equation needs to be established. As described in [18]; when a material yields, the loads, deformation and stresses are non-linearly related and history-dependent. Strain increments are regarded as composed of recoverable (elastic) and non-recoverable (plastic) components [18]:

$$\{d\boldsymbol{\epsilon}\} = \{d\boldsymbol{\epsilon}^e\} + \{d\boldsymbol{\epsilon}^p\} \tag{2.16}$$

where

$\{d\boldsymbol{\epsilon}\}$	total strain increment vector
$\{d\boldsymbol{\epsilon^e}\}$	elastic strain increment vector
$\{d\boldsymbol{\epsilon^p}\}$	plastic strain increment vector

Stress increments are associated with only the elastic components such that [18]:

$$\{d\boldsymbol{\sigma}\} = [\boldsymbol{E}]\,\{d\boldsymbol{\epsilon}^e\} \quad or \quad \{d\boldsymbol{\sigma}\} = [\boldsymbol{E}]\,(\{d\boldsymbol{\epsilon}\} - \{d\boldsymbol{\epsilon}^p\}) \tag{2.17}$$

where

$\{d\boldsymbol{\sigma}\}$	stress increment vector
$[\boldsymbol{E}]$	elastic material property matrix

In general, $\{d\boldsymbol{\sigma}\}$ contains increments of all six components of stress such that [18]:

$$\{d\boldsymbol{\sigma}\} = [d\boldsymbol{\sigma}_x, d\boldsymbol{\sigma}_y, d\boldsymbol{\sigma}_z, d\boldsymbol{\tau}_{xy}, d\boldsymbol{\tau}_{yz}, d\boldsymbol{\tau}_{zx}]^T \tag{2.18}$$

where

$\{d\boldsymbol{\sigma}_i\}$	stress increment in ith direction
$\{d\boldsymbol{\tau}_{ij}\}$	shear stress increment in i-j plane

Being able to describe the elastic-plastic material behaviour requires a *yield criterion*, a *flow rule* and a *hardening rule*. The yield criterion relates the state of stress to the onset of yielding. The flow rule relates the state of stress $\{\boldsymbol{\sigma}\}$, and the six increments of plastic strain $\{d\boldsymbol{\epsilon}_p\}$ when an increment of plastic flow occurs. The hardening rule modifies the yield criterion for straining beyond the initial yield. Yielding is defined by $F = 0$, where F is defined as the yield function [18].

$$F = F\left(\{\boldsymbol{\sigma}\}, \{\boldsymbol{\alpha}\}, W_p\right) \tag{2.19}$$

where

$\{\boldsymbol{\sigma}\}$	total stress vector
$\{\boldsymbol{\alpha}\}$	vector describing kinematic hardening
W_p	scalar describing the isotropic hardening

$\{\boldsymbol{\alpha}\}$ and W_p describes how the yield surface is altered in multi-dimensional stress space in response to plastic strain increments. As mentioned in [44] three factors are important regarding material behaviour subjected to blast and penetration problems.

- strain
- strain-rate
- temperature

Increased strain-rate normally increases the strength and an increased temperature decreases the strength. A commonly used material model which accommodates the aforementioned factors is the Johnson-Cook material (JC) model [12]:

$$\sigma_{eq} = \left(A + B\epsilon_{eq}^n\right)\left(1 + C\ln\frac{\dot{\epsilon}}{\dot{\epsilon_0}}\right)\left(1 - \left(\frac{T - T_r}{T_m - T_r}\right)^m\right) \tag{2.20}$$

where

A, B, C, n, m	material constants
ϵ_{eq}	equivalent plastic strain
$\dot{\epsilon}$	strain-rate
$\dot{\epsilon}_0$	reference strain-rate
T	temperature
T_r	reference temperature
T_m	melting temperature

The strain-rate sensitivity term $\left(1 + C\ln\frac{\dot{\epsilon}}{\dot{\epsilon_0}}\right)$ was modified in [15] to be able to represent small strain-rate effects. A modified version of JC can be written as [12]:

$$\sigma_{eq} = \left(A + B\epsilon_{eq}^{n}\right)\left(1 + \frac{\dot{\epsilon}}{\dot{\epsilon_0}}\right)^{C}\left(1 - \left(\frac{T - T_r}{T_m - T_r}\right)^{m}\right) \tag{2.21}$$

The non-linear isotropic strain hardening Voce law is used to represent strain hardening:

$$\sigma_{eq} = \sigma_0 + \sum_{i=1}^{n} Q_i \left(1 - \exp\left(-C_i \epsilon_{eq}\right)\right) \tag{2.22}$$

where

σ_0	initial yield stress
Q_1, C_1	primary hardening
Q_2, C_2	secondary hardening

The final constitutive relation using modified JC with Voce hardening results in the following equation:

$$\sigma_{eq} = \left(\sigma_0 + \sum_{i=1}^{n} Q_i \left[1 - \exp\left(-C_i \epsilon_{eq}\right)\right]\right)\left(1 + \frac{\dot{\epsilon}}{\dot{\epsilon_0}}\right)^{C}\left(1 - \left(\frac{T - T_r}{T_m - T_r}\right)^{m}\right) \tag{2.23}$$

In the event of fracture, a *fracture criterion* needs to be set. As mentioned in [44], a ductile fracture is highly dependent on the stress triaxiality. A simple fracture criteria which includes stress triaxiality and is widely used is the Cockcroft-Latham (CL) fracture criterion [30]:

$$W = \int_0^{\epsilon_f} \langle \sigma_1 \rangle d\epsilon_{eq} \leq W_{cr} \tag{2.24}$$

and

$$\langle \sigma_1 \rangle = \begin{cases} \sigma_1 & \sigma_1 \geq 0 \\ 0 & \sigma_1 < 0 \end{cases} \tag{2.25}$$

where

σ_1	major principle stress
W_{cr}	the critical value of the plastic work per unit volume until fracture
W	the plastic strain energy density
ϵ_f	the strain at fracture

The concept is that damage accumulates until $W = W_{cr}$ is reached at $\epsilon_{eq} = \epsilon_f$.

2.3 Failure Modes

In the event of failure in the plates subject to blast loading, a system of classifying different failure modes is described in [54]. Note that the study in [54] was based on the failure of circularly shaped plates. However, it is assumed that this can be translated in to similar expected behaviour for quadratically shaped plates. Failure of plates subject to impulsive velocities are classified in to three distinct failure modes [54]:

- Mode I: Large ductile deformation (figure 2.10a)
- Mode II: Tensile-tearing and deformation (figure 2.10b)
- Mode III: Transverse shear (figure 2.10c)

Mode II can be further divided into three levels of tensile tearing [39];

- II* Partial tensile tearing
- IIa Complete tensile tearing with increasing deformation
- IIb Complete tensile tearing with decreasing deformation

The main failure modes are depicted in figure 2.10

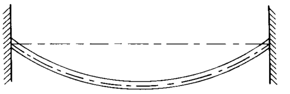

(a) Mode I

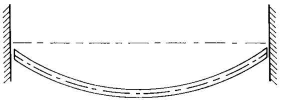

(b) Mode II

(c) Mode III

Figure 2.10: Failure modes [54]

Mode II* is the borderline case between Mode I and Mode IIa. Mode IIb is the borderline case between Mode IIa and Mode III [44].

2.4 Numerical Methods

2.4.1 Time Integration

Initially the analyst has the choice between an implicit and an explicit time integration scheme to a numerical simulation. Explicit time integration proves the best suited for high speed blast simulations. Explicit methods have major advantages when it comes to solving contact problems and wave propagation problems created by a blast or impact loading because no equilibrium iterations are necessary [35]. The explicit scheme have a low cost per time step, but since the method is conditionally stable, a very small time step is required.

Perform a first order Taylor-series expansion of the displacement d_{n+1} and d_{n-1} about time t_n and combine the resulting equations:

$$\dot{d}_n = \frac{d_{n+1} - d_{n-1}}{2\Delta t} \quad \text{or} \quad \ddot{d}_n = \frac{d_{n+1} - 2d_n + d_{n-1}}{\Delta t^2} \tag{2.26}$$

These two equations are often referred to as the conventional central difference equations [35]. Since we employed a first order Taylor series expansion, the primary error term in these equations are proportional to Δt^2 which implies that the displacement d has second order accuracy.

Substitute the central difference approximations for velocity and acceleration in to the equilibrium equation for a non-linear MDOF system

$$[\boldsymbol{M}]\left\{\ddot{\boldsymbol{D}}\right\} + [\boldsymbol{C}]\left\{\dot{\boldsymbol{D}}\right\} + \left\{\boldsymbol{R}^{int}\right\} = \left\{\boldsymbol{R}^{ext}\right\} \tag{2.27}$$

To obtain [35].

$$\{\boldsymbol{D}\}_{n+1} = \left[\boldsymbol{K}^{eff}\right]^{-1}\left\{\boldsymbol{R}^{eff}\right\}_n \tag{2.28}$$

where

$$\left[\boldsymbol{K}^{eff}\right] = \frac{1}{\Delta t^2}[\boldsymbol{M}] + \frac{1}{2\Delta t}[\boldsymbol{C}] \tag{2.29}$$

$$
\begin{aligned}
\left\{\boldsymbol{R}^{eff}\right\}_n = \left\{\boldsymbol{R}^{ext}\right\}_n - \left\{\boldsymbol{R}^{int}\right\} + \frac{2}{\Delta t^2}\left[\boldsymbol{M}\right]\left\{\boldsymbol{D}\right\}_n \\
- \left(\frac{1}{\Delta t^2}\left[\boldsymbol{M}\right] - \frac{1}{2\Delta t}\left[\boldsymbol{C}\right]\right)\left\{\boldsymbol{D}\right\}_{n-1}
\end{aligned} \tag{2.30}
$$

If lumped mass matrices combined with mass proportional damping is employed, displacements $\{\boldsymbol{D}\}_{n+1}$ may be computed very efficiently. However since the mass proportional Rayleigh damping damps lower modes mainly, the dynamic response will contain high frequency numerical noise [35]. It may be desirable to include a stiffness-proportional damping in order to damp high frequency numerical noise. The solution of an equation system is then required since the effective stiffness $\left[\boldsymbol{K}^{eff}\right]$ becomes non-diagonal, thus the computational cost per time step is greatly increased. However, it may be shown that if the equilibrium equations are established with velocity lagging by half a time step, the problem with increased computational cost may be traversed [35].

2.4.1.1 Time Integration in LS-DYNA

The classic half-step central difference method is the integration scheme implemented in LS-DYNA [32]. Establish the equation of motion with the velocity term lagging half a time step behind:

$$
\left[\boldsymbol{M}\right]\left\{\ddot{\boldsymbol{D}}\right\}_n + \left[\boldsymbol{C}\right]\left\{\dot{\boldsymbol{D}}\right\}_{n-\frac{1}{2}} + \left\{\boldsymbol{R}^{int}\right\}_n = \left\{\boldsymbol{R}^{ext}\right\} \tag{2.31}
$$

By employing

$$
\left\{\dot{\boldsymbol{D}}\right\}_{n-\frac{1}{2}} = \frac{1}{\Delta t}\left(\{\boldsymbol{D}\}_n - \{\boldsymbol{D}\}_{n-1}\right) \tag{2.32}
$$

and

$$
\left\{\dot{\boldsymbol{D}}\right\}_{n+\frac{1}{2}} = \frac{1}{\Delta t}\left(\{\boldsymbol{D}\}_{n+1} - \{\boldsymbol{D}\}_{n}\right) \tag{2.33}
$$

To obtain

$$
\begin{aligned}
\left\{\ddot{\boldsymbol{D}}\right\}_n &= \frac{1}{\Delta t}\left(\left\{\dot{\boldsymbol{D}}\right\}_{n+\frac{1}{2}} - \left\{\dot{\boldsymbol{D}}\right\}_{n-\frac{1}{2}}\right) \\
&= \frac{\{\boldsymbol{D}\}_{n+1} - 2\{\boldsymbol{D}\}_n + \{D\}_{n-1}}{\Delta t^2}
\end{aligned} \tag{2.34}
$$

By substituting these equations in to the equation of motion and approximating the damping term by:

$$\frac{1}{2\Delta t}\left[\boldsymbol{C}\right]\left(\left\{\boldsymbol{D}\right\}_{n-1}-\left\{\boldsymbol{D}\right\}_{n+1}\right)\approx\frac{1}{\Delta t}\left[\boldsymbol{C}\right]\left(\left\{\boldsymbol{D}\right\}_{n-1}-\left\{\boldsymbol{D}\right\}_{n}\right) \tag{2.35}$$

The preferred form of the central difference method is obtained [35]:

$$\left\{\boldsymbol{D}\right\}_{n+1}=\Delta t^{2}\left[\boldsymbol{M}\right]^{-1}\left\{\boldsymbol{R}^{eff}\right\}_{n} \tag{2.36}$$

Where

$$\begin{aligned}\left\{\boldsymbol{R}^{eff}\right\}_{n}=\left\{\boldsymbol{R}^{ext}\right\}_{n}-\left\{\boldsymbol{R}^{int}\right\}+\frac{1}{\Delta t^{2}}\left[\boldsymbol{M}\right]\left(2\left\{\boldsymbol{D}\right\}_{n}+\left\{\boldsymbol{D}\right\}_{n-1}\right)\\-\frac{1}{\Delta t}\left[\boldsymbol{C}\right]\left(\left\{\boldsymbol{D}\right\}_{n}-\left\{\boldsymbol{D}\right\}_{n-1}\right)\end{aligned} \tag{2.37}$$

The preferred form of the central difference method can only guarantee first-order accuracy, but for small damping values and small time steps it has almost the same accuracy as the classical central difference method [35]. In order for initial calculations to be performed, a need exists to employ a backward finite difference approximations [35] which yields:

$$\left\{\ddot{\boldsymbol{D}}\right\}_{0}=\frac{2}{\Delta t}\left(\left\{\dot{\boldsymbol{D}}\right\}_{0}-\left\{\dot{\boldsymbol{D}}\right\}_{-\frac{1}{2}}\right) \tag{2.38}$$

leads to

$$\left\{\dot{\boldsymbol{D}}\right\}_{-\frac{1}{2}}=\left\{\boldsymbol{D}\right\}_{0}-\frac{\Delta t}{2}\left\{\ddot{\boldsymbol{D}}\right\}_{0} \tag{2.39}$$

By approximating $\left\{\dot{\boldsymbol{D}}\right\}_{-\frac{1}{2}}$ with a central difference [1]:

$$\left\{\dot{\boldsymbol{D}}\right\}_{-\frac{1}{2}}=\frac{1}{\Delta t}\left(\left\{\boldsymbol{D}\right\}_{0}-\left\{\boldsymbol{D}\right\}_{-1}\right) \tag{2.40}$$

To arrive at an expression for $\left\{\boldsymbol{D}\right\}_{-1}$ [18]:

$$\left\{\boldsymbol{D}\right\}_{-1}=\left\{\boldsymbol{D}\right\}_{0}-\left\{\dot{\boldsymbol{D}}\right\}_{0}\Delta t+\frac{\Delta t^{2}}{2}\left\{\ddot{\boldsymbol{D}}\right\}_{0} \tag{2.41}$$

where the value of $\left\{\ddot{\boldsymbol{D}}\right\}_{0}$ can be found from the equilibrium equation of motion.

The time integration loop implemented in LS-DYNA is illustrated in figure 2.11 [32].

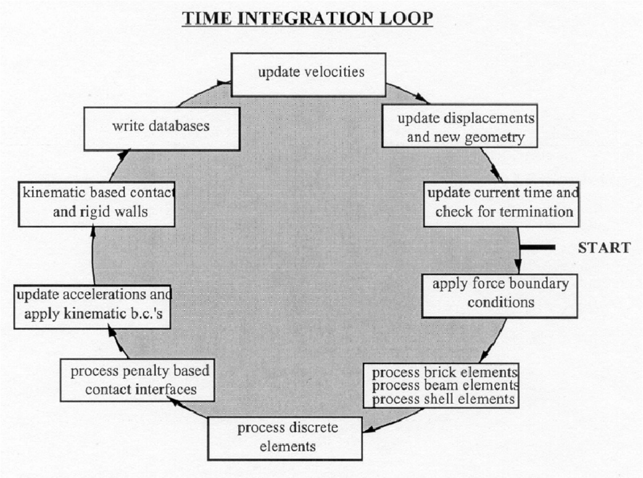

Figure 2.11: Time integration loop in LS-DYNA [32]

2.4.1.2 Stability of the Explicit Time Integration

One big drawback of the explicit analysis is the conditional stability of the explicit analysis. The solution is bounded only when the time increment Δt is less than the stable time increment Δt_{cr}. It can be shown that the stability limit can be defined in terms of the eigen-frequency (ω_j) and the fraction of critical damping (ξ_j) of eigen-mode ϕ_j [36]:

$$\Delta t_{cr} \leq \min\left[\frac{2}{\omega_j}\left(\sqrt{1-\xi_j^2}-\xi_j\right)\right] \tag{2.42}$$

Since for all practical problems, damping is likely to be small for all modes, thus for an undamped material, the upper bound for the critical time step becomes:

$$\Delta t_{cr} \leq \frac{2}{\omega_{\max}} \tag{2.43}$$

The physical interpretation is that Δt must be small enough so that information does not propagate more than the distance between adjacent nodes during a single time-step. The stable time increment can then be expressed in terms of the dilatational wave speed c_d, and the characteristic length L^e of the smallest element in the FE model [36].

$$\Delta t_{cr} = \frac{L^e}{c_d} \tag{2.44}$$

where

L^e	Characteristic length of the smallest element
C_d	Dilatational wave speed in the material

2.4.2 Finite Element Formulations

In this section, an introduction to the Lagrangian, Eulerian and the Arbitrary Lagrangian Eulerian finite element formulations will be given. The different finite element formulations arise from the same set of fundamental conservation laws. These equations must always be satisfied by a physical system [7]. The four conservation laws relevant for thermomechanical systems are.

- Conservation of mass
- Conservation of linear momentum
- Conservation of energy
- Conservation of angular momentum

The conservation laws are usually expressed as partial differential equations (PDE). These equations are derived by forcing the conservation laws on to a domain of a body that in turn leads to an integral relation [7].

For each of the element formulations, the conservation equations will be represented, also how the different kinematic relations differ from one another. The kinematic relations together with most of the theory in this section is taken from [7] if not stated otherwise.

2.4.2.1 Preliminary Kinematics

A body in the initial state at time t=0 is referred to as being in the reference configuration Ω_0. The significance of the reference configuration lies in the fact that motion is defined with respect to this configuration. The boundary of the respective configurations are referred to as Γ_0 and Γ.

The motion or deformation of a body is described by a function $\boldsymbol{\phi}(\boldsymbol{X}, t)$ with material coordinates $\boldsymbol{X}$ and time t as independent variables [7]. This function gives the spatial positions of the material points as a function of time through:

$$\boldsymbol{x} = \boldsymbol{\phi}(\boldsymbol{X}, t) \tag{2.45}$$

This relation is also called a map between the reference and current configuration. The displacement of a material point denoted $\boldsymbol{u}$ is the difference between its current position and its original position:

$$\boldsymbol{u}(\boldsymbol{X}, t) = \boldsymbol{\phi}(\boldsymbol{X}, t) - \boldsymbol{X} \tag{2.46}$$

An illustration of the kinematic relations can be seen in figure 2.12

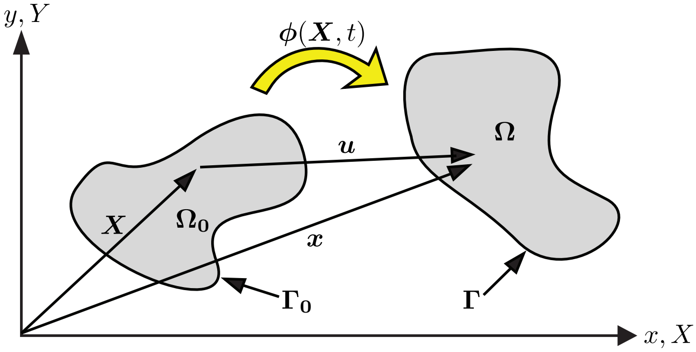

Figure 2.12: Kinematic relations

The velocity is the rate of change of the position vector for a material point:

$$\boldsymbol{v}(\boldsymbol{X}, t) = \frac{\partial \boldsymbol{\phi}(\boldsymbol{X}, t)}{\partial t} = \frac{\partial \boldsymbol{u}(\boldsymbol{X}, t)}{\partial t} \equiv \dot{\boldsymbol{u}} \tag{2.47}$$

The acceleration is the rate of change of velocity of a material point:

$$\boldsymbol{a}(\boldsymbol{X}, t) = \frac{\partial \boldsymbol{v}(\boldsymbol{X}, t)}{\partial t} = \frac{\partial^2 \boldsymbol{u}(\boldsymbol{X}, t)}{\partial t^2} \equiv \dot{\boldsymbol{v}} \tag{2.48}$$

To describe the deformation and the measure of strain is an important part of non-linear continuum mechanics. An important variable in this matter is the deformation gradient:

$$F_{ij} = \frac{\partial \phi_i}{\partial X_j} \equiv \frac{\partial x_i}{\partial X_j} \quad \text{or} \quad \boldsymbol{F} = \frac{\partial \boldsymbol{\phi}}{\partial \boldsymbol{X}} \equiv \frac{\partial \boldsymbol{x}}{\partial \boldsymbol{X}} \equiv (\nabla_0 \boldsymbol{\phi})^T \tag{2.49}$$

The deformation gradient $\boldsymbol{F}$ is often also referred to as the Jacobian matrix of the motion $\boldsymbol{\phi}(\boldsymbol{X}, t)$.

Two different approaches are used to describe the deformation of a body in a continuum. In the Lagrangian description the independent variables are the material coordinates $\boldsymbol{X}$ and the pseudo-time t. This description is therefore often referred to as a material description. In the other approach the independent variables are the spatial coordinates $\boldsymbol{x}$ and the pseudo-time t. This is called a spatial or Eulerian description. Note that so far the kinematic relations are only for material points, as they do not differ for the two formulations.

2.4.3 Lagrangian FEA

In classical solid mechanics, the Lagrangian formulation is the most widely used. The attractiveness roots in how the formulation handles complicated boundary conditions and the ability to follow specific material points. There exist different varieties of the Lagrangian formulation, namely the Updated Lagrangian Formulation and the Corotational Lagrangian Formulation among others. In this study however, we will focus on the Total Lagrangian Formulation in which integrals and derivatives are taken with respect to the material coordinates $\boldsymbol{X}$.

In a Lagrangian mesh, the nodes are coincident with the material points as illustrated in figure 2.13, so in short the nodes $\boldsymbol{X}_I$ = constant in time. This leads to the fact that the mesh cannot deform without the material deforming and vice versa. This suits the applicability of solid mechanics greatly since most non-linear materials are history dependent, and they are easily traceable if referred to the initial undeformed configuration. The fact that the mesh deforms with the body allows the analyst employ the use of history dependent materials with finite (small) deformations. Another advantage of the Lagrangian formulation is that is an easy task to track material boundaries because they coincide with element edges. The tracking of element quadrature points are also simple because the mesh is coinciding with material points.

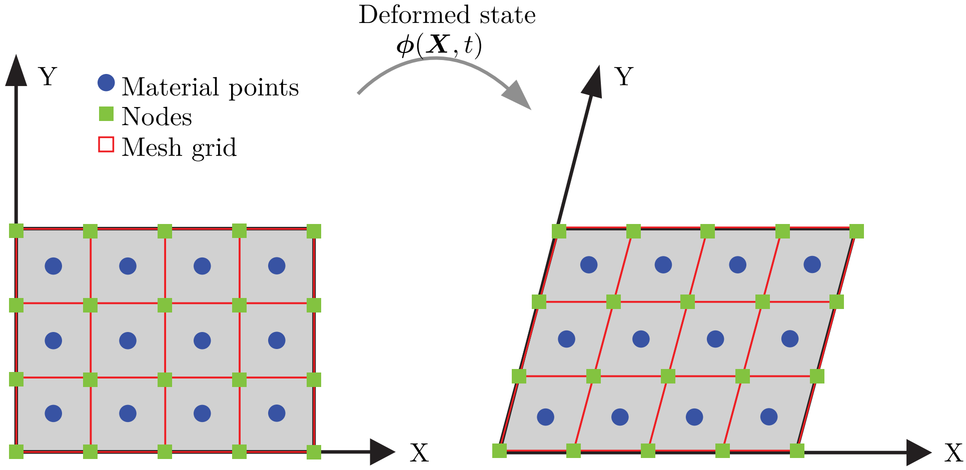

Figure 2.13: The Lagrangian FE formulation

As stated in section 2.4.2 the conservation laws have to be satisfied for a physical body. For the Lagrangian formulation the conservation gives rise to the following equations [7]:

Conservation of mass

$$\rho\left(\boldsymbol{X},t\right)J\left(\boldsymbol{X},t\right)=\rho_0\left(\boldsymbol{X}\right)\quad\text{or}\quad\rho J=\rho_0 \tag{2.50}$$

Conservation of linear momentum

$$\rho_0\frac{\partial\boldsymbol{v}(\boldsymbol{X},t)}{\partial t}=\nabla_0\cdot\boldsymbol{P}+\rho_0\boldsymbol{b}\quad\text{or}\quad\rho_0\frac{\partial v_i(\boldsymbol{X},t)}{\partial t}=\frac{\partial P_{ji}}{\partial X_j}+\rho_0 b_i \tag{2.51}$$

Conservation of angular momentum

$$\boldsymbol{F}\cdot\boldsymbol{F}=\boldsymbol{P}^T\cdot\boldsymbol{F}^T\quad\text{or}\quad F_{ik}P_{kj}=P^T_{ik}F^T_{kj}=F_{jk}P_{ki},\quad\boldsymbol{S}=\boldsymbol{S}^T \tag{2.52}$$

Conservation of energy

$$\left.\begin{array}{c}\rho_0\dot{w}^{int}=\rho_0\frac{\partial w^{int}(\boldsymbol{X},t)}{\partial t}=\dot{\boldsymbol{F}}^T:\boldsymbol{P}-\nabla_0\cdot\tilde{\boldsymbol{q}}+\rho_0 s\\ \text{or}\\ \rho_0\dot{w}^{int}=\dot{F}_{ji}P_{ij}-\frac{\partial\tilde{q}_i}{\partial X_i}+\rho_0 s\end{array}\right\} \tag{2.53}$$

where

ρ_0	is the original density
ρ	is the current density
w	is the hyperelastic potential on the reference configuration
$\boldsymbol{b}$	is the body force vector
J	is the determinant of the Jacobian between spatial and material coordinates $J = \det\left[\partial x_i / \partial X_j\right]$.
$\boldsymbol{F}$	is the deformation gradient $F_{ij} = \partial x_i / \partial X_j$
$\boldsymbol{S}$	is the Second Piola-Kirchhoff (PK2) stress.
$\boldsymbol{P}$	is the nominal stress (the transpose of the first Piola-Kirchoff stress).
$\boldsymbol{q}$	is the collection of internal variables in the constitutive model
s	is the specific heat source term

One big drawback of the Lagrangian element formulation is that it has difficulties with treating severe deformed bodies. Because the mesh is fixed at specific material point, extensive deformation may cause markedly distorted elements. The severly distorted elements will contribute to a degraded accuracy and a negative Jacobian determinant might be obtained that can worsen the numerical errors greatly [7]. Therefore, for applications where we expect very large deformations, an Eulerian FEA might be more applicable.

2.4.4 Eulerian FEA

Eulerian FEA is most suited for problems with very large deformations. As opposed to the Lagrangian formulation where the mesh is fixed on specific material points, the Eulerian mesh is fixed in space, and the material can deform independently of the mesh. The dependent variables are functions of the Eulerian spatial coordinate $\boldsymbol{x}$ and the time t. In short it is often said that the Eulerian nodes $\boldsymbol{x}_I$ = constant in time. This serves to be ideal for problems where the material is not history dependent and very large deformations of the body are present. In fluid mechanics, it is very hard and often impossible to describe the motion of the fluid with respect to a reference configuration. However it is not needed since the state of a newtonian fluid is independent of its history.

An illustration of the Eulerian FEA can be seen in figure 2.14 for the shearing of a rectangular plate in two dimensions. As we can see, the material points deform independently from the mesh.

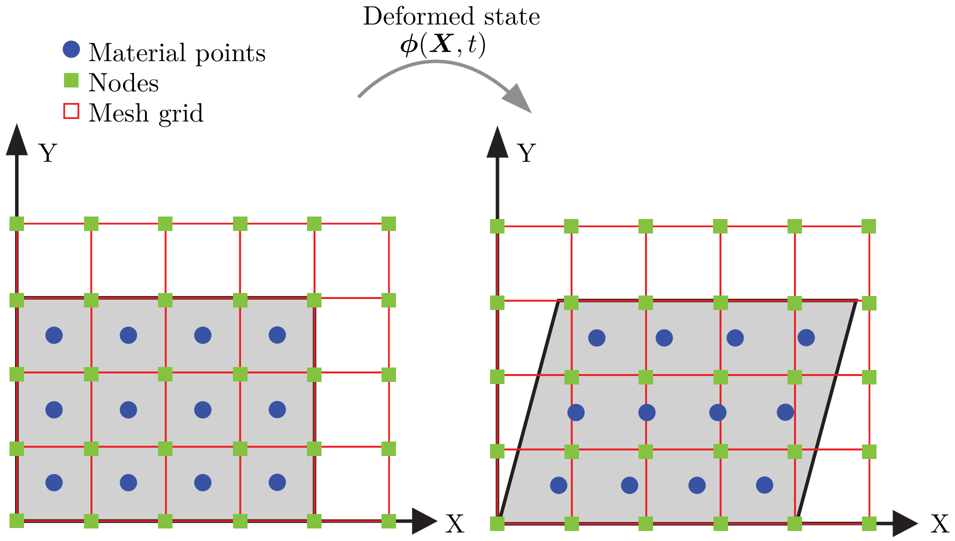

Figure 2.14: The Eulerian FE formulation

The conservation equations that must hold in the Eulerian element formulation are as follows:

Conservation of mass:

$$\frac{D\rho}{Dt} + \rho \mathrm{div}(\boldsymbol{v}) = 0 \quad \text{or} \quad \frac{D\rho}{Dt} + \rho v_{i,i} = 0 \quad \text{or} \quad \dot{\rho} + \rho v_{i,i} = 0 \tag{2.54}$$

Conservation of linear momentum:

$$\rho \frac{D\boldsymbol{v}}{Dt} = \nabla \cdot \boldsymbol{\sigma} + \rho \boldsymbol{b} \equiv \mathrm{div}\,(\boldsymbol{\sigma}) + \rho \boldsymbol{b} \quad \text{or} \quad \rho \frac{Dv_i}{Dt} = \frac{\partial \sigma_{ji}}{\partial x_j} + \rho b_i \tag{2.55}$$

Conservation of angular momentum:

$$\boldsymbol{\sigma} = \boldsymbol{\sigma}^T \quad \text{or} \quad \sigma_{ij} = \sigma_{ji} \tag{2.56}$$

Conservation of energy:

$$\rho\frac{Dw^{int}}{Dt} = \boldsymbol{D} : \boldsymbol{\sigma} - \nabla\cdot\boldsymbol{q} + \rho s \quad \text{or} \quad \rho\dot{w}^{int} = D_{ij}\sigma_{ij} - \frac{\partial q_i}{\partial x_i} + \rho s \tag{2.57}$$

where

$\boldsymbol{v}$	is the velocity field
$\boldsymbol{D}$	is the rate of deformation, the velocity strain $\boldsymbol{D} = \text{sym}(\nabla\boldsymbol{v})$
$\boldsymbol{\sigma}$	is the Cauchy stress tensor

In contrast to the Lagrangian description, it is not easy to track material interfaces because they do not coincide with element edges. Tracking methods or approximate methods such as volume or fluid approaches need to be employed for moving boundaries. In addition to this, the Eulerian mesh must be large enough to enclose the material in its deformed state, or instabilities may occur.

2.4.5 Arbitrary Lagrangian Eulerian FEA.

The two aforementioned formulations have their obvious strengths and weaknesses. To capitalize on the strengths of both methods the Arbitrary Lagrangian Eulerian (ALE) finite element formulations have been developed. The goal of the ALE formulation is to capture the advantages of both the Lagrange and Eulerian formulations while marginalizing the disadvantages associated with each method. The result is a formulation where the mesh is adopting to the material deformation to reduce the numerical errors associated with large elements in the Eulerian formulation and to prevent ill-shaped elements in the Lagrangian formulation. The ALE formulation also treats the problem of describing complicated boundaries in the Eulerian formulation. The problems associated with the Lagrangian and Eulerian formulations are illustrated in figure 2.15.

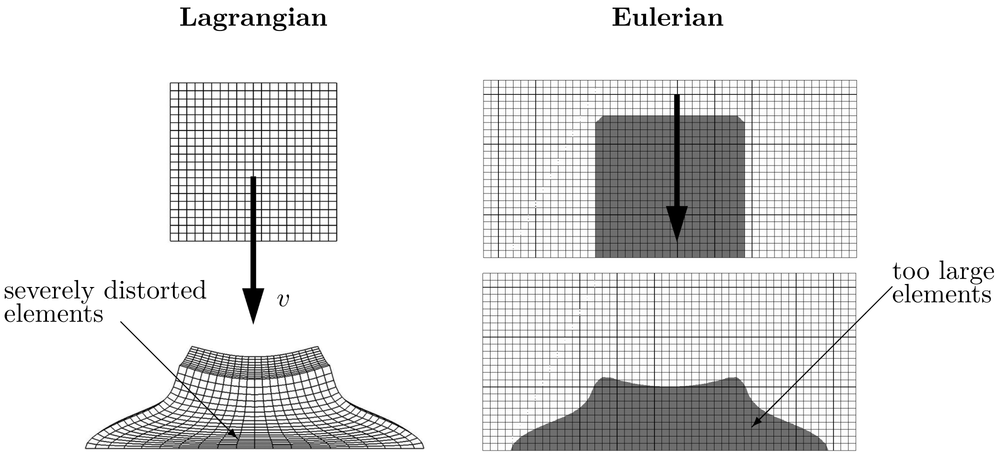

Figure 2.15: Lagrangian and Eulerian associated problems [40]

In an ALE formulation, the mesh will adapt in order to better represent the large deformations. This effect is illustrated in figure 2.16.

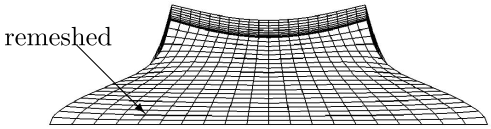

(a) Lagrangian

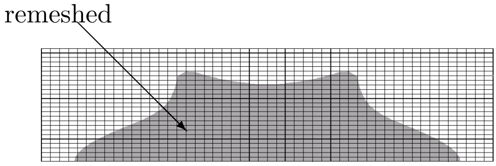

(b) Eulerian

Figure 2.16: Adaptation of the ALE-mesh [40]

When both element formulations are implemented in the same code, it allows for materials with very stiff subdomains to be represented accurately by a Lagrangian formulation, modelled together with fluids deforming comprehensibly in an Eulerian mesh. It is quite often suitable to treat parts of a model as a Lagrangian structure and other parts as Eulerian, This is called a Fluid Structure Interaction (FSI) formulation. A FSI coupling algorithm is needed for the communication between the different parts [40].

In section 2.4.2.1 it was stated that the displacement, velocity and acceleration of the material was independent of the chosen element formulation. This also holds for the ALE formulation. However, the displacement, velocity and acceleration of the mesh are different in the three element formulations. To properly describe kinematics in the ALE formulation, the ALE referential domain $\hat{\Omega}$ is introduced together with the ALE coordinates $\boldsymbol{\chi}$. The ALE domain $\hat{\Omega}$ is used to describe the motion of the mesh independently of the material.

The motion of the mesh is described by:

$$\boldsymbol{x} = \hat{\boldsymbol{\phi}}(\boldsymbol{\chi}, t) \tag{2.58}$$

The $\hat{\boldsymbol{\phi}}$ function is crucial. By employing this function the points in the ALE domain is mapped on to $\boldsymbol{x}$ in the spatial domain. By combining equation (2.45) and (2.46) with equation (2.58) we relate the material coordinates to the ALE coordinates:

$$\boldsymbol{\chi} = \hat{\boldsymbol{\phi}}^{-1}(\boldsymbol{x}, t) = \hat{\boldsymbol{\phi}}^{-1}(\boldsymbol{\phi}(\boldsymbol{X}, t), t) = \boldsymbol{\Psi}(\boldsymbol{X}, t) \tag{2.59}$$

or

$$\boldsymbol{\Psi} = \hat{\boldsymbol{\phi}}^{-1} \circ \boldsymbol{\phi} \tag{2.60}$$

Then the material motion can be expressed as a composition of the mesh motion and the $\boldsymbol{\Psi}$ map:

$$\boldsymbol{x} = \boldsymbol{\phi}(\boldsymbol{X}, t) = \hat{\boldsymbol{\phi}}(\boldsymbol{\Psi}(\boldsymbol{X}, t), t) \tag{2.61}$$

or

$$\boldsymbol{\phi} = \hat{\boldsymbol{\phi}} \circ \boldsymbol{\Psi} \tag{2.62}$$

The compatibility of the different domains is illustrated in figure 2.17.

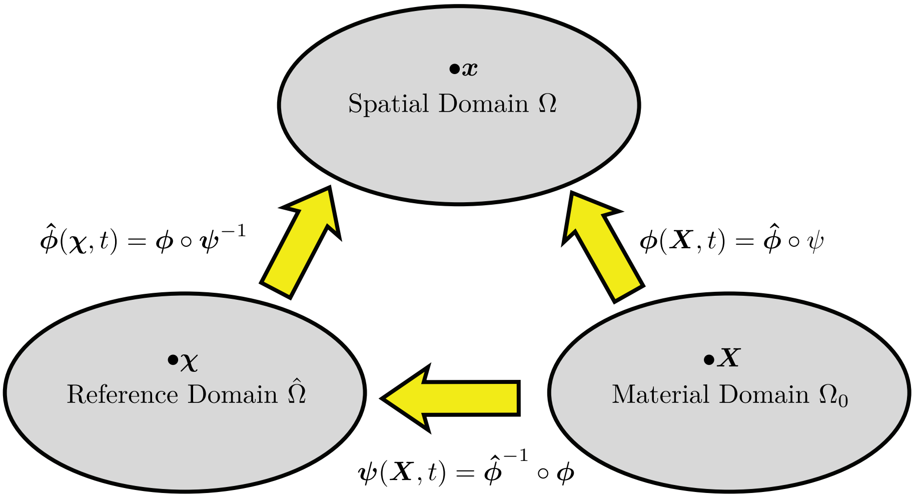

Figure 2.17: Compatibility of different domains

While the mesh kinematics was easy to obtain for the Lagrangian and Eulerian formulations, it becomes a bit more cumbersome with the ALE formulation. Mesh displacement is obtained by:

$$\hat{\boldsymbol{u}}(\boldsymbol{\chi},t)=\boldsymbol{x}-\boldsymbol{\chi}=\hat{\boldsymbol{\phi}}(\boldsymbol{\chi},t)-\boldsymbol{\chi} \tag{2.63}$$

Mesh velocity is defined analogously to the material velocity

$$\hat{\boldsymbol{v}}(\boldsymbol{\chi},t)=\frac{\partial\hat{\boldsymbol{\phi}}(\boldsymbol{\chi},t)}{\partial t}\equiv\hat{\boldsymbol{\phi}}_{,t[\boldsymbol{\chi}]} \tag{2.64}$$

Mesh acceleration follows:

$$\hat{\boldsymbol{a}}(\boldsymbol{\chi},t)=\frac{\partial\hat{\boldsymbol{v}}(\boldsymbol{\chi},t)}{\partial t}=\frac{\partial^2\hat{\boldsymbol{u}}(\boldsymbol{\chi},t)}{\partial t^2}=\hat{\boldsymbol{u}}_{,tt[\boldsymbol{\chi}]} \tag{2.65}$$

For convenience the kinematics for material and mesh motion with respect to all three formulations are given in table 2.2.

Table 2.2: Kinematics for material and mesh motion for all three formulations [7]

Description		General ALE	Lagrangian	Eulerian
Motion	Material	$\boldsymbol{x} = \boldsymbol{\phi}(\boldsymbol{X}, t)$	$\boldsymbol{x} = \boldsymbol{\phi}(\boldsymbol{X}, t)$	$\boldsymbol{x} = \boldsymbol{\phi}(\boldsymbol{X}, t)$
	Mesh	$\boldsymbol{x} = \hat{\boldsymbol{\phi}}(\boldsymbol{\chi}, t)$	$\boldsymbol{x} = \boldsymbol{\phi}(\boldsymbol{X}, t)$ $(\boldsymbol{\chi} = \boldsymbol{X},\ \hat{\boldsymbol{\phi}} = \boldsymbol{\phi})$	$\boldsymbol{x} = \boldsymbol{I}(\boldsymbol{x})$ $(\boldsymbol{\chi} = \boldsymbol{x}\ ,\ \hat{\boldsymbol{\phi}} = \boldsymbol{I})$
Displacement	Material	$\boldsymbol{u} = \boldsymbol{x} - \boldsymbol{X}$	$\boldsymbol{u} = \boldsymbol{x} - \boldsymbol{X}$	$\boldsymbol{u} = \boldsymbol{x} - \boldsymbol{X}$
	Mesh	$\hat{\boldsymbol{u}} = \boldsymbol{x} - \boldsymbol{\chi}$	$\hat{\boldsymbol{u}} = \boldsymbol{x} - \boldsymbol{X} = \boldsymbol{u}$	$\hat{\boldsymbol{u}} = \boldsymbol{x} - \boldsymbol{X} = \boldsymbol{0}$
Velocity	Material	$\boldsymbol{v} = \boldsymbol{u}_{,t[\boldsymbol{X}]}$	$\boldsymbol{v} = \boldsymbol{u}_{,t[\boldsymbol{X}]}$	$\boldsymbol{v} = \boldsymbol{u}_{,t[\boldsymbol{X}]}$
	Mesh	$\hat{\boldsymbol{v}} = \hat{\boldsymbol{u}}_{,t[\boldsymbol{X}]}$	$\hat{\boldsymbol{v}} = \hat{\boldsymbol{u}}_{,t[\boldsymbol{X}]} = \boldsymbol{v}$	$\hat{\boldsymbol{v}} = \hat{\boldsymbol{u}}_{,t[\boldsymbol{X}]} = \boldsymbol{0}$
Acceleration	Material	$\boldsymbol{a} = \boldsymbol{v}_{,t[\boldsymbol{X}]}$	$\boldsymbol{a} = \boldsymbol{v}_{,t[\boldsymbol{X}]}$	$\boldsymbol{a} = \boldsymbol{v}_{,t[\boldsymbol{X}]}$
	Mesh	$\hat{\boldsymbol{a}} = \hat{\boldsymbol{v}}_{,t[\boldsymbol{X}]}$	$\hat{\boldsymbol{a}} = \hat{\boldsymbol{v}}_{,t[\boldsymbol{X}]} = \boldsymbol{a}$	$\hat{\boldsymbol{a}} = \hat{\boldsymbol{v}}_{,t[\boldsymbol{X}]} = \boldsymbol{0}$

Prior to expressing the governing equations for the ALE formulations, two definitions must be stated. The convective velocity c_i is defined as the difference between the material and mesh velocity

$$c_i = v_i - \hat{v}_i \tag{2.66}$$

The material time derivative which is embedded in the ALE formulation is defined as follows:

$$\frac{Df}{Dt} = f_{,t[\chi]} + f_{,j}\,\frac{\partial x_j}{\partial \chi_i} w_i = f_{,t[\chi]} + f_{,j}\,c_j \tag{2.67}$$

The governing equations can then be expressed as follows:

Conservation of mass:

$$\dot{\rho} + \rho v_{k,k} = 0 \quad \text{or} \quad \rho_{,t[\chi]} + \rho_{,i}\,c_i + \rho v_{k,k} = 0 \tag{2.68}$$

Conservation of linear momentum:

$$\rho \dot{v}_i = \rho \left(v_{i,t[\chi]} + v_{i,j} c_j \right) = \sigma_{ji,j} + p b_i \tag{2.69}$$

Conservation of angular momentum

$$\sigma_{ij} = \sigma_{ji} \tag{2.70}$$

Conservation of energy:

$$\rho(E,_{t[\chi]} + E,_i c_i) = \sigma_{ij} D_{ij} + b_i v_i + (k_{ij}\theta,_j),_i + \rho s \tag{2.71}$$

where

$\frac{Df}{Dt}$	is the material time derivative
c	is the convective velocity
θ	is the temperature
k	is the thermal conductivity of the material

2.4.6 Numerical Implementation of ALE

In this section an overview of the numerical implementation of the Arbitrary Lagrangian Eulerian formulation in LS-DYNA are given. The theory in this section is taken from the LS-DYNA theory manual if not stated otherwise.

2.4.6.1 Operator Split Technique

As explained earlier, the ALE formulation may be thought of as an algorithm that performs automatic rezoning of the mesh. In theory, the ALE formulation contains the Eulerian formulation as a subset, because an ALE calculation without the rezoning would simply be a Eulerian formulation. Most ALE implementations only allow one single material in each element, this greatly speeds up the calculation process. In a single material ALE formulation LS-DYNA first computes the Lagrangian time derivative and updates the history variables. Subsequently the relative motion between the mesh and material is computed, and then the history variables are updated once more. This is also called an operator split technique and is illustrated in figure 2.18.

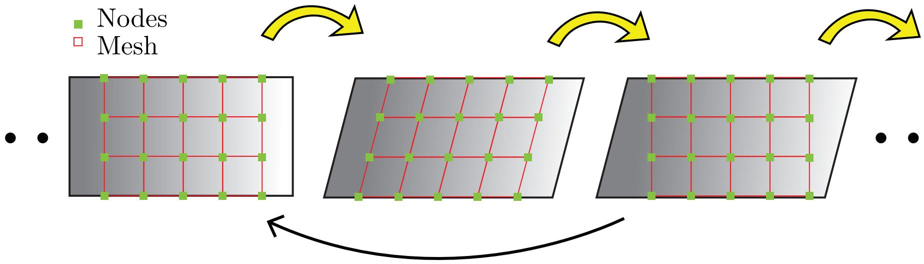

Figure 2.18: Operator split technique

The overall flow of an single material Euler/ALE timestep is as follows:

1. Perform a Lagrangian time step.
2. Perform mesh smoothing.
   (a) Decide which nodes to move.
   (b) Move the boundary nodes.
   (c) Move the interior nodes.
3. Perform an advection step.
   (a) Calculate the transport of the element-centered variables.
   (b) Calculate the momentum transport and update the velocity.

2.4.6.2 Mesh Smoothing

The repositioning of the nodes is referred to as the mesh smoothing process. In an Eulerian formulation the nodes are moved back to their initial position while in an ALE analysis, they are moved back such that the mesh does not possess severe distortions. Most problems associated with the mesh smoothing process are when complicated boundaries are present. It is important for the mesh smoothing algorithm not to present a crude mesh where a good refinement is needed to accurately represent the final solution. In LS-DYNA there are essentially two ways of repositioning the nodes in a single material ALE formulation:

1. Force a set of nodes to stay on a straight line between two master nodes, also often referred to as the direct method. The forcing is done in the parametric domain to conserve the correct ratio of distances between the nodes. The direct method is illustrated in figure 2.19

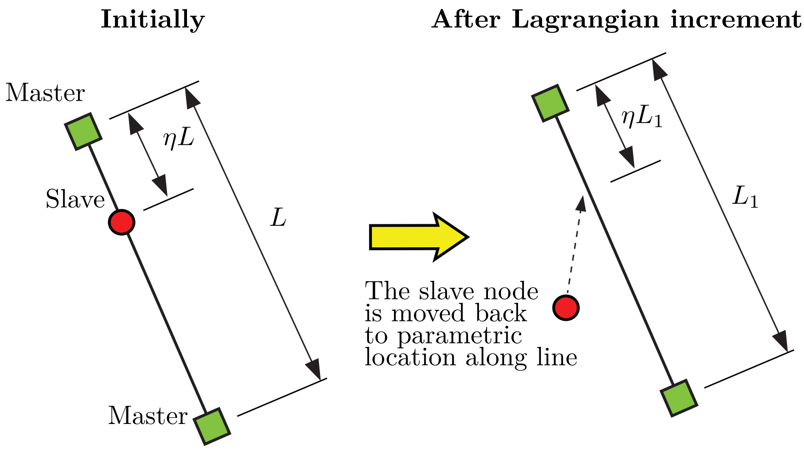

Figure 2.19: Direct Method [40]

2. An iterative mesh smoothing algorithm. This can be done in several different ways, but the most useful methods implemented in LS-DYNA are called the Simple average method illustrated in figure 2.20 where the coordinates for the node to be moved is the average of the coordinates of the surrounding nodes. The Equipotential smoothing algorithm is harder to visualize but the new node placements are obtained by solving Laplace's equation in the parametric domain.

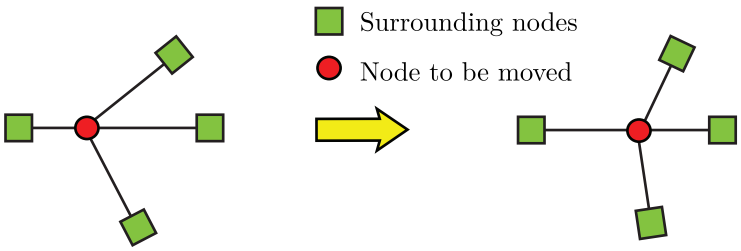

Figure 2.20: Simple average [40]

2.4.6.3 The Advection Step

The re-mapping of the solution variables on to the new configuration is called the advection step, and this is the process that is associated with the largest portion of the numerical errors in an ALE analysis. In LS-DYNA there are two different advection algorithms; the first order accurate Donor Cell scheme and the second order accurate Van Leer scheme. Both methods utilize the half index shift scheme for advection of node centered variables (velocities and temperatures). Because a perfect fit of the solution variables is generally not possible within a reasonable timeframe, a compromise between speed and accuracy has to be done to ensure a viable computational time.

The algorithms for performing the remap step are taken from classical computational fluid dynamics. They are referred to as advection algorithms after the first order, scalar conservation equation that is frequently used as a model hyperbolic problem:

$$\frac{\partial \phi}{\partial t} + a\left(x\right)\frac{\partial \phi}{\partial x} = 0 \tag{2.72}$$

A good advection scheme should be monotonic, conservative and as little dissipative and dispersive as possible. What the four attributes imply is presented in the subsequent paragraphs. It is also important to note that the algorithm should be as accurate as possible and stable when the timestep employed is below a critical value. Although many of the solution variables such as the stress and plastic strain are not governed by the conservation equations like momentum and energy, it is still highly desirable that the volume integral of all the solution variables remain unchanged by the remap step [32]. This is especially important for the mass and energy conservation equations because negative values would lead to physically unrealistic solutions.

Monotonic

A monotonic advection scheme is a numerical implementation that does not introduce higher maximum values or smaller minimum values in the history variable fields. This is presented mathematically as:

$$\max_{x \in V}\left(\phi^{new}\right) \leq \max_{x \in V}\left(\phi^{old}\right) \tag{2.73}$$

$$\min_{x \in V}\left(\phi^{new}\right) \geq \min_{x \in V}\left(\phi^{old}\right) \tag{2.74}$$

This is an important condition to ensure that no non-physical or unrealistic effects can alter the final solution.

Conservative

If an advection scheme is conservative it does not change the total mass, momentum or volume of the system. This condition ensures that the fundamental conservation equations expressed in equation 2.67 to 2.71 holds. Expressed mathematically as:

$$\int_V \phi^{new} dV = \int_V \phi^{old} dV \tag{2.75}$$

Dissipative

The advection algorithm should strive to minimize the dissipative effects. A strong dissipative algorithm smears out the solution variable fields in time.

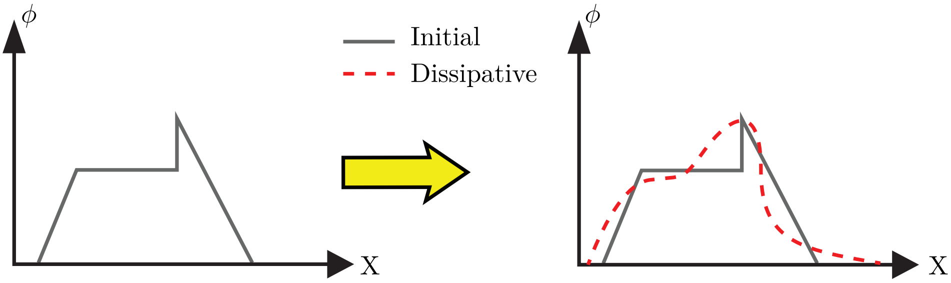

Figure 2.21: Dissipative [40]

Figure 2.21 illustrates a wave moving through a mesh in the x direction. As the dissipative effect increases, the wave gets smeared out in time.

Dispersion

A dispersive error occurs when the different frequencies travels at different speeds. Dispersion errors originate from the fact that different solution variables with different frequencies don't necessarily have the travel at the same speed, and this balance may be shifted if not treated carefully. Dispersion of high frequencies can often be counteracted by employing a dissipative scheme that damps out higher frequencies.

Below follows an outline of the numerical implementation of the two advection schemes in LS-DYNA.

The First Order Donor Cell Scheme

The Donor cell scheme is monotonic, conservative and fast. However there is a big drawback that the scheme is only first order accurate and has large dissipative errors. This severely limits the usefulness of this scheme. In theory, the Donor cell scheme is also dispersive, but the errors are often camouflaged by very strong dissipation, thus high frequencies that travel too slow are quickly damped out. This scheme is an upwind method, meaning that the scheme uses data from the upstream convective velocity a_j, thus the flux f_j^ϕ is dependent on the sign of a at node j which defines the upstream direction. The scheme only collects information from elements that share common sides and utilizes internal averaging making the advected variables the volume weighted average of their projection on to the new mesh. The donor cell algorithm therefore assumes that the distribution of ϕ is constant over the element.

Mathematically the Donor Cell Scheme is formulated as:

$$\phi_{j+\frac{1}{2}}^{n+1} = \phi_{j+\frac{1}{2}}^{n} + \frac{\Delta t}{\Delta x}\left(f_j^\phi - f_{j+1}^\phi\right) \tag{2.76}$$

$$f_j^\phi = \frac{a_j}{2}\left(\phi_{j-\frac{1}{2}}^{n} + \phi_{j+\frac{1}{2}}^{n}\right) + \frac{|a_j|}{2}\left(\phi_{j-\frac{1}{2}}^{n} - \phi_{j+\frac{1}{2}}^{n}\right) \tag{2.77}$$

where

f_j^ϕ	is the flux or the so-called transport volume of between two adjacent elements.
a_j	is the convective velocity or the velocity of the contact discontinuity at node j.

The advection algorithm stems from a first order Godunov method applied to the advection equation (2.72). The Donor cell scheme for one and two dimensions are illustrated in figure 2.22 and 2.23.

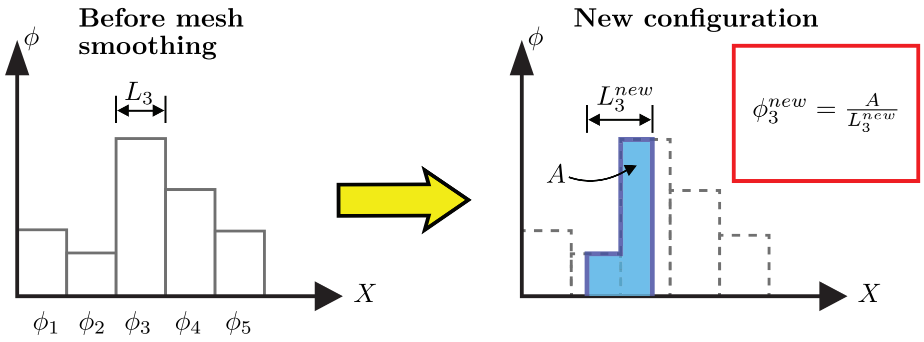

Figure 2.22: The donor cell advection scheme in one dimension [40]

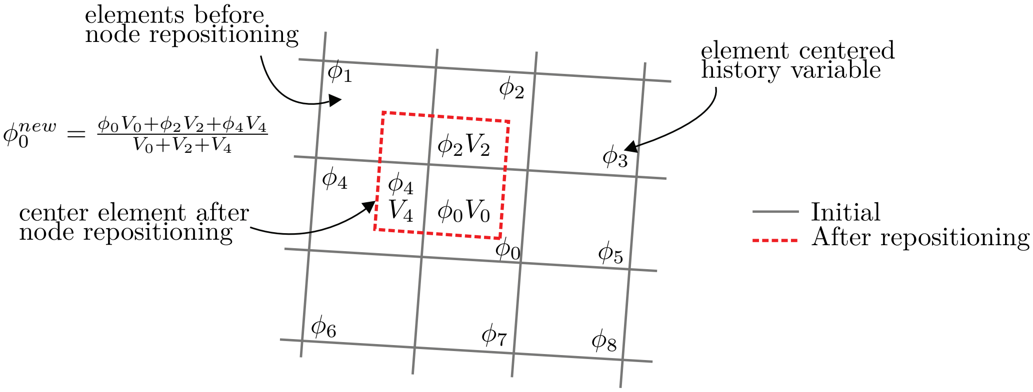

Figure 2.23: The donor cell advection scheme in two dimensions [40]

The Second Order Van Leer Scheme

The van Leer scheme is monotonic, conservative and second order accurate. This comes at the drawback of a much higher computational cost compared to the donor cell method. It is based on the assumption of a mesh consisting of rectangular elements. In most cases, severe element distortion or the enforcing of monotonicity introduce second order errors terms and the scheme is in reality reduced to a first order numerical scheme [32].

The basic idea is to reconstruct an assumed linear variation of the history variable fields. The assumed fields are mapped from the old mesh on to the new configuration. Where the donor cell scheme assumed piecewise constant distribution of ϕ over the element, the Van Leer replaces the piecewise constant distribution with a higher order interpolation function $\phi^n_{j+\frac{1}{2}}(x)$ that is subject to an element level conservation constraint. The value of ϕ at the element centroid is regarded in this context as the average value of ϕ over the element instead of the spatial value at $x^n_{j+\frac{1}{2}}$ (if the field is assumed linear).

$$\phi^n_{j+\frac{1}{2}} = \int_{x_j}^{x_{j+1}} \phi^n_{j+\frac{1}{2}}(x)dx \tag{2.78}$$

Generally the $\phi^n_{j+\frac{1}{2}}(x)$ function can be of any numerical order, but introducing a function of a high order will result in an extremely cumbersome numerical scheme that will prove to be too expensive to solve effectively, therefore $\phi^n_{j+\frac{1}{2}}(x)$ is almost always assumed as a linear function.

The assumed piecewise linear functions are found from the classical central difference method where x now is the volume coordinate. The volume coordinate of a point is simply the volume swept along the path between the element centroid and the point itself. Conservation of volume is guaranteed by expanding the linear function about the element centroid.

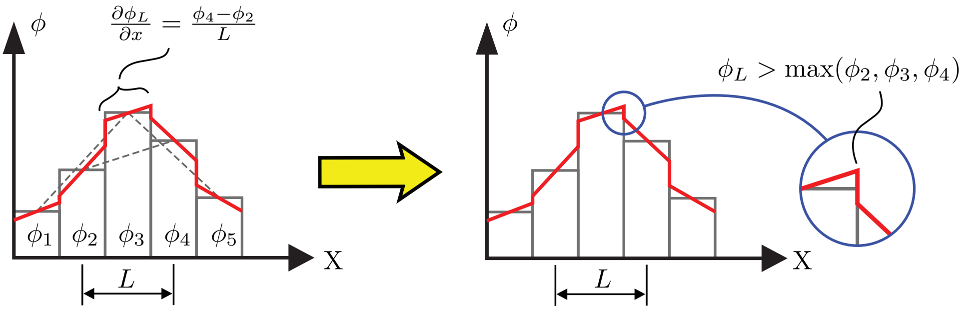

Figure 2.24: The second order Van leer advection scheme [40]

As we can see from figure 2.24 the resulting linear field might become non-monotonic such that:

$$\phi_i^{new} > \max_{i=1,nel}(\phi_i) \tag{2.79}$$

To counteract this, the numerical scheme can enforce monotonicity in one of two different ways.

The easiest and least accurate method is to determine the maximum and minimum allowed slopes to the left and to the right of node $\phi^n_{j+\frac{1}{2}}$ and the force $\phi^n_{j+\frac{1}{2}}(x)$ to fall in between this range by employing the following equation:

$$\frac{\partial \phi_L}{\partial x} = \frac{1}{2}(sgn(s^L) + sgn(s^R)) \cdot \min(\left|s^L\right|, \left|s^R\right|, |S|) \tag{2.80}$$

where

s^L	is the slope to the left of $\phi^n_{j+\frac{1}{2}}$
s^R	is the slope to the right of $\phi^n_{j+\frac{1}{2}}$
S	is the slope across $\phi^n_{j+\frac{1}{2}}$ from $\phi^n_{j-\frac{1}{2}}$ to $\phi^n_{j+\frac{3}{2}}$

This is illustrated in figure 2.25

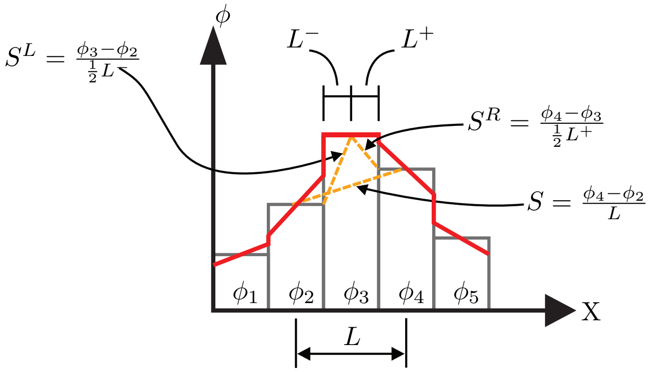

Figure 2.25: the enforcing of monotonicity with the second order Van Leer scheme [40]

The second and more elegant method is to restrict the average value of ϕ in the transport volumes associated with element $j + \frac{1}{2}$. The latter definition allows the magnitude of the ϕ transported to adjacent elements to be larger than the first formulation. And as a result the second method is more able to transport solutions with large discontinuities. Figure 2.26 summarizes the second order Van Leer advection scheme.

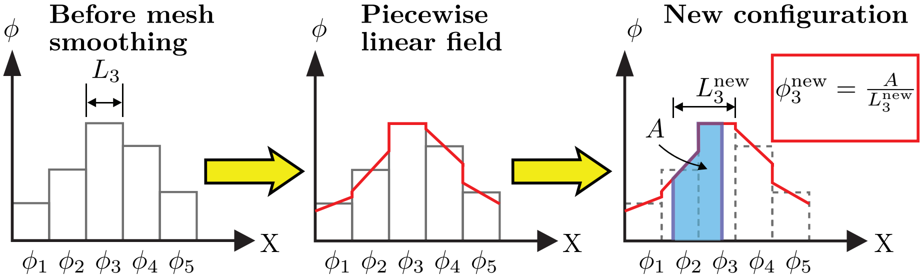

Figure 2.26: Summary of the second order Van Leer advection scheme [40]

Half Index Shift

While the two aforementioned advection algorithms work well for element centered variables such as stresses and strains, they have to be modified to advect node associated variables such as velocity without being non-conservative. LS-DYNA advects momentum instead of velocity to guarantee that the algorithm stays conservative. To advect the momentum an auxiliary set of element-centered variables are constructed from the velocity, and then advected by employing one of the two standard advection schemes. Then the algorithm has to reconstruct the new velocities from the auxiliary variables. This process is called the Half Index Shift algorithm and is quite cumbersome numerically.

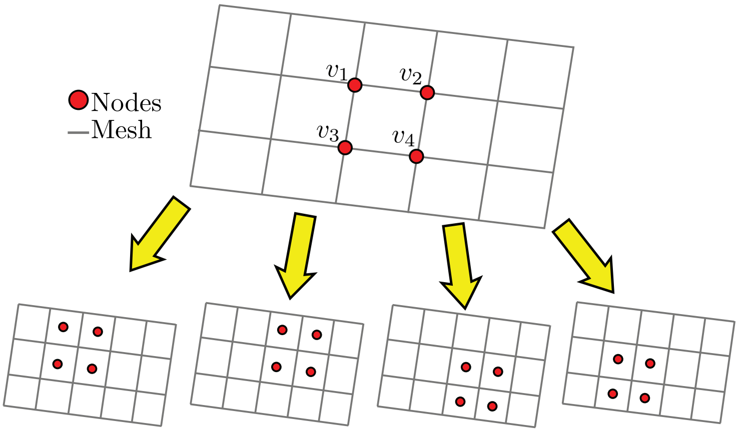

Figure 2.27: The half index shift algorithm employed to advect the node associated variables [40]

As is illustrated in figure 2.27, the half index shift algorithm is used to transport the nodal velocities to the integration points of the surrounding elements (four different positions for two dimensions, eight different positions for three dimensions). Subsequently they are advected by employing the standard Donor cell or van Leer scheme. Then the new velocities are transported back to the nodes.

2.4.6.4 Critical Time Step Size

Due to the implemented advection schemes, the mass flux velocity influence the critical time step size in equation (2.42) The new critical time step is now bounded by two conditions:

$$\Delta t_{cr} = \min_{nel} \left[\frac{\Delta x^e}{c_d}, \frac{\Delta x^e}{4 v^{flux}} \right] \tag{2.81}$$

$$v^{flux} = \max_i \left(\| v_i - \hat{v}_i \| \right) \tag{2.82}$$

where

Δx^e	is the characteristic length of an element.
c_d	is the dilatational wave speed.
v_i	is the material velocity from equation (2.47).

$\hat{v}_i$ is the mesh velocity from equation 2.64.

The definition of Δt_{cr} ensures that a particle will not flow across more than one quarter of an element in one time step. This is important for the advection accuracy [40].

Typically the cost of an advection step is two to five times that of a Lagrangian time step. By only performing an advection step for every ten Lagrangian steps, the cost of an ALE calculation can often be reduced by a factor of three without adversely affecting the time step size. Generally it is not worth the cost to advect an element unless at least twenty percent of its volume will be transported because the gain in time step size will not offset the cost of the advection calculation [32].

2.4.6.5 Multi-Material ALE

In the previous section we covered the single material ALE formulation where only one material is present in the movable mesh. LS-DYNA contains a Multi-Material Arbitrary Lagrangian Eulerian (MMALE) formulation that allows for different materials such as steel and air to be present in the same element. This is particularly useful for problems where multiple gasses are mixing or where the boundary between a gas and a fluid with large deformations needs to be modelled. This formulation can contain a mixture of fluids moving through an Eulerian mesh that is also moving relative to a fixed reference frame. This is illustrated in figure 2.28.

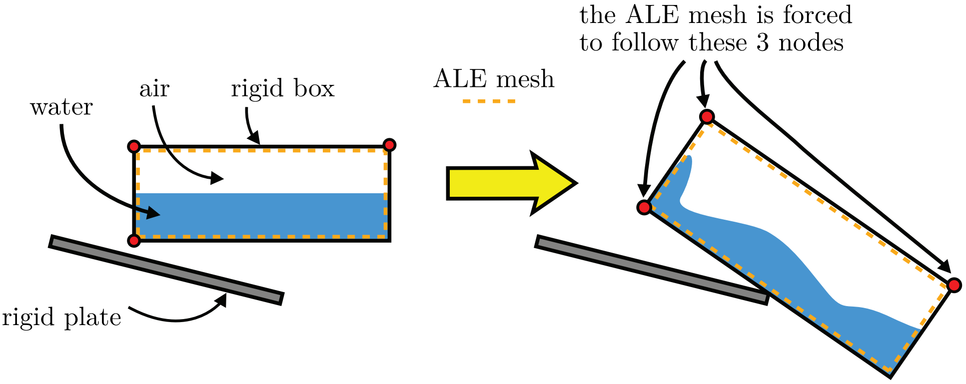

Figure 2.28: Multi-Material ALE formulation [40]

Figure 2.28 illustrates the MMALE formulation where two different materials are deforming inside a shared Eulerian mesh that is also translating with respect to a fixed reference frame. It is also possible for the mesh to deform while it contains multiple materials.

By default, all materials inside one element are assumed being exposed to the same strain rate. This simplification can cause trouble such as drastically dropping the stable time increment and non-physical deformation. LS-DYNA solves this by employing a pressure iteration algorithm together with an interface reconstruction numerical scheme to properly describe how the different materials deform inside the same element. The boundaries between the multiple materials are internally defined as where the volume fraction equals 50%.

In this thesis the MMALE formulation will be utilized to simulate explosives in a Eulerian domain with an equation of state (EOS). The explosive agent needs to be defined as a separate material inside the Eulerian domain, thus a multi-material Euler formulation needs to be employed to properly describe the system behaviour. Because of the almost discontinuous pressure changes when the blast wave propagates in the Eulerian mesh, an extremely small element size is required to properly describe the blast wave behaviour. An MMALE formulation is therefore preferred because it can refine the mesh close to the pressure front as the wave is propagating forward and will lead to a more accurate solution.

2.4.6.6 Fluid Structure Interaction

It is often suitable to treat parts of a model as purely Lagrangian, purely Eulerian or purely ALE. A fluid structure coupling algorithm is needed for the communication between the different parts. There are two different fluid structure coupling algorithms available in LS-DYNA.

Constraint Based Formulation

The constraint based method implemented in LS-DYNA directly modifies the velocities of both the fluid and the structural nodes directly to force them to follow each other. The Eulerian nodes are projected on to the edges of the Lagrangian surface and the mass, force and momentum are lumped on to the Lagrangian structure. The main drawback of the constraint based method is that it does not conserve energy. The constraint based method is illustrated in figure 2.29.

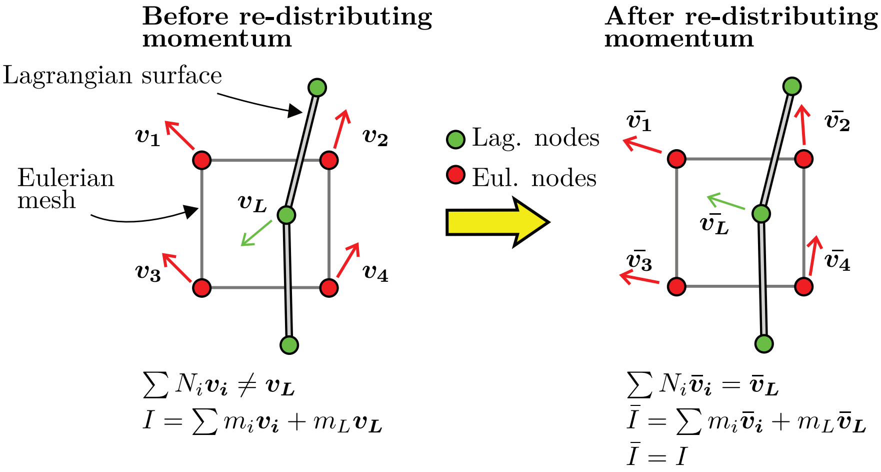

$$\sum N_i \boldsymbol{v_i} \neq \boldsymbol{v_L}$$
$$I = \sum m_i \boldsymbol{v_i} + m_L \boldsymbol{v_L}$$

$$\sum N_i \bar{\boldsymbol{v}}_{\boldsymbol{i}} = \bar{\boldsymbol{v}}_{\boldsymbol{L}}$$
$$\bar{I} = \sum m_i \bar{\boldsymbol{v}}_{\boldsymbol{i}} + m_L \bar{\boldsymbol{v}}_{\boldsymbol{L}}$$
$$\bar{I} = I$$

Figure 2.29: The constraint based FSI algorithm [40]

The Penalty Based Method

The penalty based method are for most problems the preferred FSI coupling algorithm because it conserves energy almost exactly [40]. The algorithm tracks the relative displacement between the fluid and the structure to detect penetration. When penetration is present, interface springs are placed between the penetrating nodes and the contact surface, thus a force is applied to ensure that the fluid-structure interface follows one another. The force applied will be proportional to the magnitude of the relative displacement between the fluid and the structure. The penalty based method is illustrated in figure 2.30.

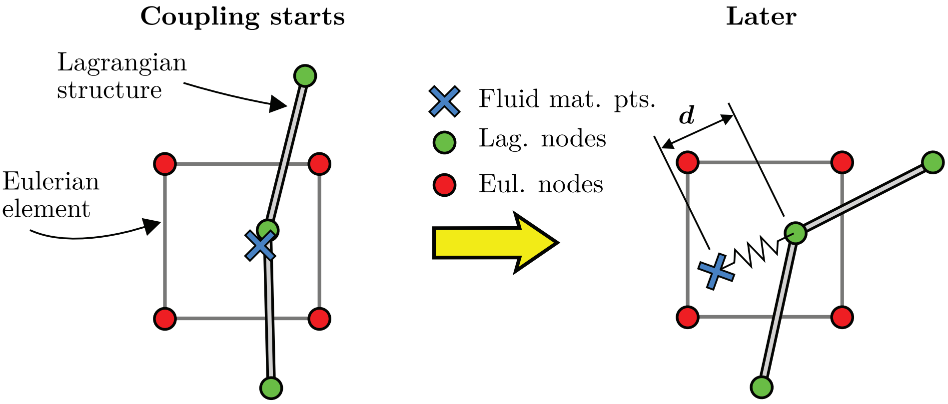

Figure 2.30: The penalty based FSI algorithm [40]

The algorithm does not enforce the contact condition as accurate as the constraint based method, it produces numerical noise and is not as stable, but if it is properly defined it prevails as the method of choice because of energy conservation.

If the algorithm is not defined properly, leakage through the coupling interface might occur. The leakage is either caused by a crude coupling grid or due to numerical errors in the interface reconstruction. Coupling grid refinement or activation of the leakage control option in LS-DYNA should then be considered.

2.4.7 Discrete Particle Method (DPM)

As an alternative to the ALE or FSI formulations, a discrete particle method may be employed. The method is based on modelling a blast simulation or a specific gas behaviour by employing a set of discrete particles. The most obvious advantages include a greatly reduced computational effort and the absence of advection errors compared to an ALE or FSI formulation [41]. The model for the particles is based on kinetic molecular theory where the rigid particles obey Newton's laws of classical mechanics. The gas-structure interactions can be modelled with perfectly elastic collisions in a purely Lagrangian domain, thus eliminating the numerical advection errors and other numerical errors outlined in section 2.4.6.3 that lead to energy dissipation in the ALE formulation [41, 14].

2.4.7.1 Kinetic Molecular Theory

The kinetic molecular theory is a study of gas molecules and their interactions on a microscopic level. This in turn lead to the macroscopic relationship engineers know as the ideal gas law. The theory is based on the four following assumptions [41]:

- The average distance between the molecules is large compared to their size.
- There is a thermo-dynamical equilibrium, i.e the molecules are in random motion
- The molecules obey Newton's laws of classical mechanics
- The only molecule-molecule and molecule-structure interactions are perfectly elastic conditions.

The molecular theory was first proposed in 1738 by Daniel Bernoulli [9, 8] when he proposed that air pressure against a surface can be decomposed in to discrete molecular collisions. Later on in 1860 James Clerk Maxwell derived an expression for the molecular velocity distribution for a gas at thermal equilibrium [41, 37].

The ideal gas law serves as a base for these derivations:

$$PV = nRT \tag{2.83}$$

where

P	is the pressure
V	is the volume
n	is the number of molecules $[mol]$
R	is the universal gas constant
T	is the absolute temperature

In blast mechanics, it is important to describe the pressure accurately. From the kinetic molecular theory it is possible to derive the pressure that is exerted on to a surface from one particle when an elastic collision occurs. The average pressure against a wall at $x = L_x$ from a particle collision with the wall (see figure 2.31) can be expressed as [41]:

$$P_{x,i} = \frac{m_i \left|v_{x,i}\right|^2}{L_x L_y L_z} = \frac{m_i \left|v_{x,i}\right|^2}{V} \tag{2.84}$$

where

m_i	is the mass of particle i.
$v_{x,i}$	is the velocity in the x direction of particle i
V	is the volume $L_x \times L_y \times L_z$

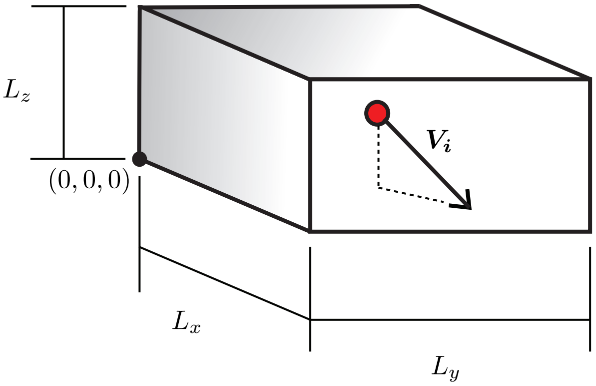

Figure 2.31: Molecule collision [40]

With N molecules, the pressure in the x direction can be summed up as:

$$P_x = \frac{1}{V}\sum_{i=1}^{N} m_i \left|v_{x,i}\right|^2 \tag{2.85}$$

In a thermal equilibrium, the kinetic energy is evenly distributed in all Cartesian direction, such that:

$$P_x = P_y = P_z = P = \frac{2W_k}{3V} = \frac{2}{3}w_k = \frac{nMv_{rms}^2}{3V} \tag{2.86}$$

where

W_k	is the total translational kinetic energy of all the molecules in the system
w_k	is the specific translational kinetic energy per unit volume
M	is the molar mass

v_{rms}	is the root-mean-square acceleration

If equation (2.86) is combined with equation (2.83), we arrive at the following expression for the root-mean-square acceleration

$$v_{rms} = \sqrt{\frac{1}{N}\sum_{i=1}^{N}|v_i|^2} = \sqrt{\frac{3RT}{M}} \tag{2.87}$$

From Maxwell's statistical descriptions, it is possible to derive quantities such as the mean free path and frequency of collisions that in turn are significant parts of the discrete particle formulation. The Maxwell-Botzmann distribution of molecular velocities in an ideal gas is based on the assumption that the velocity distribution in orthogonal directions are uncoupled [41], thus the velocity in x direction is not a function of the velocity in the y direction and vice versa. From this single assumption it is possible to show that the molecular velocity distribution at thermal equilibrium is [37]:

$$f(v) = 4\pi\left(\frac{M}{2\pi RT}\right)^{\frac{3}{2}} v^2 \exp\left[-\frac{Mv^2}{2RT}\right] \tag{2.88}$$

The root-mean-square velocity at thermal equilibrium can then be calculated as the integral [41, 42]:

$$v_{rms} = \sqrt{\int_0^\infty v^2 f\left(v\right) dv} \tag{2.89}$$

It is important to note that the thermal velocity v_{rms} should not be confused with flow velocity. For illustrative purposes, air molecules at room temperature typically have a root-mean-square velocity of roughly 500 m/s [42].

The frequency of collision can be derived from equation (2.88):

$$f_c = n_v r_p^2 \sqrt{\frac{8\pi RT}{M}} \tag{2.90}$$

where

r_p	is the molecular radius
n_v	is the number of molecules per unit volume

The mean-free-path I of a molecule is also derived from Maxwells statistical descriptions

$$I = \frac{1}{\sqrt{2}\pi n_v r_p^2} \tag{2.91}$$

Macroscopically the translational kinetic energy per unit volume w_k is a fraction of the specific internal energy $e = \rho C_v T$ of the gas [41]. If one were to assume that the heat capacities are temperature independent, the following relation holds:

$$P = \frac{2}{3} w_k = (\gamma - 1)e = (\gamma - 1)\rho C_v T \tag{2.92}$$

It is important to note that the internal energy in an ideal gas can be divided in to translational kinetic energy, vibration energy and spin, but it is only the translational kinetic energy that produces the pressure. The fact that the vibration and spin energy does not contribute to the pressure allows the analyst to model the same pressure with a reduced number of particles as long as the total mass of the particles m_{tot} and v_{rms} stays constant. This is fundamental for the discrete particle method implemented in a computer code, because simulating every single molecule would be computationally extremely expensive.

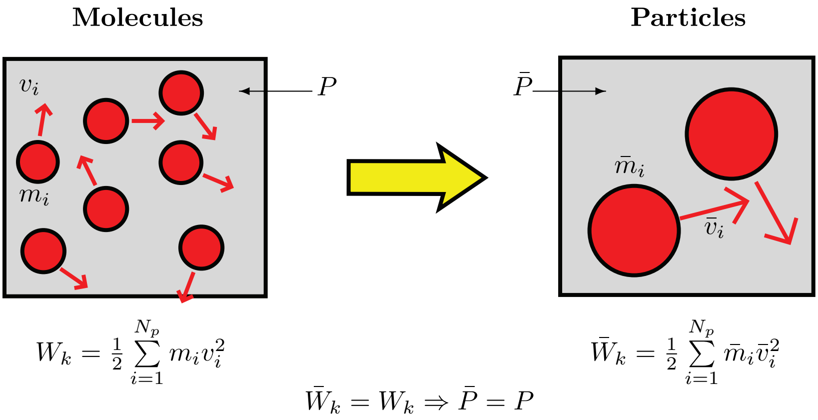
Molecules

Particles

$$W_k = \tfrac{1}{2}\sum_{i=1}^{N_p} m_i v_i^2 \qquad \bar{W}_k = \tfrac{1}{2}\sum_{i=1}^{N_p} \bar{m}_i \bar{v}_i^2$$

$$\bar{W}_k = W_k \Rightarrow \bar{P} = P$$

Figure 2.32: A reduced number of particles represent the same pressure [41]

2.4.7.2 Numerical Implementation of the Discrete Particle Method

As stated earlier, the discrete particle method is purely Lagrangian. The simple formulation of the fluid flow makes it easy to define and numerically robust [41]. The numerical implementation in IMPETUS takes in to account co-volume effects, and in addition the interaction between the gas particles allows the quota of translational energy and rotational energy to change during the course of the simulation. This leads to a much more complex interaction between the gas particles than described in the previous section, but the fundamentals remain the same. The discrete particle method employed in this thesis is implemented in the finite element code IMPETUS.

Depending on the molecular weight, the number of molecules per gram of detonation product is in the range of $10^{22} - 10^{23}$ molecules [42]. It is therefore impossible to simulate every molecule within a reasonable timeframe. The need for computational efficiency in the numerical implementation has led to the following assumptions and deviations from the kinetic molecular theory [41, 42, 28]:

- The particles are given a spherical shape to speed up contact treatment
- The particles are assumed rigid
- Each particle represents many molecules. Typically $10^{15} - 10^{20}$ depending on application
- To obtain a smoother pressure distribution, the impulse transfer from particle collisions is slightly smeared out in time.

2.4.7.3 The Discrete Particle Method for Blast Applications

The discrete particle method has several advantages over a full ALE analysis both when it comes to efficiency, advection errors and severe contact problems [14]. Because it is impossible to simulate every single molecule, some effects will not be as accurately represented as in a continuum formulation. Despite this fact, a good representation of the blast load scenario can be achieved as done in [14] and [42]. It is important to note that as the standoff increase more and more particles are needed to properly describe fluid flow such as a blast wave. For large values of the scaled distance Z, the method is a crude approximation.

Chapter 3

Materials

Proper material models needs to be defined in order to get reliable results from the FE simulations.

3.1 Material Docol 600 DL

The steel plate material used in the upcoming experiments is a cold-rolled, dual phase steel of type Docol 600 DL supplied from Swedish steel AB (SSAB). The nominal yield strength is reported to be in the range of 280 MPa to 360 MPa, and the nominal tensile strength ranges from 600 MPa to 700 MPa [47]. The chemical composition is shown in table 3.1.

Table 3.1: Chemical composition of Docol 600 DL (in wt%) [47]

C	Si	Mn	P	S	Al_{tot}
0.1	0.4	1.5	0.01	0.002	0.04

3.2 Experimental Work

The main focus in this thesis will be numerical simulations, therefore the experimental work with regards to establishing the material model and its attributes will be based on the extensive work done in the doctorate Ductile Fracture in Dual-Phase Steel [26] by Gruben. In his thesis a detailed overview of mechanical testing, theoretical aspects of ductile fracture and numerical simulations on 2.0 mm thick Docol 600 DL plates is found. A comparison of material behaviour for 0.7 mm and 2.0 mm thick Docol 600 DL plates has been performed by Rakvåg [44], that confirmed material isotropy.

Five experiments were conducted in [26] to determine the material paramaters of the Docol 600 DL plates.

(a) Uniaxial tension test
(b) Plane-strain tension test

(c) In-plane shear test
(d) Modified Arcan test set-up with $\beta = 90°$
(e) Modified Arcan test set-up with $\beta = 45°$

The experiments were performed at room temperature with strain rates of approximately $10^{-3}s^{-1}$. For added accuracy, the strain fields were recorded using Digital Image Correlation (DIC), and used as a benchmark for comparing the material model used in the numerical simulation. A comparison of strain fields observed in the experiments and the finite element analysis are shown in figure 3.1 and 3.2.

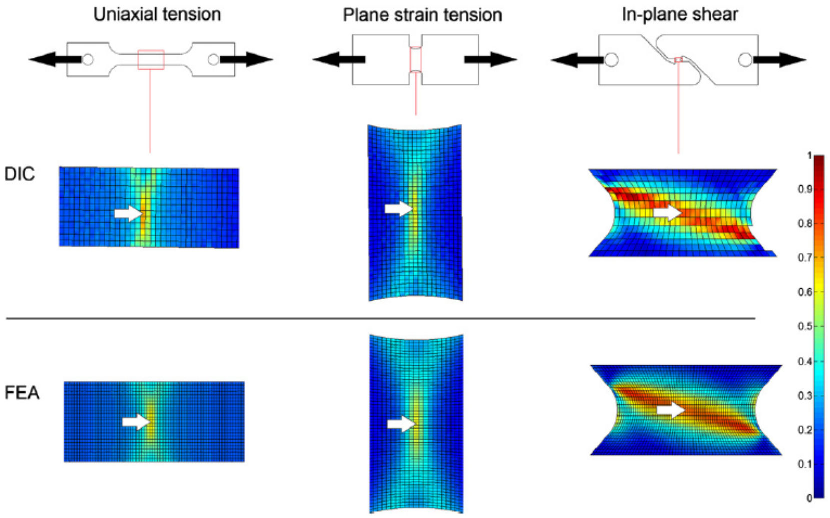

Figure 3.1: Experiment (a) to (c) versus FEA solution comparison [26]

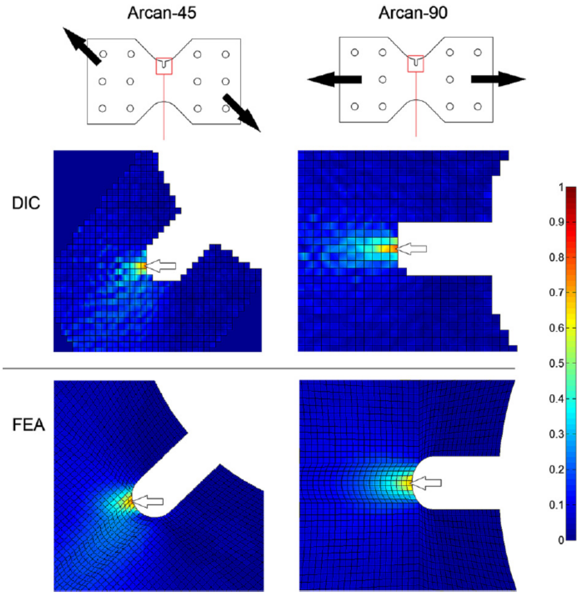

Figure 3.2: Experiment (d) to (e) versus FEA solution comparison [26]

The force-displacement histories from the instruments used in the experiments and strain fields gathered with DIC were used to determine the material model parameters.

3.3 Docol 600 DL Parameters

Based on the work in [26], it is assumed that the material is perfectly plastic and obeying the von Mises yield criterion with the associated flow rule. Nominal elastic properties are described by a Young's modulus of 210 GPa and a Poisson's ratio of 0.33.

As mentioned in [26], appropriate values for the materials strain-rate sensitivity C and $\dot{\epsilon}_{0p}$ are shown to be 0.005 and 0.001 respectively in the work of [53] and [19]. After necking strain rate increases significantly, and delays the evolution of the neck. The strain-rate sensitivity term is added such that it captures this effect.

In order to capture the post-necking behaviour, an iterative method similar to the one used in [6] was implemented. The primary hardening in equation (2.23) saturates for small strains, while the post necking stress is controlled by the secondary hardening. Then an iterative process was performed in order to optimize the material model. This was done by fitting the Voce curve according to the pre-necking results and comparing force-displacement curves from FE-simulations and experimental results. The fitted Voce curve on top of the experimental results are shown in figure 3.3.

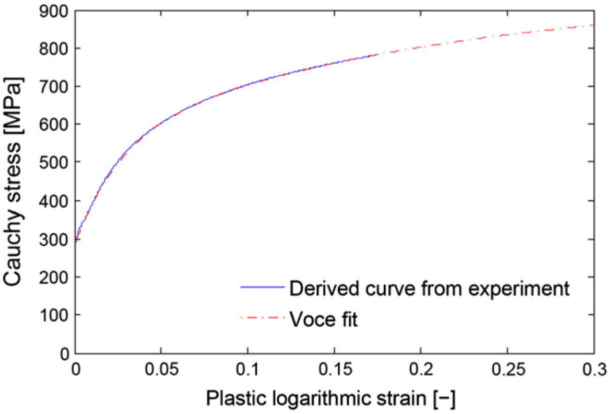

Figure 3.3: Voce versus experimental results [26]

The final Voce and JC coefficients are shown in table 3.2.

Table 3.2: Voce Coefficients [26, 44]

σ_0 [MPa]	Q_1 [MPa]	C_1	Q_2 [MPa]	C_2	$\dot{\epsilon_{0p}}$	C
283.3	268.3	39.38	396.6	5	0.001	0.005

As seen in table 3.2, the yield strength range of 280 MPa to 360 MPa stated in the supplied SSAB datasheet [47] corresponds quite well with the observed yield strength of 283.3 MPa. This also applies for the supplied tensile strength indicated in the range of 600 MPa to 700 MPa compared to the observed in the derived curve from the experiment (figure 3.3).

Additional material data used in LS-DYNA MAT_107 is based on Hallset and Haagenruds thesis in 2011 [27] and are shown in table 3.3.

Table 3.3: Additional material data for Docol 600 DL [27]

Coeff.	LS-DYNA var.	Value	Description	Units
ρ	ro	7850	Density of steel	$[\frac{kg}{m^3}]$
χ	xsi	0.9	Taylor-Quinnery coefficient	$[-]$
c_p	cp	452	Specific heat capacity for constant P	$[\frac{J}{kgK}]$
α	alpha	1.2E-5	Thermal expansion coefficient	$[K^{-1}]$
t_r	tr	293	Room temperature	$[K]$
t_m	tm	1800	Material melting temperature	$[K]$
t_0	t0	293	Initial temperature	$[K]$
D_c	dc	1	Critical damage parameter	$[-]$
W_{cr}	pd/wc	7.48E8	Critical CL parameter	$[Pa]$
T_c	tc	1650	Critical temperature par.	$[K]$
τ_c	tauc	1E20	Critical shear stress par.	$[-]$

3.4 Fluid Parameters

To accurately describe air behaviour in LS-DYNA, a proper definition of fluid parameters needs to be established using input cards MAT_NULL and EOS_LINEAR_POLYNOMIAL. The parameters in table 3.4 are based on data found in [44].

Table 3.4: EOS_LINEAR_POLYNOMIAL and MAT_NULL parameters for air [44]

ρ_{air} $[kg/m^3]$	C4 [-]	C5 [-]	E0 $[J/m^3]$	V0 [-]
1.25	0.4	0.4	2.5E5	1.0

3.5 Explosives Parameters

In order to simulate the explosive process in LS-DYNA, a proper definition of the explosive agent needs to be addressed. The parameters are employed in LS-DYNA using the input cards MAT_HIGH_EXPLOSIVES_BURN and EOS_JWL. The parameters in table 3.5 and 3.6 are based mainly on data from [14], and supplemented by findings in [17] and [44]. Coefficients not included in this section are not tampered with, thus set to default values or simply set to zero.

Table 3.5: EOS_JWL parameters for C4 [14]

A [Pa]	B [Pa]	R_1 [-]	R_2 [-]	ω [-]	$E0$ $[J/m^3]$
5.974E11	1.39E10	4.5	1.5	0.32	8.7E9

Table 3.6: MAT_HIGH_EXPLOSIVE_BURN parameters for C4 [14], [17] and [44]

ρ_{C4} $[kg/m^3]$	D [m/s]	PCJ [Pa]	β [-]	k [-]	g [-]
1601	8190	2.8E10	2	1	1

Chapter 4

Experimental Work

The experiments covered in this thesis will serve as benchmarks for the numerical simulations in chapter 7. Three separate experiments are presented in this thesis

- Experiments performed by Rakvåg in 2009 [44] at NTNU (section 4.1.3)
- Experiments performed in connection with this thesis (2013) at NTNU (section 4.1.4)
- Experiments performed by Rakvåg in 2010 at Raufoss [44] (section 4.2)

4.1 Experiments at NTNU

4.1.1 Introduction

SIMLabs two-stage compressed gas gun was used to simulate blast loading. It is primarily intended for penetration studies, and was designed and built at NTNU, Department of Structural Engineering, in close collaboration with the Norwegian Defence Construction Service, Central Staff, Technical Division (FBT). At the time it was built in the mid 1990s, it was the first of its kind in Norway. The gas gun is capable of launching a 0.25 kg projectile to a velocity of 1000 m/s [11]. The gas gun is shown in figure 4.1.

Figure 4.1: Experimental rig

4.1.2 Gas Gun Description

A schematic of the test set-up is shown in figure 4.2. The main components are the pressure tank, the firing section, the barrel, the impact chamber and the support. The pressure tank has an internal volume of 20 litre and is made of stainless steel. The barrel is 9.6 m long (figure 4.3), and is comprised of a stainless, acid-proof steel (AISI 316L). The internal diameter of the barrel was measured to be 50.32 mm in [11]. The impact chamber consists of a 16 m^3 large tank, 4 meters long with an outer diameter of 2.4 meters, whereas the wall-thickness in all parts of the tank is 25 mm, where only St52-3N steel has been employed.

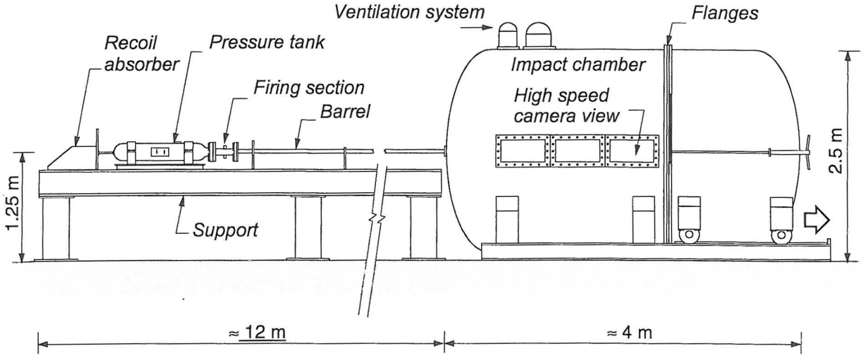

Figure 4.2: Experimental rig setup [11]

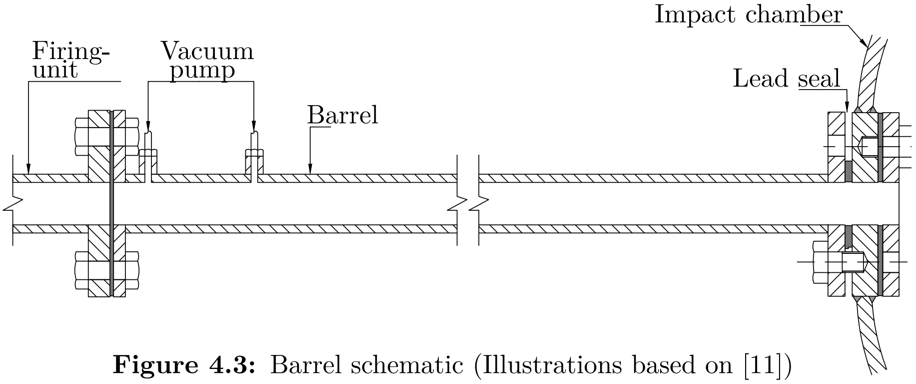

Figure 4.3: Barrel schematic (Illustrations based on [11])

The gas gun was originally intended to be used for penetration studies with ballistics. It was later modified to be able to simulate blast loading. Mylar membranes are placed on either side of the firing section, and then air is pumped in to the pressure tank and the firing section. When half of the desired pressure is reached in both the main tank and the firing section, the air valve for the firing section is closed such that the pressure stays constant in the firing tank. Pressure continues to build up in the main tank until the desired pressure is reached. To fire the gas gun, the pressure in the firing section is released, causing the membranes to rupture and the pressure is released in to the barrel. The mylar membranes are designed to break on a specified pressure gradient, such that by inserting membranes that ruptures at a pressure gradient approximately 50% larger than half of the desired pressure, the firing of the gun can be controlled by the evacuation valve. For the simulation of blast loads the barrel will be filled with air at 1 atm, which means that the vacuum pumps depicted in figure 4.3 are not used. The firing of the gas gun is illustrated in figure 4.4 and 4.5.

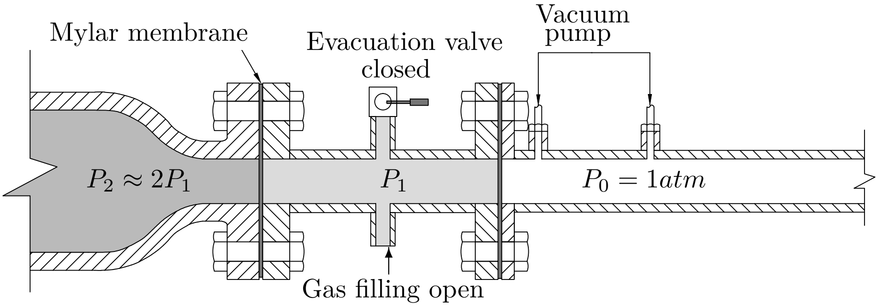

Pressure gradient: $\bar{P} = P_2 - P_1 \approx P_1$

Figure 4.4: Firing section gas filling (Illustrations based on [11])

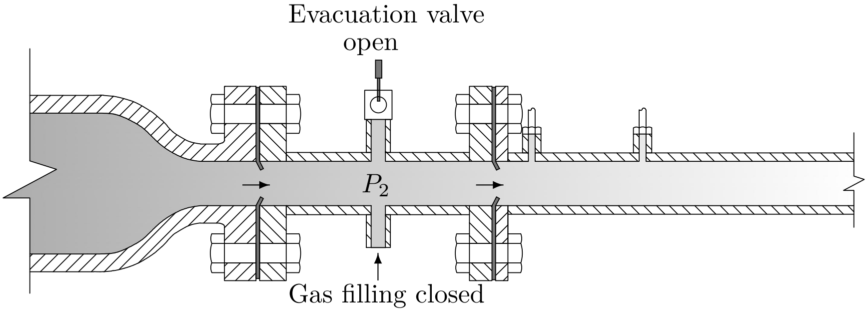

Pressure gradient: $\bar{P} = P_2 \Rightarrow$ Membrane ruptures

Figure 4.5: Firing section release mechanism (Illustrations based on [11])

4.1.3 Experiments Performed at NTNU in 2009

Two sets of experiments were performed in 2009:

- Measuring reflected pressures
- Plate loading

4.1.3.1 Experiment Rig

The gas gun experiments were conducted by fixing a frame approximately 35 cm from the muzzle of the barrel (as shown in figure 4.6).

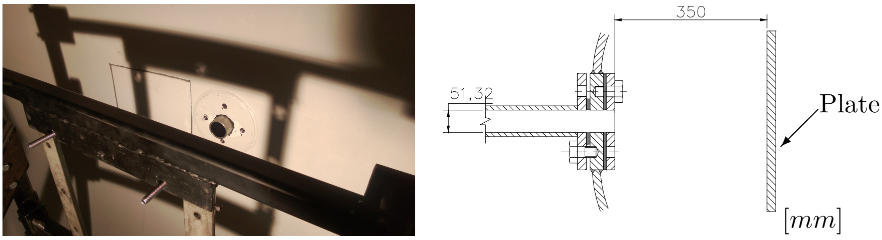

(a) Picture of rig in 2009 **(b)** Rig schematic 2009

Figure 4.6: 2009 experiment overview

Measuring Reflected Pressure

The reflected pressure generated by the gas gun is measured using pressure transducers fixed in a rigid plate (shown in figure 4.7a), and positioned such as illustrated in figure 4.7b.

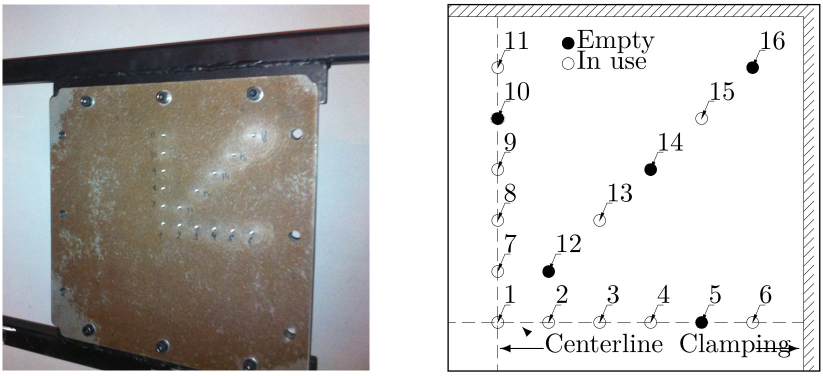

(a) Pressure transducers positioning

(b) Pressure transducer numbering

Figure 4.7: Pressure readings setup 2009 (As seen from behind)

Plate Loading

The plates used in experiments are 0.7mm thick 340mm x 340mm Docol 600 DL steel plates (example shown in figure 4.8) using boundary conditions shown in figure 4.9.

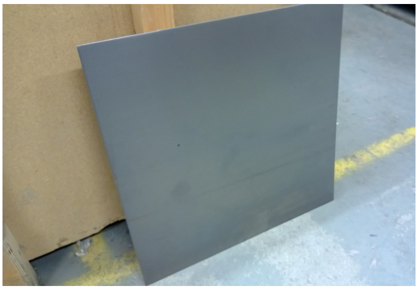

Figure 4.8: Docol 600 DL steel plate

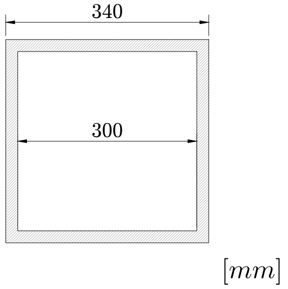

Figure 4.9: Plate boundary conditions (2009)

The plates are positioned in between the frames with enough slack such that they are not pinched.

4.1.3.2 Experiment Procedure

Measuring Reflected Pressure

A series of experiments employing 5, 10, 15, 20, 30 and 40 bar in the main tank of the gas gun was performed. See section 5.1.1 for results.

Plate Loading

Only the experiments resulting in permanent deflections are considered, thus only the 40 bar pressure experiment is presented in this thesis.

4.1.4 Experiments Performed at NTNU in 2013

Previous work by Rakvåg [44] shows that the peak pressure levels are subject to stagnation. In order to combat the peak pressure stagnation the barrel was retrofitted with a funnel, shown in figure 4.10.

4.1.4.1 Experiment Rig

The experiment rig used in 2013 is the same as used in 2009, only retrofitted with a funnel.

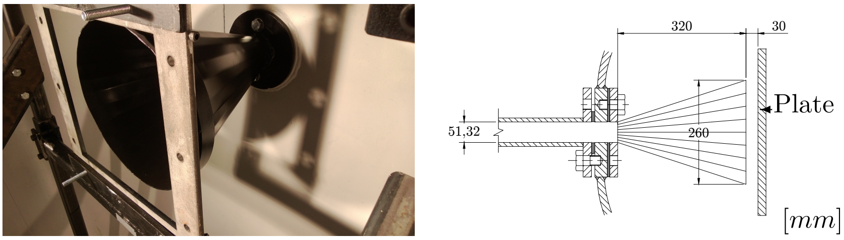

(a) Barrel extended with a funnel (2013) **(b)** Rig 2013 schematic

Figure 4.10: Experiment overview

Measuring Reflected Pressure

The reflected pressure readings set-up will be similar to the experiments performed in 2009, illustrated in figure 4.7. The only modification is the retrofitted funnel.

Plate Loading

The plates subjected to loading are similar to the ones used in 2009 (see section 4.1.3 and figure 4.8). The plate boundary conditions are modified, illustrated in figure 4.11. The plates are 390mm x 390mm in order to fit better with the new boundary conditions used in this thesis.

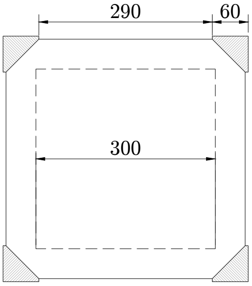

Figure 4.11: Plate boundary conditions (2013)

4.1.4.2 Experiment Procedure

Measuring Reflected Pressure

A series of experiments (similar to the ones presented in 4.1.3) were performed using various pressures ranging from 5 bar to 30 bar in the main tank. Additional experiments were performed using the main tank only and the firing section only, in order to investigate their individual impacts on reflected pressure readings (illustrated in 4.5).

Table 4.1: Test matrix 2013

Pressure $[Bar]$	Main tank only	Firing section only	Normal set-up
5			✓
10	✓	✓	✓
15			✓
20			✓
30			✓

See section 5.1.1 for results.

Plate Loading

3 successful plate loading experiments were performed at the following pressures:

Table 4.2: Plate loading experiment set-up 2013

Pressure $[Bar]$	# of experiments
30	1
40	2

See section 5.1.2 for results.

4.2 Experiments at Raufoss (2010)

Full scale experiments employing real explosives were performed at Raufoss (2010) conducted mainly by Rakvåg and K. O. Hauge from NDEA. Two sets of experiments were performed:

- Side-on pressure measurements based on a ground placed charge.
- Blast loading steel plates.

Cylindrical (130 mm long and with a diameter of 30 mm) C4 charges, at approximately 140-146g were employed. Three different C4 casings were used in the original experiments intended to investigate the effect of fragmentation, however only the naked charges will be investigated in this thesis (illustrated in figure 4.12).

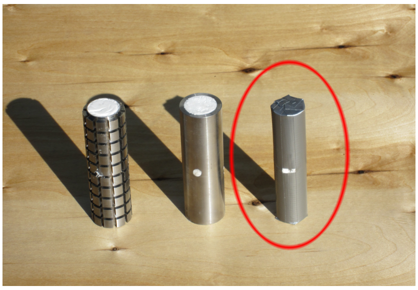

Figure 4.12: Charge types (From left: Pre-frag, Cased and Naked)

4.2.1 Side-on Pressure Experiments

Originally the side-on pressure experiments were intended to be used as a basis for load curves for the related plate loading experiments.

4.2.1.1 Experiment Rig

The rig used for measuring side-on pressure consist of a charge placed on a steel plate, and a small steel tap placed directly in front of the charge in order to prevent the sensors to be hit by debris from the explosion (shown in figure 4.13 and 4.14).

Figure 4.13: Side-on pressure rig

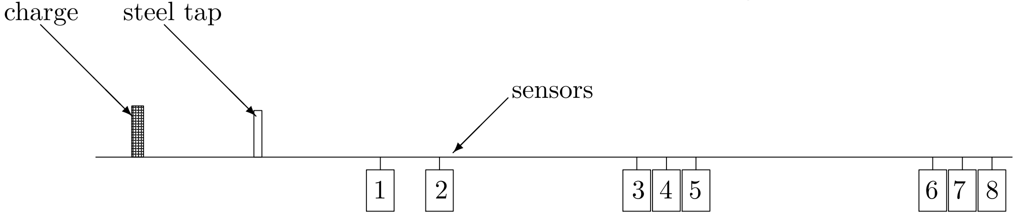

Figure 4.14: Side-on pressure rig schematic

Table 4.3: Sensor distances at Raufoss

Sensor #	R $[m]$
1	0.6000
2	0.7500
3	0.1250
4	0.1325
5	0.1400
6	0.2000
7	0.2075
8	0.2150

4.2.1.2 Experiment Procedure

The side-on pressure sensors were placed at various distances shown in table 4.3. The side-on pressure was recorded for all three charge types, however only the "Naked" charge will be discussed in this thesis. 4 different naked charge tests were performed. See section 5.2.1 for results

4.2.2 Blast Loading Steel Plates

A series of blast loaded plate experiments were conducted at 4 different standoffs.

4.2.2.1 Experiment Rig

The rig used for blast loading plate experiments consists of two identical plate-rigs which makes it possible to test two different standoffs for each explosive charge (see figure 4.15a).

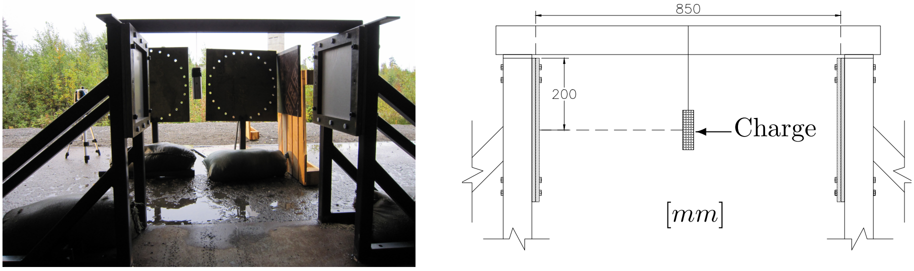

(a) Blast loading steel plates rig

(b) Rig at Raufoss schematic

A schematic of the experimental setup is shown in figure 4.15b which shows how the charge is placed directly in front of the plate.

2mm thick, quadratic 400x400mm Docol 600 DL steel plates are employed, which are bolted to the frames. The plate geometry and boundary conditions can be seen in figure 4.15.

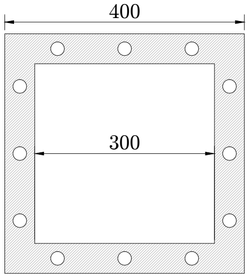

Figure 4.15: Plate boundary conditions (Raufoss 2010)

4.2.2.2 Experiment Procedure

Two explosive experiments were performed, thus permanent plate deflections from four different standoffs could be extracted.

Table 4.4: Experiment details for Raufoss

Experiment #	R $[mm]$	Explosives
1	300 550	C4 140-146 g
2	400 450	

See section 5.2.2 for results.

Chapter 5

Experimental Results

5.1 Experiments at NTNU

In this section the results from the experiments described in section 4.1.3 and 4.1.4 will be presented. The results are presented alongside each other because they are both performed using the gas gun at NTNU.

5.1.1 Reflected Pressure Time-History

The experiment data is extracted using the methods described in section 4.1.3.1. The data from the pressure sensors suffered from a lot of noise, thus making it necessary to apply a filter in order to properly process the data. A 100 Hz 2. order lowpass Butterworth filter algorithm was employed to filter the raw data (See Appendix A.2 for details). A collection of comparisons between raw data and the corresponding filtered pressure time-histories can be found in Appendix A.1. Filter validation was performed by comparing the impulses of both raw data and filtered results, thus making sure impulses are preserved in the filtering process. An example of the filtered results is shown in figure 5.1.

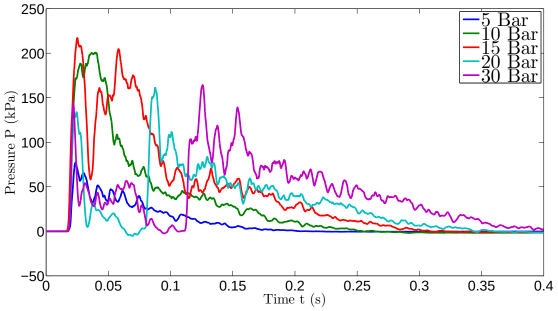

Figure 5.1: Reflected pressure time-history from the midpoint sensor (sensor 1, NTNU 2013)

Data from sensor 1 is compared for the two aforementioned experiments in figure

5.2 and table 5.1.

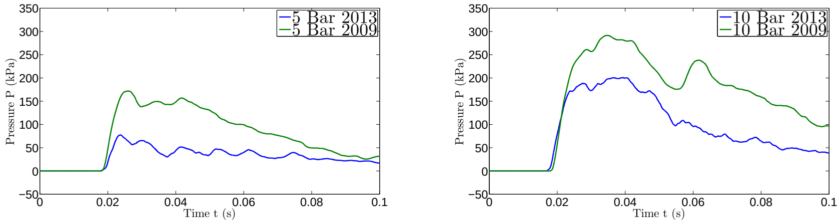

(a) 5 Bar **(b)** 10 Bar

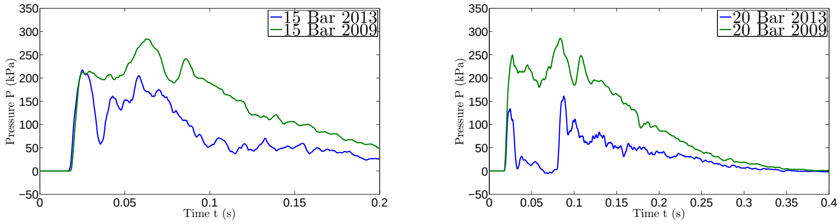

(c) 15 Bar **(d)** 20 Bar

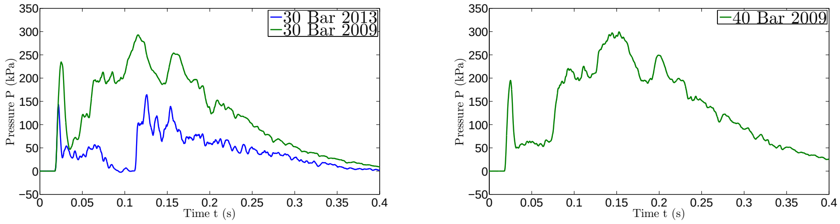

(e) 30 Bar **(f)** 40 Bar

Figure 5.2: Reflected pressure time-history NTNU comparison

Table 5.1: Peak reflected pressure and impulse comparison NTNU

Sensor	2009 (40 Bar)		2009 (30 Bar)		2013 (30 Bar)	
	$i_{r,exp}$ $[kPas]$	$P_{r,exp}$ $[kPa]$	$i_{r,exp}$ $[kPas]$	$P_{r,exp}$ $[kPa]$	$i_{r,exp}$ $[kPas]$	$P_{r,exp}$ $[kPa]$
1	54.30	299.49	47.51	292.82	15.72	164.29
7	31.90	246.31	33.51	269.98	10.81	144.46
8	14.83	253.60	13.69	235.97	3.53	67.35
9	5.42	180.36	2.09	166.72	-4.74	23.88
11	30.03	266.31	1.36	24.78	-15.58	5.87

As mentioned in section 4.1.4 the intention behind retrofitting the barrel with a funnel was to increase the peak pressure and impulse. However based on the data in both table 5.1 and figure 5.2, it is evident that the funnel has reduced the total impulse for all the various pressure levels in the main tank.

For the upcoming numerical simulations, it is important to check whether or not the pressure load is evenly distributed around the plates centre. Initially the data from 2009 was examined and found to be approximately centred. However, by investigating the results the loads from 2013 are found to be not centred. A good representation of the pressure distribution was found by looking at the data from sensors 2, 3, 7 and 8 (illustrated in figure 5.3a). Ideally if the pressure is evenly distributed around the centre, sensor 2 and 3 should give similar results as sensor 7 and 8. Pressure data indicates signs of the load distribution being consistently non-centred for all the different pressure levels in the main tank. An example of pressure time-history being non-centred is shown in figure 5.3b and table 5.2.

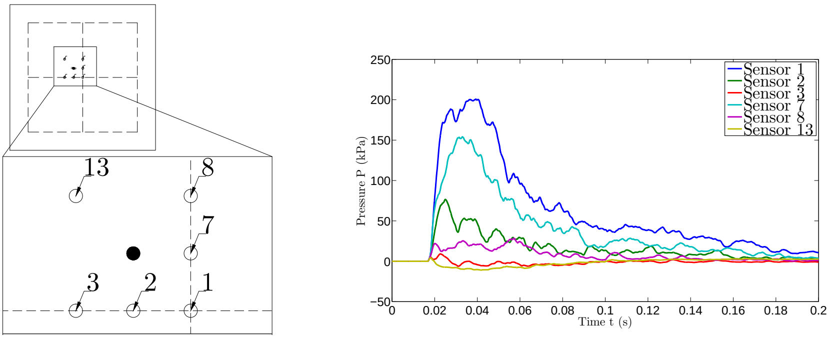

(a) Sensor selection (front) **(b)** Example of pressure time-history (10 Bar)

Figure 5.3: Pressure results

Table 5.2: Peak pressures recorded using 10 Bar

Sensor #	$P_{r,exp}$ $[kPa]$
1	200.8
2	76.6
3	9.2
7	154.2
8	28.4
13	4.4

From examining the results, it is evident that the funnel somehow forces the pressure loading out of alignment.

5.1.2 Loaded Steel Plate Deformations

After a series of initial tests it was shown that any tests using pressures beneath 30 Bar in the main tank only resulted in elastic deformation, and are therefore omitted. Note that the different plate boundary conditions should be considered when comparing the plate deflections from 2009 and 2013.

Table 5.3: Plate deformations summary

Experiment	Δ_{exp} $[mm]$	
	NTNU (2009)	NTNU (2013)
30 bar test # 1		8 ± 2
40 bar test # 1	~ 15	18 ± 2
40 bar test # 2		20 ± 2

Accurate measurements of midpoint deflection proved to be difficult, due to asymmetrical deformations in all the plates subjected to loading. The asymmetrically deformed plates are shown in figure 5.4

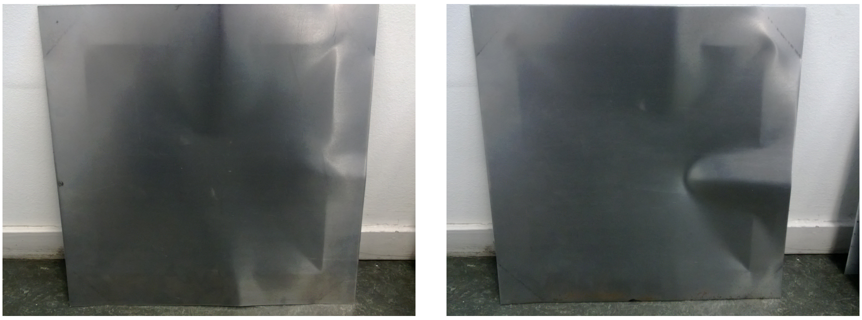

(a) 30 Bar test 1

(b) 40 Bar test 1

(c) 40 Bar test 2

Figure 5.4: Deformed plates (2013) due to air-pressure loading

The deformed plates show signs of the load not being centred, reaffirming the suspicions from the reflected pressure measurement-results in section 5.1.1. The plate-deflections are larger than what was reported back in 2009, despite being loaded by a smaller impulse and peak pressures. However, there are significant changes concerning plate boundary conditions (shown in figure 4.9) which would indicate that the boundary conditions used now (2013) allows for more deformation.

Comments concerning the reflected pressure- and plate loading experiment at NTNU are listed below.

- The plate might not be centred perfectly in front of the muzzle.
- The newly added funnel might be unsymmetrical and forces the pressure wave out of alignment.
- The plate might not be perfectly placed perpendicular to the direction of the pressure flow.
- The pressure readings from the transducers might be inaccurate.
- The plate deflections might be inaccurately measured.

5.2 Experiments at Raufoss (2010)

5.2.1 Side-on Pressure Time-History

Pressure time-history was recorded for all sensors, and the data was largely consistent. The resulting peak side-on pressures from the experiments are summarized in table 5.4.

Table 5.4: Side-on pressure readings

Sensor #	$P_{so,exp}$ $[kPa]$			
	Test # 1	Test # 2	Test # 3	Test # 4
1	1742.53	1576.93	3223.43	1296.25
2	1047.09	1376.42	1010.00	1001.51
3	362.31	362.31	362.31	362.31
4	277.62	285.84	294.20	338.86
5	127.58	137.63	344.70	213.95
6	89.38	100.15	92.96	138.25
7	84.27	96.72	73.78	110.98
8	18.67	48.17	16.99	25.30

Examples of the pressure time-history plots are shown in figure 5.5.

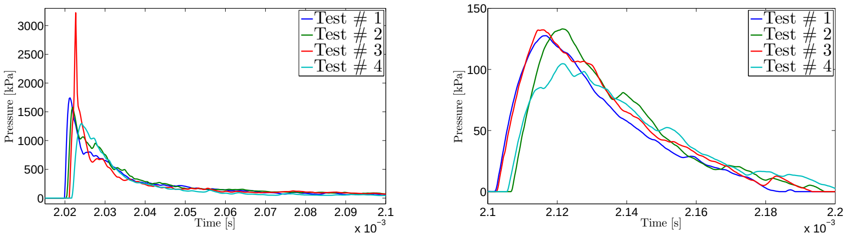

(a) Sensor 1 **(b)** Sensor 5

Figure 5.5: Side on pressures Raufoss (2010)

Based on the relatively large value in sensor 1 in Test # 3, it might indicate that this is an anomaly. Seemingly sensor 3 could be malfunctioning considering it was recording the same peak pressures for all 4 tests, or sensor 3 is somehow capped at a certain peak pressure.

5.2.2 Blast Loaded Steel Plate Deformations

Experimental results from the blast loaded plates described in section 4.2.1.2 are shown in table 5.5.

Table 5.5: Experiment results for Raufoss

Experiment #	R $[mm]$	Δ_{exp} $[mm]$
1	300	32.19
	550	18.47
2	400	26.93
	450	24.07

An example of a deformed plate is shown in figure 5.6.

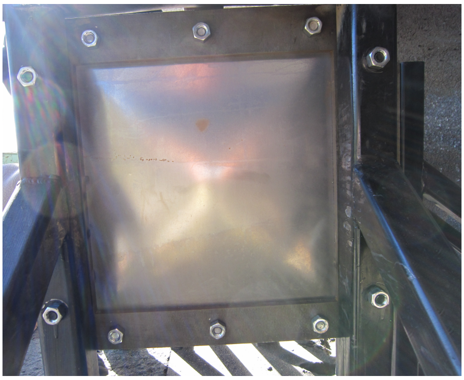

Figure 5.6: Plate deformation example from experiments at Raufoss

The plate deformation seems to be symmetric judging by figure 5.6.

Comments and potential error-sources regarding the experiments at Raufoss:

- The side-on pressure transducers might be inaccurate
- The small steel tap in the side-on experiments might disturb the experimental results
- The measured distances might be inaccurate
- The mass of the explosive agent, or the geometry could deviate from the reported values
- The plate might have geometric imperfections

Chapter 6

Preliminary Numerical Study

The foundation for the upcoming numerical models will be established in this chapter by accounting for the necessary calibrations required in order to recreate experimental results.

6.1 The Lagrangian Model

The Lagrangian formulation described in 2.4.3 will be employed in order to represent the different plate- and supporting frame-geometries presented in chapter 4. An initial study on mesh sensitivity will be performed in LS-DYNA, followed by a cross-platform validation for the two numerical codes LS-DYNA and IMPETUS. After the cross-platform validation, a calibration of the number of particles employed in the discrete particle method will be performed.

6.1.1 Mesh-Sensitivity Study

A mesh-sensitivity study will be performed in LS-DYNA to determine which elements and corresponding attributes, that are appropriate to accurately represent the expected deformation.

Introduction

A simple benchmark problem was defined and modelled in LS-DYNA. A quarter symmetry model based on the geometry shown in figure 4.11 was created, and loaded by a generalized blast wave. The applied load in the defined benchmark problem is represented by a Friedlander approximation employing a set of parameters expected to be a good representation of the loads observed in the experiments. The parameters are shown in table 6.1 and illustrated in figure 6.2. The applied load area is described in figure 6.1c.

Even though no experimental data is present to validate theses numerical simulations, the results are expected to converge towards one solution as the mesh is refined.

The numerical model consists of three parts; a frame, clamp and a plate (shown in figure 6.1). The frame and the clamp consists of rigid solid elements, and are restricted from any movements or rotations. The 0.7 mm thick plate will be modelled both by shell and solid elements. A general contact algorithm will be employed between all parts with a steel-steel friction coefficient set to zero. The plate material model is based on data from section 3.3. Note that in LS-DYNA the rigid elements must be assigned a density, which in turn has been set to the same density used for the plates. However considering the frame and the clamp are restricted from any movement or rotations, the assigned density will not have an impact on the analyses.

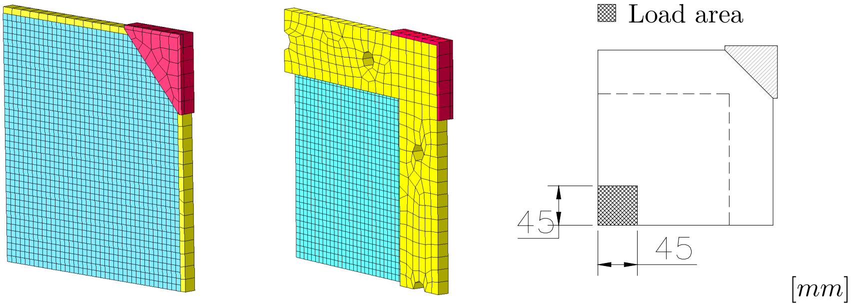

(a) Front **(b)** Back **(c)** Load area schematic

Figure 6.1: Numerical model overview (frame: yellow, clamp: red, plate: blue)

Table 6.1: Friedlander parameters

Parameter	Value
b	2
T$^+$	0.02
P_{so}	300 kPa

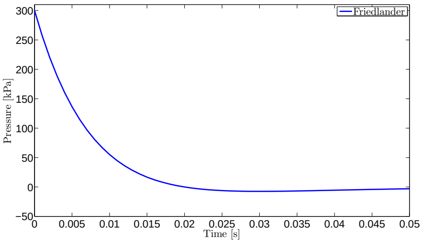

Figure 6.2: Friedlander load curve

Procedure

The different shell and solid element formulations with corresponding element sizes investigated are tabulated in table 6.2. The plate response is expected to be dominated by bending, such that an appropriate number of thickness integration points needs to be determined for shells. The number of solid elements through the plates thickness is investigated for the same reason.

Table 6.2: Mesh sensitivity study element sizes overview

Shell elements		
Element size $[mm^2]$	# of integration points through plate thickness	Total # of elements
5x5	3,5 and 7	1521
2.5x2.5	3,5 and 7	6084
1x1	3,5 and 7	37636
Solid elements		
Element size $[mm^3]$	# of elements through plate thickness	Total # of elements
5x5x0.7	1	1521
	2	3042
	3	4563
2.5x2.5x0.7	1	6084
	2	12168
	3	18252
1x1x0.7	1	37636
	2	75272
	3	112908

A very small solid element size needs to be employed in order to prevent bad aspect ratios, which would be very computationally expensive. However, they are included to illustrate the benefits of employing shell elements for this particular type of problem.

The analyses will be run for a simulation time of 50 ms, and the deflection of the center node will be recorded. The simulated time of 50 ms allows the plates to be permanently deformed, and also have enough time to determine a permanent deflection based on the average of the oscillating plates elastic deformations.

The solid element formulation employed in LS-DYNA is especially intended for elements with poor aspect ratio using full integration, and the shell elements are employing a standard Belytschko-Tsay formulation [33] employing reduced integration. The Gauss-Lobatto integration rule was used in the thickness integration, in order to have integration points at the shell element surfaces.

The analyses were performed using LS-DYNA synchronized multiprocessing (SMP) solver version ls971d R6.1.0 with double precision (I8R8). Primarily a Xeon64 system Linux cluster was employed allocating 3 processors on each analysis. See appendix B.1 for a keyword example.

Results

The results from the analyses are shown in table 6.3, and are further illustrated in figure 6.3. An example of a deformed plate is shown in figure 6.4

Table 6.3: Results from the mesh sensitivity study

SOLIDS

Element size [mm]	# of elements through thickness	Δ_{max} [mm]	Δ_{perm} [mm]	CPU time [h:min:s]*
5	1	11.43	5.23	[01:14:03]
	2	15.94	10.50	[04:25:54]
	3	21.66	17.36	[08:39:34]
2.5	1	12.79	6.58	[03:01:03]
	2	25.42	20.02	[16:01:58]
	3****	-	-	[–:–:–]
1	1	43.15	18.89	[24:13:40]
	2****	-	-	[–:–:–]
	3****	-	-	[–:–:–]

SHELLS

Element size [mm]	# of thickness integration points	Δ_{max} [mm]	Δ_{perm} [mm]	CPU time [h:min:s]*
5	3	26.47	15.26	[00:01:42]**
	5	25.53	13.41	[00:02:11]**
	7	25.46	13.61	[00:02:38]**
2.5	3	25.94	13.52	[00:12:32]**
	5	25.36	13.31	[00:15:44]**
	7	25.03	12.65	[00:18:42]**
1***	3	27.59	15.10	[04:24:54]
	5	26.76	14.45	[05:07:32]
	7	26.54	13.99	[05:51:30]

* Since the CPU resources available are not constant, reported CPU times should not be used as accurate measurements.

** Analyses were run using 4 processors on an intel core i7-3612QM CPU personal laptop.

*** For smaller elements an increase in displacement occurs (especially for 1x1x0.7 [mm] solids). By controlling the energy readouts it is confirmed that increased sliding energy is the culprit for the increase in midpoint displacement.

**** Analyses not completed because the expected CPU time was too long.

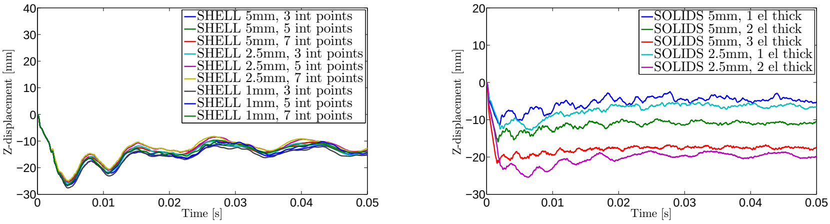

(a) Shell elements **(b)** Solid elements

Figure 6.3: The plates midpoint deflection

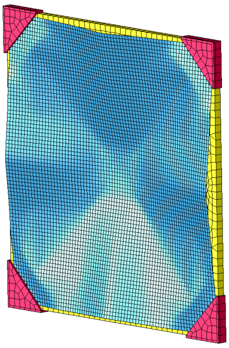

Figure 6.4: Example of a deformed plate at T = 0.05s employing 5x5 $[mm]$ shell elements with 5 integration points through the thickness

As expected employing less than three solid elements through the plate thickness represents bending poorly. The 5x5x0.23 $[mm]$ solid elements requires a CPU time of over eight hours compared to approximately two minutes using shells. This makes shell elements the appropriate choice for further study.

Based on the results in this section, a shell element formulation with reduced integration employing 5x5 $[mm]$ elements, and 5 thickness integration points, is chosen based on its proven accuracy compared to the smaller element sizes, and its efficiency.

For shell elements employing reduced integration it is important to check for hourglassing. See figure 6.5a for the energy balance for the selected shell element formulation.

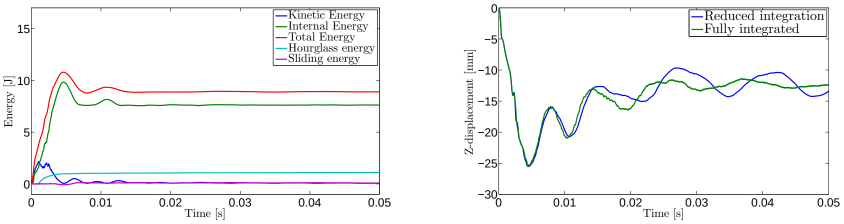

(a) Energy reduced

(b) Reduced vs full integration

Figure 6.5: Reduced integration versus full integration

Hourglass energy is observed in figure 6.5a. The hourglass energy is suspected to be caused by small high frequency plate-oscillations that does not affect the maximum and permanent displacement to any noticeable degree. Additional simulations using similar elements employing full integration were performed, and by comparing the results (shown in figure 6.5b), it is observed that the maximum and permanent deflections are not significantly affected by hourglassing.

6.1.2 Cross-Platform Validation

In order to compare numerical results between IMPETUS and LS-DYNA we have to ensure that the two yields approximately the same results for identical problems. In this section the two codes are compared using two defined problems.

Introduction

Two scenarios that represents the different experiments performed in this thesis are subject to a cross-platform validation. The first scenario is based on the numerical simulations described in section 6.1.1, and the geometry is based on the experiments in section 4.1.4. The second scenario is based on the geometry from the experiments in section 4.1.3.

Procedure

An overview of the scenario 1 geometry is shown in 6.6, followed by a description of the applied load in figure 6.7

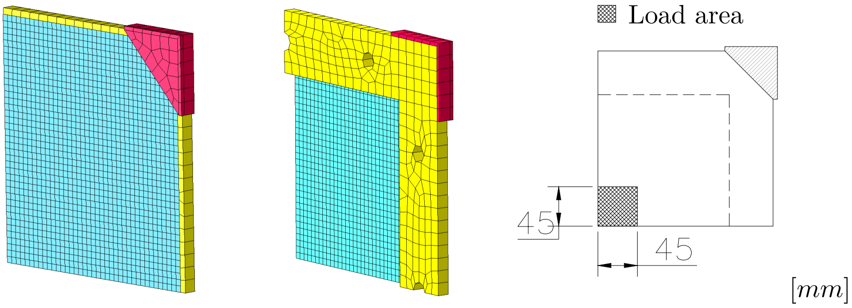

(a) Front **(b)** Back **(c)** Load area schematic

Figure 6.6: Scenario 1 overview (frame: yellow, clamp: red, plate: blue)

For scenario 1, three nodal deflection time-history plots will be subject for comparison as shown in figure 6.7a.

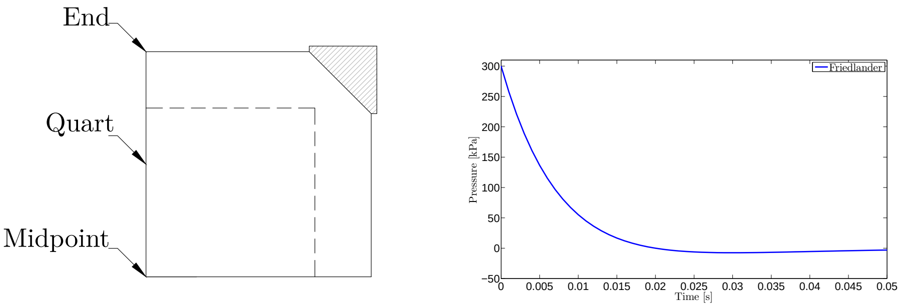

(a) Recorded node-deflections **(b)** Friedlander load curve

Figure 6.7: Scenario 1 further explained

As mentioned in the previous section, a Friedlander curve is chosen for the applied load in scenario 1 because it is a good representation of the loads observed in the experiments.

An overview of the scenario 2 geometry is shown in figure 6.8, followed by a description of the applied load in figure 6.9b.

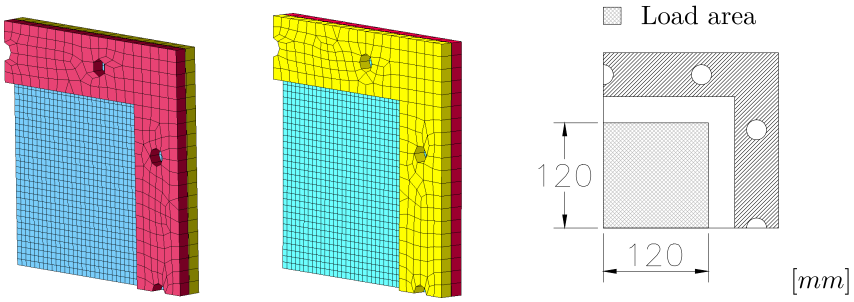

(a) Front **(b)** Back **(c)** Load area schematic

Figure 6.8: Scenario 2 overview (frame: yellow, clamp: red, plate: blue)

For scenario 2, two nodal deflection time-history plots will be subject for comparison as shown in figure 6.9a.

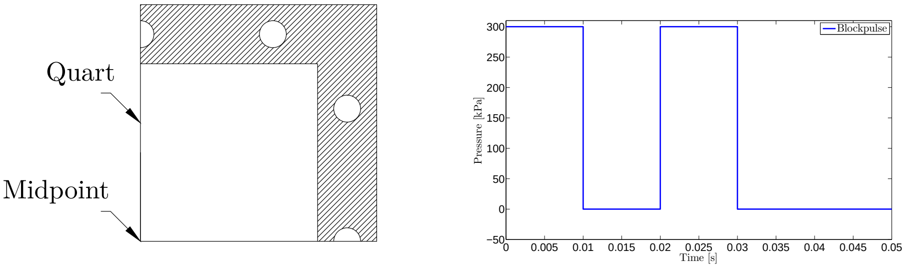

(a) Recorded node-deflections **(b)** Blockpulse load curve

Figure 6.9: Scenario 2 further explained

The applied load in scenario 2 is a blockpulse (illustrated in figure 6.9b) with peak pressures of 300 kPa at 10ms intervals, evenly distributed on a area sketched in figure 6.8c. A blockpulse is employed in order to represent sudden loading-offloading observed in the experiments.

The geometry created in LS-DYNA is exported and imported into IMPETUS. However IMPETUS does not employ the same set of shape functions as LS-DYNA, thus it allows for higher order solid elements to be employed without the increased numerical noise present in classic explicit codes with non-linear elements. The third order elements in IMPETUS (figure 6.10) have shown excellent performance in plasticity problems [41] but results in increased computational costs compared to classic first order linear elements. Different element sizes were therefore chosen in the two codes such that the results would be as comparable as possible. The recommended 5x5 $[mm]$ shell element from section 6.1.1 is employed in LS-DYNA, therefore an element size of 15x15x0.7 $[mm]$ was chosen in IMPETUS. This was based on the assumption that three linear shell elements in LS-DYNA are approximately the equivalent of employing a single third-order element in IMPETUS. A comparison of the different element formulations is shown in figure 6.11.

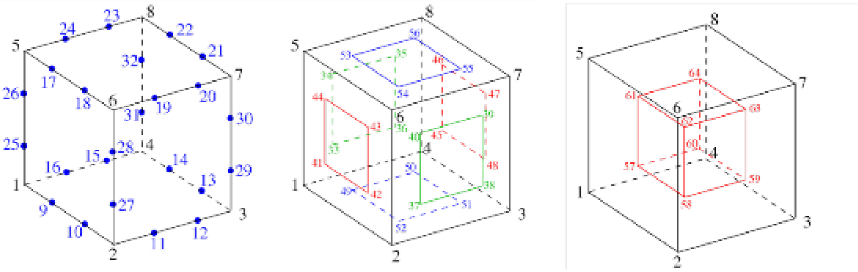

Figure 6.10: IMPETUS elements [43]

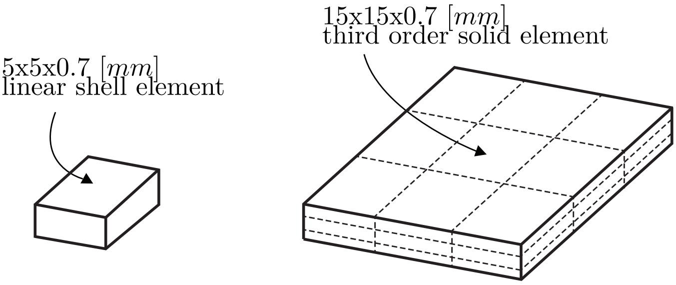

Figure 6.11: Cross-platform element comparison

Only a graphically comparison between the deflection time-histories from each code will be performed in order to validate the cross-platform plate deformation.

Results

The recorded nodal deflections for Scenario 1 are shown in figure 6.12, and shown for Scenario 2 in figure 6.13.

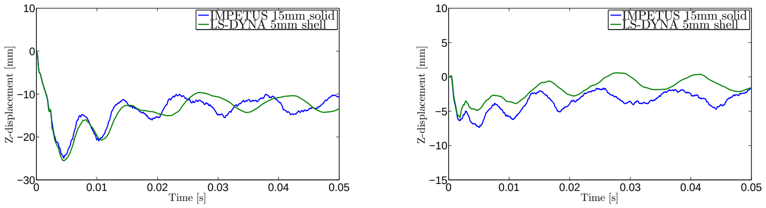

(a) Midpoint **(b)** Quart

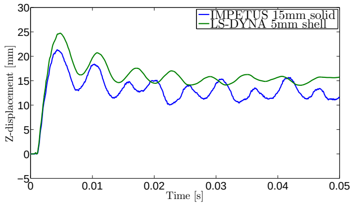

(c) End

Figure 6.12: Scenario 1 nodal deflection time-history comparison

By examining the deflection time-history curves from scenario 1, it is evident that IMPETUS and LS-DYNA generate approximately similar results. The maximum midpoint deflections are almost identical, and the only apparent difference is that the oscillations are not in sync. This could be explained by the fact that the two element formulations results in different plate stiffness's.

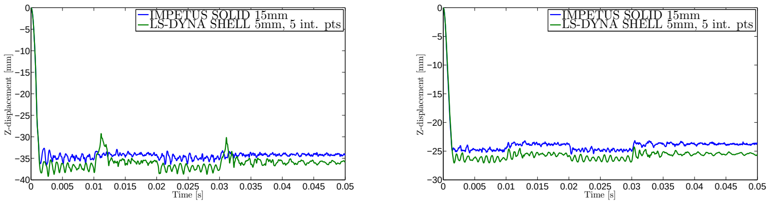

(a) Midpoint **(b)** Quart

Figure 6.13: Scenario 2 nodal deflection time-history comparison

In the deflection time-histories from scenario 2 it is also observed strong similarities between LS-DYNA and IMPETUS. However the deflection in IMPETUS is observed to be slightly bigger than what is produced in LS-DYNA, which also could be explained by the difference in stiffness generated by the two different element formulations. A comparison of the computational time in IMPETUS against the time in LS-DYNA is shown in table 6.4.

Table 6.4: Computational time compared

Scenario	LS-DYNA [h:min:s]	IMPETUS [h:min:s]
1	[00:02:11]	[04:02:22]
2	[00:02:30]	[06:50:47]

Based on the results in this section it is observed that the two codes can generate similar results despite using different element formulations. A cross-platform comparison is valid given that it is based on the conditions presented in this section (identical input geometry except for IMPETUS employing 15x15x0.7 [mm] solid elements for the plate, compared to the 5x5 [mm] shell elements employed in LS-DYNA).

6.1.3 Number of Particles

In chapter 7 the discrete particle method will be employed to describe various blast loads. As outlined in section 2.4.7.2 it is impossible to simulate every single molecule present in the experiment because of the computational demand. Therefore a proper amount of particles needs to be chosen to sufficiently retain accuracy but not increase the computational time to an unacceptable level.

Introduction

As seen in section 6.1.2, the third order solid elements greatly increase the computational time of the analyses in IMPETUS. Therefore a quarter symmetry model should be employed wherever applicable. Due to the apparent randomness of the particle motion, the effect of employing a symmetry condition with varying amount of particles will be investigated further. Analysis will be run to determine a sufficient number of particles that is needed to present the same displacements for both a full and a quarter symmetry model. An increased amount of particles are needed to accurately represent the blast load when the standoff distance increases, thus a balance between an acceptable computational time and accurate results must be achieved. For a low amount of particles, one would expect the results to be inaccurate and jagged because of the evident discrete particle collisions. For an increased amount of particles the results will more resemble a continuum fluid which is the main idea.

Procedure

The largest standoff distance from the experiments in section 4.2.2 is chosen for these simulations, seeing that a sufficient amount of particles for this standoff will suffice for the shorter standoff distances.

To ensure a properly defined quarter symmetry model, the amount of particles was adjusted such that both the full and quarter symmetry model presented the same amount of particles per unit volume of explosives, in this way the particle radius are identical in both the quarter symmetric and full model. The same third order solid element as used in the cross platform validation was employed in all simulations (see figure 6.10), with an element size of 15x15x2 [mm]. The different cases investigated are presented in table 6.5 and pictures of the numerical models are shown in figure 6.14.

Cases investigated:

Table 6.5: Number of particles per model

N_p	Standoff, R	Mass C-4
Full/Quart	$[mm]$	$[g]$
10^4 / 0.25×10^4	550	145
10^5 / 0.25×10^5		
10^6 / 0.25×10^6		
10^7 / 0.25×10^7		

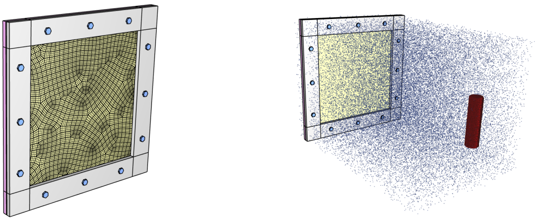

(a) Full **(b)** Full (N_P=10^5)

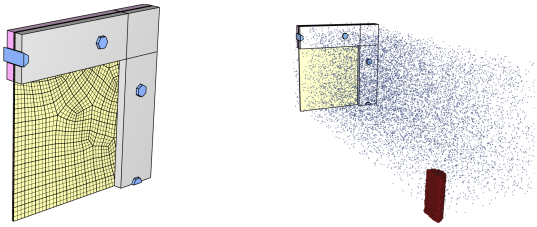

(c) Quart **(d)** Quart (N_P=0.25×10^5)

Figure 6.14: Models used in IMPETUS

Number of particles exceeding 10^7 is simply too computationally expensive to be performed in this thesis. The analyses are run for 10ms, and the displacements for the mid- and quarter points (shown in figure 6.13) are recorded.

Results

The results from the analyses are compared alongside experimental data in table 6.6, and time-displacement plots for the mid- and quarter-points are depicted in figure 6.15.

Table 6.6: Number of particles study results

Geom.	N_p	Δ_{max} $[mm]$	Δ_{perm} $[mm]$	CPU-time [h:min:s]*	Rel. i_r err. $[mms]$**	$\frac{\Delta_{perm}}{\Delta_{exp}} \cdot 100\%$
Full	10^4	20.25	15.50	[04:31:05]	1.1038e-2	83.92 %
Quart	$\frac{1}{4} \times 10^4$	19.21	15.00	[01:29:32]		81.21 %
Full	10^5	18.32	12.75	[04:56:59]	1.1179e-2	69.03 %
Quart	$\frac{1}{4} \times 10^5$	18.24	12.95	[01:36:11]		70.11 %
Full	10^6	22.05	17.50	[10:31:48]	1.7300e-3	94.75 %
Quart	$\frac{1}{4} \times 10^6$	21.93	17.50	[02:58:54]		94.75 %
Full	10^7	24.12	20.0	[82:21:18]	1.2954e-3	108.28 %
Quart	$\frac{1}{4} \times 10^7$	24.06	19.9	[21:25:09]		107.74 %

*Note that the CPU times are somewhat affected by the workload on the CPU cluster, thus it is only the general trend of increased computational time that are outlined.

**The relative error is computed as the integral:

$$e_{mid} = \int_0^{t_{end}} |z_{mid,full}(t) - z_{mid,quart}(t)| \, dt \tag{6.1}$$

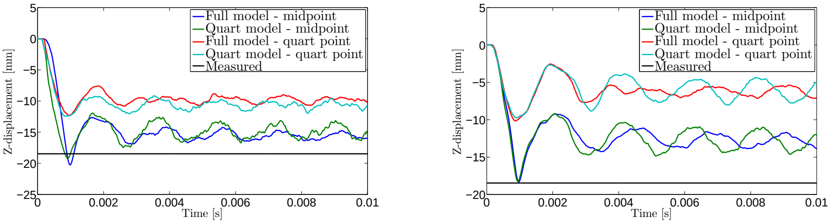

(a) $N_p = 10^4$ **(b)** $N_p = 10^5$

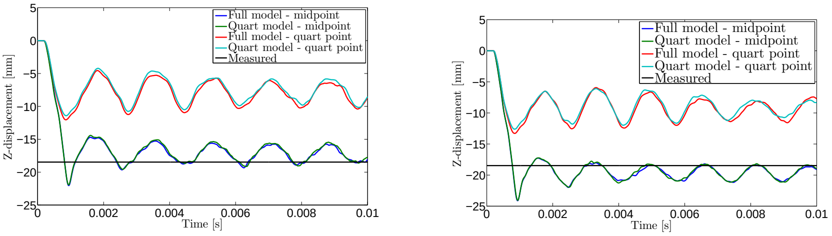

(c) $N_p = 10^6$ **(d)** $N_p = 10^7$

Figure 6.15: Time-displacement plots for various N_p

A time-lapse of one of the numerical simulation can be seen in figure 6.16. For visualization purposes, the particles are not rendered.

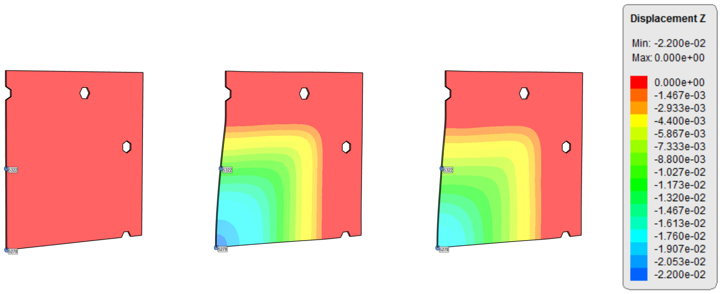

(a) T = 0s **(b)** T = 1e-3s **(c)** T = 1e-2s

Figure 6.16: Time-lapse of the simulation employing $\frac{1}{4} \times 10^6$ number of particles $[m]$

As we observe from the results, for a low amount of particles the quarter symmetric model deviates markedly from the full model. We observe that the quarter symmetry model underestimates both the peak and permanent deflection. This is in all likeliness caused by two factors:

- The perfect symmetric deformation in the quarter model will result in a stiffer behaviour.
- Fewer particles will hit dead center because of the reflective boundaries along the symmetry axes on the global particle domain.

As the amount of particles increases, the results from the two models converges, and for the last two cases the results are almost identical. For a low amount of particles, the computational time between the two representations are at a three to one ratio. We observe that when the amount of particles increases, the difference between the two models in terms of computational time increase exponentially.

A $N_p = 0.25 \times 10^6$ for the quarter symmetric model is chosen for all future discrete particle analyses on the basis of computational time and accuracy.

6.2 The Multi-Material Eulerian Model

In order to perform numerical simulations of the explosive process described in section 4.2. Two materials such as the explosive agent and the surrounding air needs to be numerically represented.

It was initially intended to employ a purely Multi-Material Eulerian (MME) using the single point Eulerian formulation in LS-DYNA. However, in order to accurately represent the explosive process, the pure MME required an extremely small element size (in the order 0.1x0.1 [mm]), thus severely increasing the computational demand. Because of this, it was decided to apply a MMALE-formulation where the Eulerian mesh grid is fixed. Note that remeshing occurs on the front between different materials within the fixed mesh grid. This would retain the accuracy of a fine mesh when representing the close-ranged blast wave propagation while reducing the computational expense. The remeshing of the shock front will lead to advection errors, but the benefits of employing the MMALE formulation outweighs the alternative of employing a finely meshed single point Eulerian formulation. Even though in principle the fluids are modelled as a MMALE, it will for future reference be referred to as a Multi-Material Eulerian because of the fixed Eulerian mesh grid.

In this chapter a study will be performed in order to determine the appropriate numerical parameters best suited for the upcoming MME simulations with regards to accuracy and efficiency.

6.2.1 Introduction

The side-on experiments at Raufoss (2010) presented in section 5.2.1 will be used as a benchmark for the MME simulations because of its repeatability and simple set-up. The necessary equation of state and material data for the explosive agent and surrounding air are based on the parameters presented in sections 3.4 and 3.5.

The numerical parameters employed consistently in all the MME simulations are based on recommendations from the supplied [33], [34], [24], [25], and also [3] and [40]. Additional consulting was performed via an unofficial LS-DYNA user forum [46], where especially Dr. Len Schwer from SE & CS offered a great deal of assistance. All the numerically related parameter-choices has been summarized and commented on in appendix B.2, however the key parameters will be presented in this section. The second order Van Leer advection scheme presented in section 2.4.6.3 is employed, and it is set to advect node- and element associated variables at every Lagrangian timestep. The pressure iteration algorithm implemented in LS-DYNA mentioned in section 2.4.6.5 is also employed in order to properly describe how the different material deforms within the same element. An initial timestep of 10^{-8}s with a timestep scaling factor of 0.6 was found to produce the most stable simulations, and will be applied consistently for all the upcoming MME analyses.

The following sections will cover the initial selection of MMALE element formulations in LS-DYNA, followed by a study on the correlation between domain size and numerical instabilities. This will ultimately lead to a selection of an appropriate domain size, which would then be subject for a mesh sensitivity study. An expected convergence of the solutions corresponding to the mesh refinement would make it possible to recommend an element size for further study based on its efficiency and accuracy. Lastly the possibility of a 2D to 3D mapping technique is explored.

6.2.2 Investigating Two MMALE Element Formulations in LS-DYNA

A full 3D simulation of the explosive process is expected to become computationally expensive, such that a study on a more computationally affordable 2D element formulation is performed. The 2D analyses require rotational symmetry around at least one axis. This section will be dedicated to investigating the difference between the 2D and 3D element formulations.

Introduction

The following element formulations are subject for further investigation:

- SECTION_SOLID (3D)
    - El. 11: 1 point ALE multi-material element [33]
- SECTION_ALE2D (2D)
    - El. 14: Axisymmetric solid (x-y plane, y-axis of rotational symmetry) – area weighted [33]

The 2D element formulation has the obvious advantage of requiring less elements than the 3D formulation while employing the same domain-length. However the 2D formulation can only be applied if a rotational axisymmetric condition can be respected (meaning that a scenario can be properly represented employing symmetry around at least one axis). The comparison between the two element formulations will be performed by numerically simulating the aforementioned side-on pressure experiment at Raufoss (2010) from section 4.2.1, which would uncover whether or not the two element formulations generate similar results.

Procedure

A 3D and 2D model were created, with the respective domain sizes shown in figure 6.17.

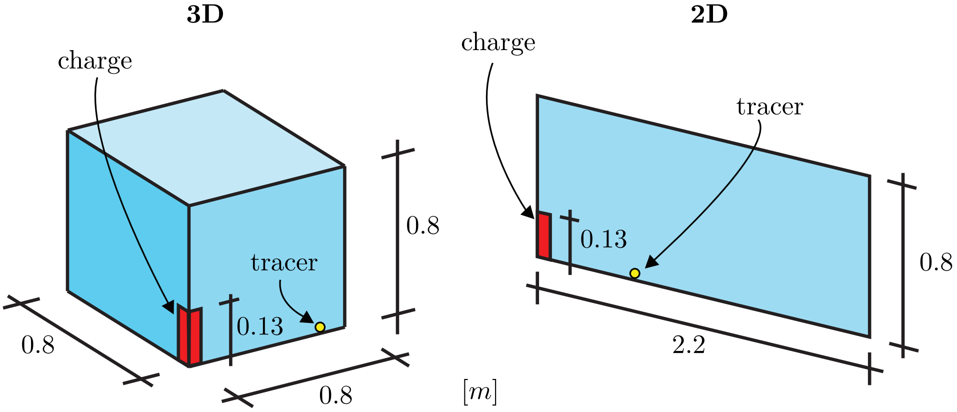

Figure 6.17: Domain sizes explained

The 3D domain-length was made shorter than the 2D model in order to minimize the number of elements. Only $\frac{1}{8}$ of the total geometry in the experiment is modelled for the 3D simulation, using reflective boundaries in the xy-plane, xz - plane and yz - plane such that symmetry is utilized to reduce the computational expense. The remaining surfaces are applied with a boundary pressure of 1 bar, allowing air to escape the domain. Tracers in the numerical models were positioned at the standoff $R = 0.6$ m (shown in figure 6.17), where the recorded pressure time-history data will be the benchmark in which the two element formulations are compared by. The charge geometry in the 3D model was employed with the ”Initial volume fraction geometry” implementation in LS-DYNA, filling the existing ”air-elements” with the C4 material and the corresponding EOS. Information about the elements employed in both of the models are shown in table 6.7

Table 6.7: Numerical models overview

Model	Element size $[mm]$	Total # of elements
3D	10x10x10	512 000
2D	10x10	17600

Results

The resulting peak side-on pressures and impulses from the analyses are shown in table 6.8, and the side-on pressure time-history plots are shown in figure 6.18.

Table 6.8: Section comparison results

Sensor	Section	P_{so} $[kPa]$	i_{so} $[Pas]$	CPU-time [h:min:s]
1	3D	1517	121	[01:11:28]
	2D	1673	130	[00:01:46]

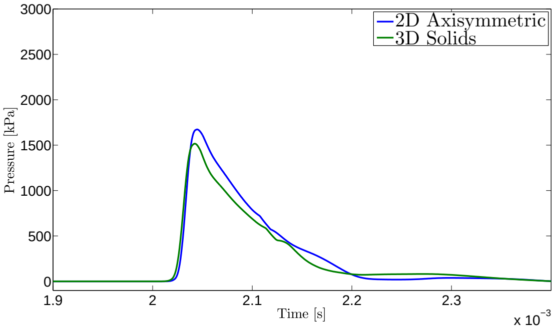

Figure 6.18: Section comparison 2D vs 3D

Based on comparison in table 6.8 and figure 6.18 a relatively good correlation between the two element formulations is observed. The small observed differences could be explained by how the charge geometry is represented in the two formulations. The 2D model described the charge as perfectly round, whereas the charge in the 3D model have to be discretized. The 2D-analyses is observed to be far more efficient when comparing the recorded CPU time in table 6.8, thus making the 2D element formulation the recommended choice where a symmetry condition can be justified.

The analyses had difficulties employing multiple symmetric multiprocessing (SMP) processors, therefore the analyses were performed with only 1 SMP processor allocated.

Some numerical instabilities are observed in the energy readouts from the 3D model (shown in figure 6.19) which manifests in the form of a non-physical sudden increase of pressure. This is probably caused by the applied pressures on the global domain boundaries. This results in an increase of the kinetic and total energy in the system. However, by examining the graphical output it is observed that the instabilities originates near the top corner directly above the charge, such that it does not influence the recorded pressures on the ground.

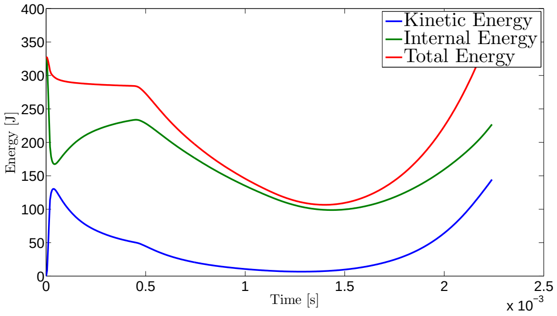

Figure 6.19: Energy balance for the 3D analysis

Note that the observed energy drop (at approx. t=0.5 ms) is caused by the blast wave front escaping the domain, thus reducing the total energy in the system.

The numerical instability is also present in the 2D model, however to a lesser degree, indicating it could be related to the domain size, which will be the subject for further investigation in the next section.

6.2.3 MME Domain Sensitivity Study

In this section a study employing different MME domain sizes is performed in order to further illustrate the correlation between domain size and numerical instability. Based on the results, the domain size that displays a negligible amount of numerical instability and still retains its numerically efficiency will be chosen for further study.

Introduction

In order to minimize the number of required analyses, a peak side-on pressure and impulse comparison identical to the one presented in section 6.2.2 will be employed, thus placing tracers at a standoff $R = 0.6$ m.

Procedure

The domain sizes subject for further investigation are shown in figure 6.20.

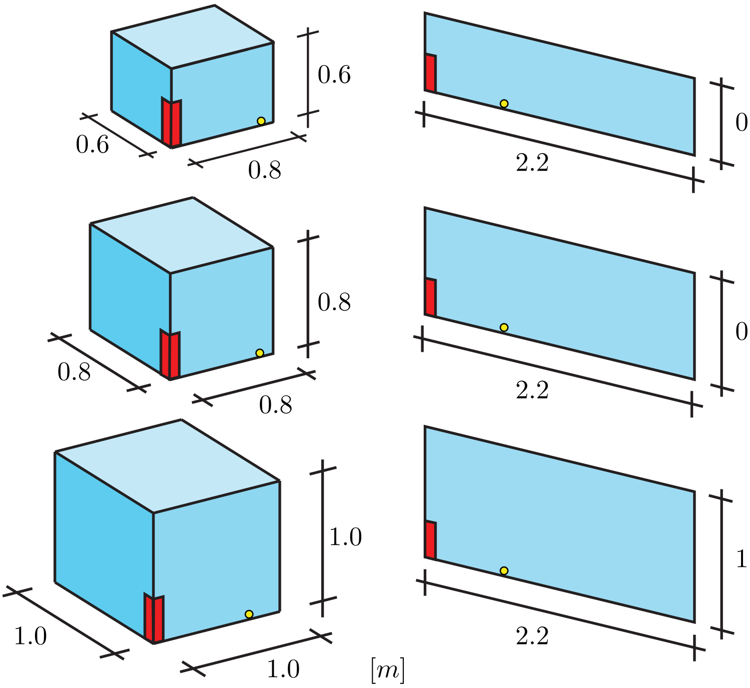

Figure 6.20: Domain sizes investigated

The domain size of the first 3D analysis is set to a length of 0.8 m such that the tracer is placed within the Eulerian domain. The same numerical parameters and elements employed in section 6.2.2 were applied in this section.

Results

The resulting peak side-on pressures and impulses from the analyses are compared in table 6.9, whereas the side-on pressure time-histories are compared in figure 6.21.

Table 6.9: The results from the study on domain size

Section	Domain Height $[m]$	# of elements	P_{so} $[kPa]$	i_{so} $[Pas]$	CPU time [h:min:s]
3D	0.6	288000	1178	79	[02:04:20]*
	0.8	512000	1517	121	[01:11:28]
	1.0	1000000	1571	125	[01:33:141
2D	0.6	13200	1673	130	[00:01:21]
	0.8	17600	1673	130	[00:01:46]
	1.0	22000	1673	130	[00:02:05]

* This domain size was very susceptible to numerical instabilities, thus increasing the CPU-time by a factor of ~2 compared to a 3D domain size of 0.8x0.8x0.8 $[m]$.

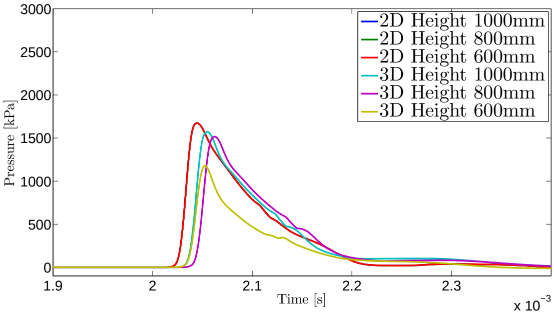

Figure 6.21: A side-on pressure time-history comparison ($R = 0.6$ m)

The 3D element formulations seem to be very sensitive to the domain size based on the shapes of the side-on pressure time-histories in figure 6.21, however this is not so clear just by comparing the data in table 6.9.

By examining the maximum side-on pressure time-history for the 2D element formulations, there does not seem to be an apparent difference between the domain sizes. However by looking at the energy output data it is observed a slight increase of energy for the smaller domain sizes.

By examining the energy readouts from the 3D and 2D analyses it seems like numerical instability is directly related to the distance the blast wave is allowed to travel before it escapes the domain. Four additional simulations were performed with the 2D element formulation to further illustrate the correlation between domain size and numerical instabilities. The additional analyses are performed with decreasingly smaller domain heights, while still retaining a domain-length of 2.2 m. The energy balance plots are shown in figure 6.22,

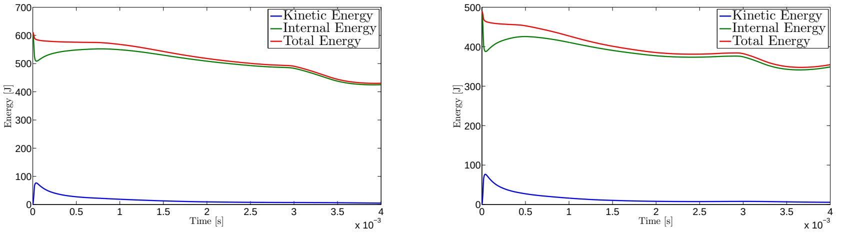

(a) Domain height = 0.8 m **(b)** Domain height = 0.6 m

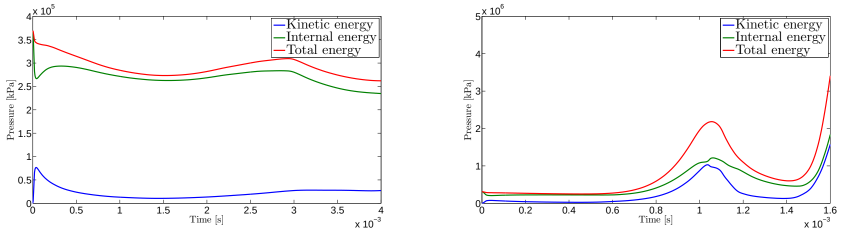

(c) Domain height = 0.4 m **(d)** Domain height = 0.3 m

Figure 6.22: The energy balance for various domain sizes employing the 2D element formulations

Based on the results in table 6.9 and figures 6.21 and 6.22 it is evident that there is a correlation between domain size and numerical instabilities. The 3D element formulations seems to be more susceptible to numerical instabilities, which could be explained by the reduced domain-length in which the blast wave is allowed to travel.

A minimum MME domain size of 0.8 m is chosen for further study, because as observed the numerically created non-physical pressure have no impact on the main positive phase of the side-on pressure at $R = 0.6$ m. Since the upcoming numerical simulations in chapter 7 will employ a maximum standoff at $R = 0.55$ m, the results from this section will have justified employing a minimum domain size of 0.8x0.8 m^2 and 0.8x0.8x0.8 m^3 for both the 2D and 3D element formulations respectively.

6.2.4 Mesh-Sensitivity Study

In this section a study on the impact of element size in the MME analyses will be performed in order to find the optimal choice of element size considering efficiency and accuracy.

Introduction

A 2D formulation is preferred because the simulations can be performed very efficiently while retaining accuracy. By employing the recommended minimum domain size from the previous section 6.2.3, a series of simulations using different element sizes will be performed in order to see if the solution converges as the mesh is refined. Note that this is the element size in the rigid Eulerian mesh and would as a result affect the maximum allowed characteristic lengths of the elements at the remeshed shock front. The element size that produces accurate results, and still is computationally inexpensive will be chosen for further study as a result of this study.

Procedure

A set of analyses will be performed employing 4 different element sizes shown in table 6.10. Tracers are positioned at $R = 0.6$ m and $R = 1.4$ m.

Table 6.10: Numerical models overview

Element size $[mm]$	Total # of elements
10x10	17520
5x5	70400
2.5x2.5	281600
1x1	1744230

Results

The resulting peak side-on pressures and impulses from the analyses are compared in table 6.11, whereas the side-on pressure time-histories are shown in figure 6.23

Table 6.11: Eulerian mesh sensitivity comparison

R $[mm]$	Element size $[mm]$	P_{so} $[kPa]$	i_{so} $[Pas]$	CPU-time [h:min:s]
0.6	10x10	1393	129	[00:01:00]
	5x5	2235	161	[00:10:50]
	2.5x2.5	2490	166	[02:58:32]
	1x1	2721	154	[73:39:56]
1.4	10x10	164	45	[00:01:00]
	5x5	222	53	[00:10:50]
	2.5x2.5	243	55	[02:58:32]
	1x1	252	56	[73:39:56]

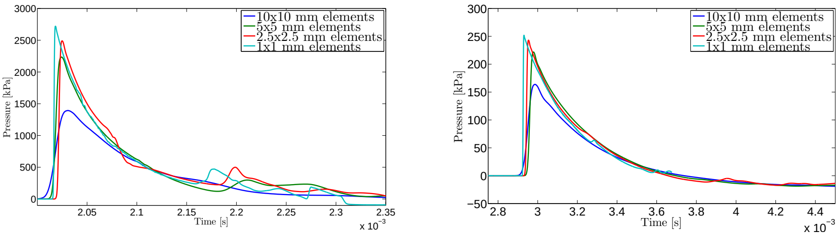

(a) $R = 0.6$ m **(b)** $R = 1.4$ m

Figure 6.23: Eulerian mesh sensitivity side-on pressure time-histories compared for $R = 0.6$ m and $R = 1.4$ m

By examining the results in table 6.11 and observing the side-on pressure time-history in figure 6.23, it is evident that mesh refinement convergence around the results from employing 5x5 $[mm]$ elements and smaller. The 10x10 $[mm]$ elements underestimates both the impulse and peak side-on pressure. The differences between the various element sizes seems to diminish by the distance from the charge, which could be explained by that the initial blast wave propagation near the explosive is more sensitive to the element size.

By comparing the computational time and accuracy shown in table 6.11, element sizes of 5x5 and 5x5x5 [*mm*] are recommended for further study in the upcoming MME analyses in order to sufficiently represent the close range blast propagation.

For the situations where axisymmetry conditions cannot be fulfilled, the 3D element formulation must be employed. Applying 5x5x5 [*mm*] elements in the recommended domain size in 3D would require a total of 4 096 000 elements. This would drastically increase the total computational time, and the amount of storage required to complete the analyses. Because of this, an alternative approach needs to be considered such as the 2D to 3D mapping technique implemented in LS-DYNA, which was successfully employed in [55]. This technique will be further investigated in the next section 6.2.5.

6.2.5 Mapping a MME Analysis from 2D to 3D

In order to minimize the computational expense of simulating three dimensional blast wave propagations, a study on the 2D to 3D mapping technique implemented in LS-DYNA will be performed.

Introduction

In order to be able to represent the close range blast wave propagation accurately without employing the recommended 5x5x5 [*mm*] element size from section 6.2.4, it is necessary to find an alternative solution. It is possible to allow the blast wave to propagate in a refined 2D mesh before being mapped into a 3D domain. The remap into the 3D domain can be applied as soon as the rotational axisymmetry condition no longer can be justified. A step by step explanation on the 2D to 3D mapping technique is presented in [3].

Procedure

Because the blast wave in the two dimensional domain only will be allowed to propagate for a short amount of time, it is decided that a smaller domain can be utilized without experiencing the numerical instabilities discussed in section 6.2.3. A 0.5x0x5 m^2 2D domain size was created employing 1x1 [*mm*] elements (shown in figure 6.24a). A 1x1 [mm] element size was found to represent the initial blast propagation in the best possible way, without being too computationally expensive. The results from the last cycle of the 2D analysis is mapped over in to a cubic 3D 0.8x0.8x0.8 m^3 domain with an element size of 10x10x10 [mm]. The selected 10x10x10 [mm] element size in the 3D domain is employed because the blast wave is less sensitive to element size the further away it is from the charge. Note that the 2D analysis is modelled with rotational axisymmetry around the y-axis, and the result is mapped around the z-axis in the 3D domain (shown in figure 6.24).

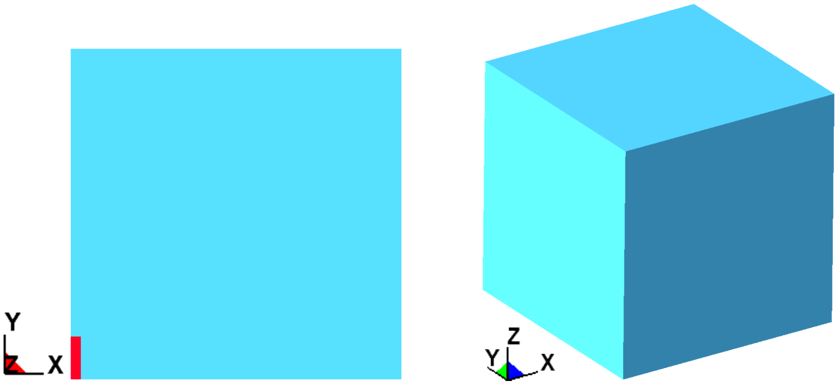

(a) 2D domain **(b)** 3D domain

Figure 6.24: Mapping description

Tracers are positioned at R = 0.6 m, such that the side-on pressure can be compared against the already performed simulations using only 2D element formulations from section 6.2.4, and the 3D element formulation employing the 10x10x10 [mm] elements from section 6.2.3.

Results

The resulting peak side-on pressures from the analysis are compared against a selection of 2D and 3D analyses from sections 6.2.4 and 6.2.3. The results are shown in table 6.12 and figure 6.25.

Table 6.12: Mapping from 2D to 3D results

Description	Element size $[mm]$	P_{so} $[kPa]$	i_{so} $[Pas]$	CPU time [h:min:s]
2D axisymmetric	5x5	2235	160	[00:14:26]
3D solids	10x10x10	1517	121	[01:11:28]
2D Mapped to 3D	1x1,10x10x10	2028	163	[01:16:58]*

* CPU-time is the total time of the 2D and 3D analyses.

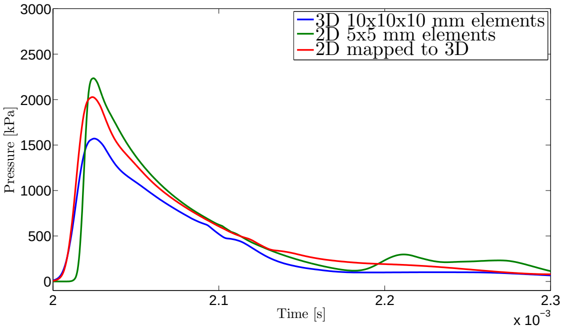

Figure 6.25: The 2D to 3D mapping results compared to 2D only and 3D only

Based on the results in table 6.12 and examining the side-on pressure time-history in figure 6.25, it seems like the 2D to 3D mapping technique successfully manages to retain most of the fine-mesh precision when representing the close-range blast wave propagation, and still be computationally efficient. Thus making the 2D to 3D mapping technique the preferred choice in future analyses were an axisymmetry-condition can not be utilized for the whole domain.

Note that there exists other techniques meant to decrease the computational expense for MME analyses. For example element erosion and mesh biasing, both of which have been employed with success in [55]. However these alternatives were not further explored in this thesis.

Chapter 7

Numerical Methods

7.1 Introduction

Originally this thesis was supposed to focus on blast calculations and numerical simulations of the gas gun at NTNU. This however posed as a problem because the gas gun struggled with emulating an ideal blast wave and had a very complex geometry that disturbed the air flow around the test specimen. It can be concluded from figure 5.1 that the positive duration of the blast is around one hundred times longer than that of an explosion in free air with the same magnitude. This posed us with a problem both regarding the increased simulation time, and a proper description of the blast load variables.

It was in the end decided to use the gas gun experiments as a preliminary method to validate our numerical techniques, and then apply the techniques and knowledge we gained from this study to properly validate the experiments performed at Raufoss (2010) presented in section 4.2.

7.2 Experiments at NTNU

In this section the experiments performed at NTNU (described in section 4.1) will be subject for numerical simulations.

7.2.1 Lagrangian

A Lagrangian formulation is employed first because it is the easiest simulation to define.

7.2.1.1 Simulations Employing a Discretized Pressure Distribution in LS-DYNA

Introduction

In this section a series of Lagrangian analyses will be performed using the pressure-time history from the experiments at NTNU (see figure 7.1) as load curves applied directly on the plates in each sensors tributary area.

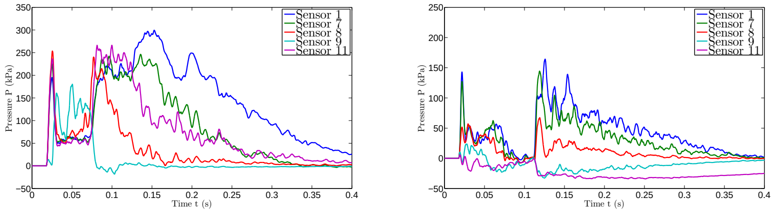

(a) 40 Bar (2009) experiment data **(b)** 30 Bar (2013) experiment data

Figure 7.1: Load curves

Procedure

In order to simplify the simulations and enable the possibility of a quarter symmetry model, the pressure distribution is assumed to be centred. This allows choosing pressure readings from sensors 1, 7, 8, 9 and 11 as representable as a discretized circular pressure distribution on a quarter-symmetry model as seen in figure 7.3b. This assumption is employed despite the results from section 5.1.1 showing a non-centred pressure distribution in the 2013 experiments.

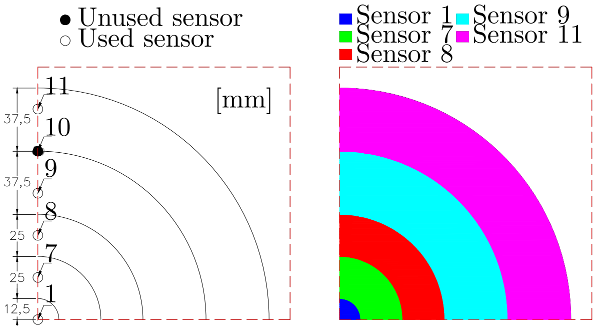

(a) Sensors used for load curve data **(b)** Sensors tributary area

Figure 7.2: Pressure distribution for 2009 and 2013 simulations

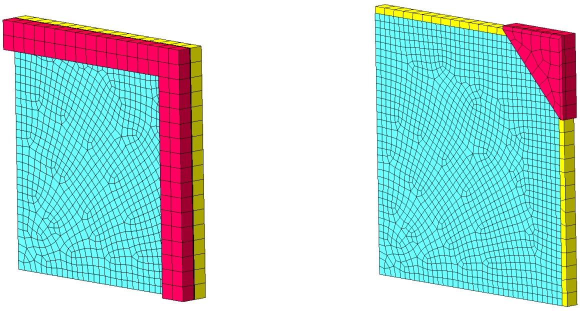

(a) 2009 (front) **(b)** 2013 (front)

Figure 7.3: Numerical models overview

The boundary conditions for the 2009 model are based on figure 4.9, and the boundary conditions employed in the 2013 model are based on figure 4.11. The parameters employed for the numerical models are identical to the ones used in section 6.1.1, which means that the plates are assumed to be placed in between the frame and clamps with enough slack, such that they are not pinched. Also the mesh elements have been allocated in a circular pattern after the geometry in figure 7.2b such that the discretized pressure distribution from the sensors are not overlapping on any elements.

Results

The results from the Lagrangian analyses are presented in table 7.1, followed by a midpoint deflection time-history plot for the 2009 analysis in figure 7.4.

Table 7.1: Lagrangian NTNU results

Experiment [mm]	Δ_{max} $[mm]$	Δ_{perm} $[mm]$	Δ_{exp} $[mm]$	CPU time [h:min:s]*	$\frac{\Delta_{perm}}{\Delta_{exp}} \times 100\%$
40 Bar (2009)	18.7	14.3	15	[00:21:47]	95.33 %
30 Bar (2013)*	-	-	8	[00:05:03]	-

*The numerical simulation was aborted because the plate got sucked out of the supports.

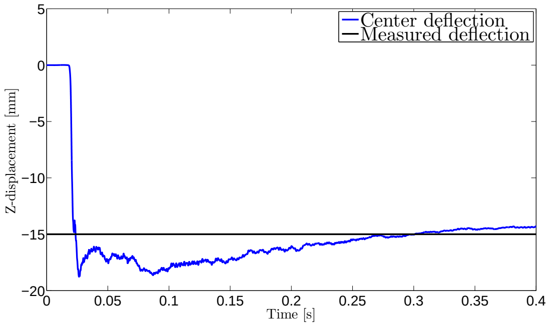

Figure 7.4: Midpoint node deflection time-history from the 2009 analysis

By examining results in table 7.1 and figure 7.4 it is observed that the 2009 load curves (shown in figure 7.1a) combined with the established Lagrangian model (shown in figure 7.3a) results in a good representation of the reported permanent deflection from the experiment. A time-lapse from the 2009 analysis is shown in figure 7.6

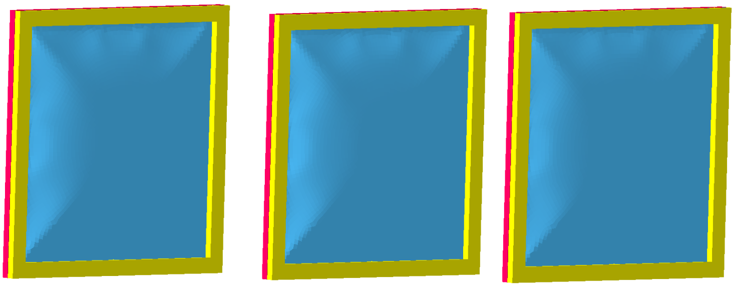

(a) T=0.0448s **(b)** T=0.0768s **(c)** T=0.4s

Figure 7.5: A time-lapse from the 2009 Lagrangian analysis

A time-lapse from the 2013 analysis is shown in figure 7.5 displaying the plate being sucked out of the supports.

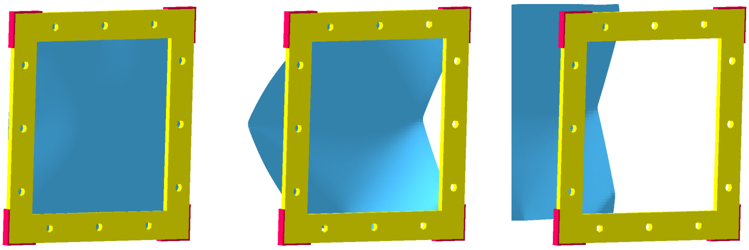

(a) T=0.0448s **(b)** T=0.0768s **(c)** T=0.0992s

Figure 7.6: A time-lapse from the 2013 Lagrangian analysis

By employing the load history from 2013 it is observed in figure 7.6 that the plate first experience some elastic deformation, and then is sucked out of the supports in the opposite direction.

As to why employing the recorded pressure from 2013 poorly represents the experimental loads could be explained by that the pressure-sensors are malfunctioning or are not properly calibrated. Also the close proximity between the funnel and plate, allows for little room for the air to evacuate through, such that it could create a suction in the pressure transducers. This will be subject for further investigation in the MME analyses in section 7.2.2.

Another source of error is the discretization of the pressure distribution, which will be the subject for further investigated in the next section.

7.2.1.2 Simulations Employing a Continuous Pressure Distribution in IMPETUS

Introduction

To capitalize on the strengths of the different numerical codes, a different approach was selected when it came to simulate the plate deformation with a Lagrangian description in IMPETUS.

As seen in the previous section the load curves can be directly applied to zones with individual tributary areas. The boundaries between these zones can (and will) represent discrete sudden load changes with respect to space that might affect the permanent plate displacement in a non-realistic manner. To investigate if these sudden changes affect response in a noticeable way we created a load field that interpolated the load curves from the different sensors in a continuous manner.

Procedure

In LS-DYNA one would normally apply loads directly to a set of element faces. The faces in each set are selected discretely by the analyst, such that applying a different load to each element face would be highly time consuming. This would also complicate the mesh refinement process because load definitions would have to change if the mesh is altered. However in IMPETUS, the loads are applied to faces inside existing user-defined geometry. Because the load applied on the faces inside the user-defined geometry can be described as functions of space and time, one can in practice apply a different load to each element face in the whole domain with minimal effort. IMPETUS was therefore employed to eliminate the large discrete load variations across elements at the tributary area intersection described earlier.

To create the continuous load field, functions for the various parameters in the load equation have to be established. A MATLAB script was written to curve-fit a Friedlander equation (eq. (2.1)) to the load curves for each sensor in figure 7.2a. Peak pressure P_r and the impulse i_r^+ were kept constant while the positive duration T^+ and the decay coefficient b were varied to create the best fit. A typical example of the Friedlander curve fit can be seen in figure 7.7

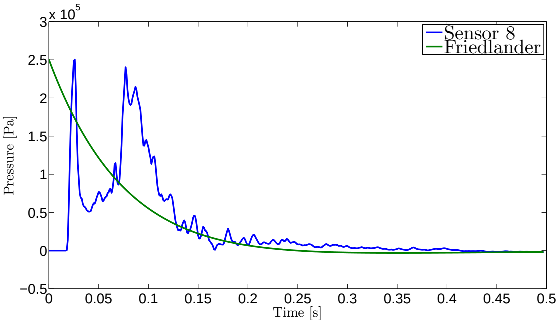

Figure 7.7: Example of the Friedlander curve fit

The resulting parameters in the Friedlander equation can then be interpolated with respect to space in a radial direction outwards from the center of the plate.

The resulting pressure load field is a spatial description of the load that is an approximation of the original test data. The resulting Friedlander equation (eq. (7.1)) is dependent on the spatial position of the element and time.

$$P(t,x,y) = P_r(x,y)\left(1 - \frac{t}{T^+(x,y)}\right) e^{\frac{-b(x,y)t}{T^+(x,y)}} \tag{7.1}$$

$$P_r(x,y) = P_r(r) \tag{7.2}$$

$$b(x,y) = b(r) \tag{7.3}$$

$$T^+(x,y) = T^+(r) \tag{7.4}$$

$$r = \sqrt{x^2 + y^2} \tag{7.5}$$

By employing equation (2.1), every element in the FE mesh will have their own Friedlander equation that is interpolated from continuous variables, thus eliminating the errors associated with the large discrete changes in load across the tributary area boundary. An illustration of the Friedlander load field technique can be seen in figure 7.8.

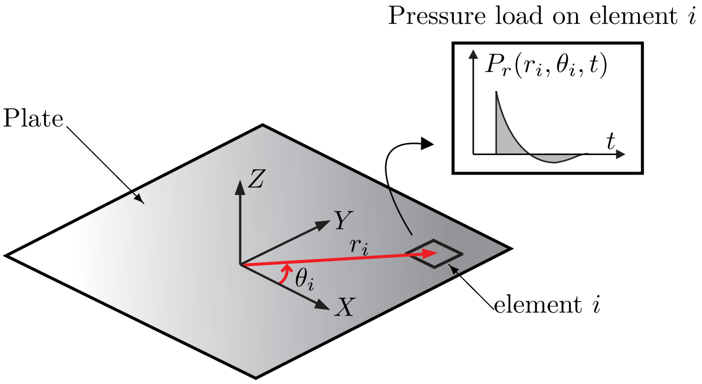

Figure 7.8: 2D Lagrange explained

To capture the non-radial symmetric effects such as the one observed in section 5.1.1, equation (7.1) can be augmented to include the angle θ (see figure 7.8). By multiplying equation (2.1) with 7.6 the effect of pressure changes with varying θ is captured:

$$f(r,\theta) = \cos^2(\theta)\left(1 - \frac{P_{90}(r)}{P_0(r)}\right) + \frac{P_{90}(r)}{P_0(r)} \tag{7.6}$$

$$\theta = \arctan(\frac{y}{x}) \tag{7.7}$$

where

$P_0(r)$	is the pressure at $\theta = 0°$(e.g sensor 2, 3, 4 or 6. See figure 4.7b)
$P_{90}(r)$	is the pressure at $\theta = 90°$ (e.g sensor 7, 8, 9 or 11. See figure 4.7b)

Note that equation (7.7) is only valid for a quarter symmetric model placed in the positive x and y quadrant.

This method is created to prevent the approximations made by a tributary area approach; however it contains several approximations and assumptions by its own. The approach assumes that the peak pressure and positive duration is a continuous variable with respect to space. It also approximates these variables with a polynomial that have to be of a finite small polynomial order to simplify the numerical implementation. The polynomial with an order between one and ten that have the lowest error norm will suffice. As seen in figure 7.16 the resulting functions are not far from its parent. This method also assumes that the time of arrival t_a of the blast wave is constant across the whole plate. In reality there are some small discrepancies, but this will only be apparent for very large plates or for extremely small values of the scaled distance Z.

Experiments from 2009

In order to validate the experimental data, a numerical simulation of the experiments described in section 7.2.1.2 using a Friedlander load field was attempted.

The load field was created from experimental data in section 5.1.1 and it was applied to a quarter symmetry model with appropriate boundary conditions seen in figure 7.9. The experimental data did not exhibit any non-symmetric radial effects such that augmenting the load field with equation (7.6) was not necessary. Examples of the Friedlander fitted functions for two of the sensors can be seen in figure 7.10.

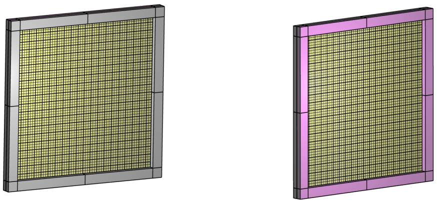

(a) Front **(b)** Back

Figure 7.9: Numerical model (2009)

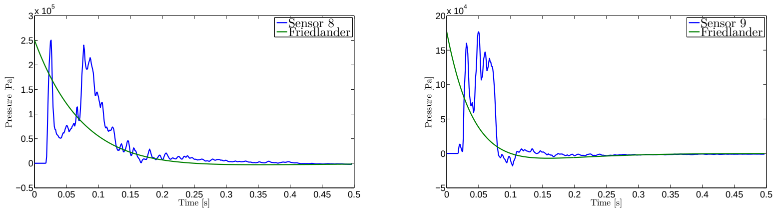

(a) Sensor 8

(b) Sensor 9

Figure 7.10: Examples of the Friedlander fitted functions

Two examples of the Friedlander variable functions that are interpolated in the radial direction can be seen in figure 7.11.

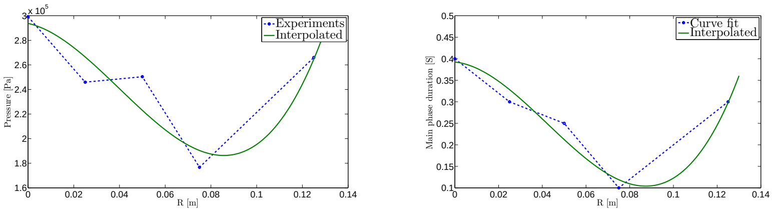

(a) Peak pressure $P_r(r)$

(b) Positive Duration $T^+(r)$

Figure 7.11: Examples of interpolated Friedlander variable functions

The simulation time was set to 400ms, and the midpoint deflection-history was recorded.

Results

The displacement-time curve of the midpoint of the steel plate can be seen in figure 7.12, and the results are summarized in table 7.2.

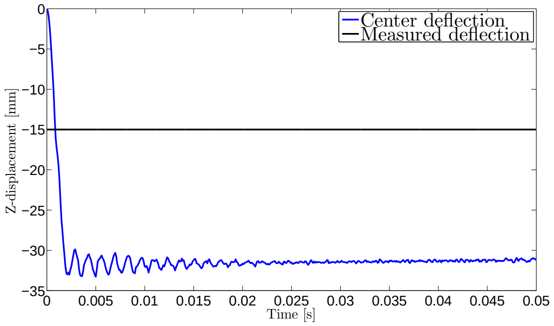

Figure 7.12: 2D Lagrange Displacement vs time

Table 7.2: Friedlander load field 2009 NTNU

Experiment [mm]	Δ_{max} [mm]	Δ_{perm} [mm]	Δ_{exp} [mm]	CPU time [h:min:s]*	$\frac{\Delta_{perm}}{\Delta_{exp}} \cdot 100\%$
40 Bar (Figure ..)	33.27	31.35	15.00	23:06:08	209 %

*Note that the CPU times are somewhat affected by the workload on the CPU cluster, thus only the general trends of computational time are outlined.

A time-lapse of the deformation is depicted in figure 7.13.

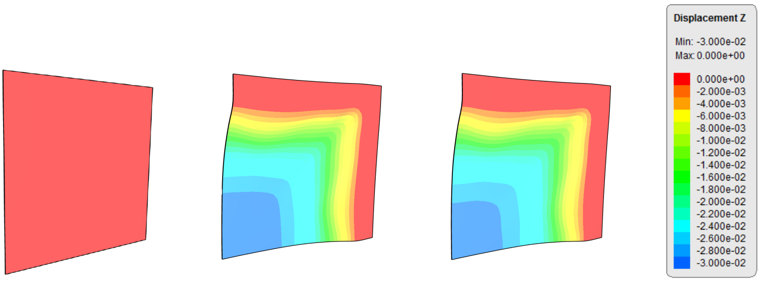

(a) T = 0s **(b)** T = 4e-3s **(c)** T = 4e-1s

Figure 7.13: Time-lapse of the simulation $[m]$

As we see observe from the results, the Friedlander field approach overestimates the permanent deflection of the midpoint. This is most likely a result of multiple combining factors:

- The experimental data does not closely resemble Friedlander equation.
- The blast wave hits all elements at the plate at the exact same time
- The idealized geometry in the numerical model

The overestimation was anticipated, but the displacements are expected to agree more for experiments with explosives that produce a more ideally shaped blast wave.

Experiments from 2013

A quarter symmetric numerical model was established and is shown in figure 7.14. The pressure readings from the experiments are as stated in section 5.1.1 quite non-ideal, such that the curve-fitted Friedlander equations will be a crude approximation of their parent functions. To improve the simulation, equation (7.1) was augmented with (7.6) to capture the non-radial symmetry effects of the pressure sensors. The same 15x15x0.7 [*mm*] third order solid element described in section 6.1.2 was employed.

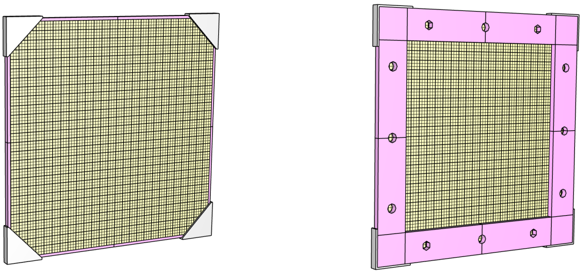

(a) Front **(b)** Back

Figure 7.14: Reflected model used for further numerical simulations

The curve-fitted Friedlander equations for two of the sensors can be seen in figure 7.15

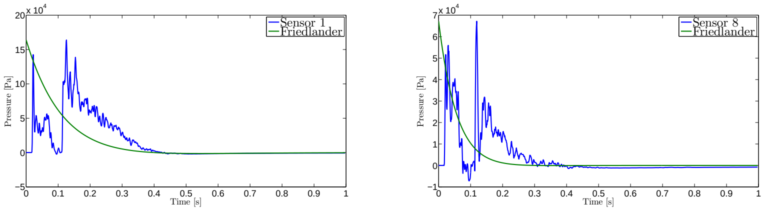

(a) Sensor 1 **(b)** Sensor 8

Figure 7.15: Friedlander fitted functions examples

Examples of the interpolated variable functions are seen in figure 7.16.

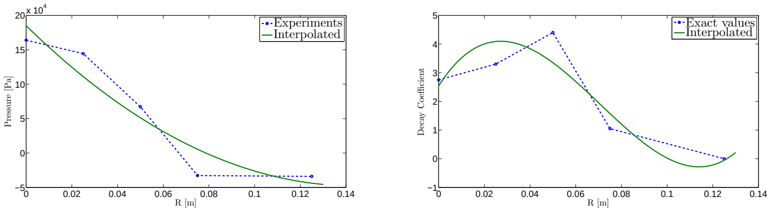

(a) Peak Pressure $P_r(r)$ **(b)** Decay coefficients $b(r)$

Figure 7.16: Examples of interpolated variable functions

The simulation time was set to 400ms, and the midpoint deflection-history was recorded.

Results

As seen from the results in section 7.2.1.1, numerical results from these experiments are of limited value. When a Friedlander load field is created, the same result is observed where the steel plate flies in the opposite direction of what is expected. A time-lapse of the deformation can be seen in figure 7.17 and the results are summarized in table 7.3.

Table 7.3: Friedlander load field displacement

Experiment	Δ_{max} [mm]	Δ_{perm} [mm]	Δ_{exp} [mm]	CPU time [h:min:s]*	$\frac{\Delta_{perm}}{\Delta_{exp}} \cdot 100\%$
30 Bar (Figure ..)	-	-	19	26:48:21	-

*Note that the CPU time are somewhat affected by the workload on the CPU cluster, thus only the general trends of computational time are outlined.

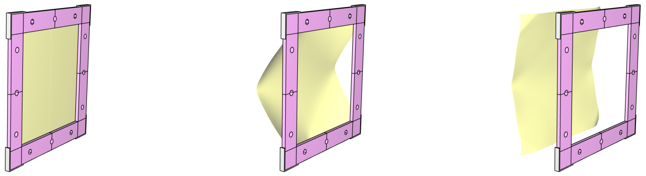

(a) T = 0s **(b)** T = 0.140s **(c)** T = 0.160s

Figure 7.17: Time-lapse of deformation Friedlander load field

These results along with the results in section 7.2.1.1 indicates that a further investigation into the experiments at NTNU should be performed.

7.2.2 Multi-Material Eulerian

An attempt was made to recreate the NTNU experiments from section 4.1 numerically by applying the MME formulation investigated in section 6.2.

Introduction

The numerical simulations will be compared alongside experimental data from section 5.1.1, and the result will serve as validation of the established numerical model from section 6.2. Potentially the analyses could help describe the airflow better and perhaps explain the difference between the pressure-readings from 2009 and 2013.

Procedure

It is assumed that the experiment can be modelled with radial symmetry which allows the use of the 2D element formulation described in section 6.2.2, thus reducing the computational need. Assuming radial symmetry would imply that the plates are circular. However since the placement of the pressure sensors (shown in figure 4.7) are possible to represent with radial symmetry, a correct plate geometry would only lead to negligible differences when compared with the experimental data. The difference between the recorded pressures in the sensors when employing a circular and square plate is assumed negligible. The numerical models (shown in figure 7.18) are created with the aforementioned 2D element formulation, employing the 5x5 [mm] elements based on the recommendation from section 6.2. The numerical parameters are identical as the ones employed in section 6.2.

(a) Pressure tank in MME analysis

(b) Impact chamber in MME analysis

Figure 7.18: Geometry used in the 2D MME analysis

The steel encapsulating the main tank, barrel and impact chamber is represented by restricting the nodes along the top edge of the system against any directional flow, which is illustrated in figure 7.19.

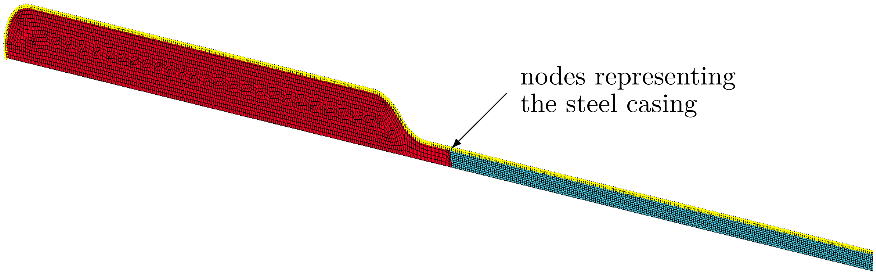

Figure 7.19: Illustration of the MME model boundary conditions

Air is modelled by employing the material and EOS parameters presented in section 3.4, and modifying the material and EOS parameter in order to accommodate for the pressurized air in the main tank. The modified parameters are shown in table 7.4.

Table 7.4: Parameters for the pressurized air in the main tank employed in the simulations

Experiment	ρ $[kg/m^3]$	E0 $[J/m^3]$
2009 (40 Bar)	50.1	10^7
2013 (30 Bar)	37.6	7.5×10^6

Tracers are positioned on the plate as shown in figure 7.20a in correspondence with the pressure transducer positioning as shown in figure 4.7b. Two models are created based on both the 2009 (shown in figure 7.20a) and 2013 (shown in figure 7.20b) geometry. The small tank (or firing section shown in figure 4.2) is not modelled as it was shown that by using only the main tank gives approximately the same results as using both (See appendix A.1 figure A.1c and A.2a).

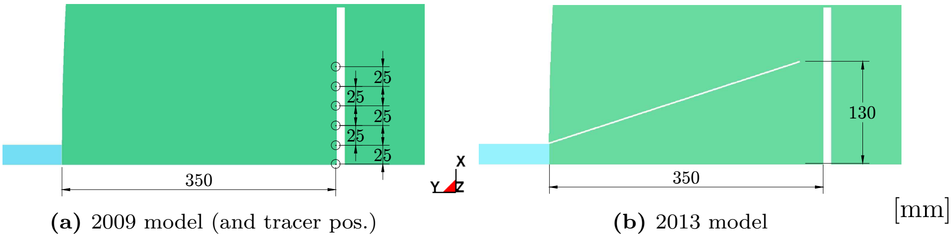

(a) 2009 model (and tracer pos.)

(b) 2013 model

Figure 7.20: MME models employed in the 2009 and 2013 simulations

The plate is modelled as completely rigid, and so is the funnel employed in the 2013 simulation (shown in figure 7.20b).

Results

The peak reflected pressure and impulse from the 2009 simulation are compared alongside the experimental results from section 5.1.1 in table 7.5. Figure 7.24 shows a pressure time-history comparison between the tracer-readings from the mid-pont sensor in the numerical simulation with the pressure time-history from the corresponding sensor in the experiments. The data from the numerical simulation suffered from a lot of numerical noise, such that the data has been filtered using the same 2. order 100 Hz lowpass Butterworth algorithm employed on the experimental data (see appendix A.2).

Table 7.5: A comparison between experimental data from 2009, and the corresponding numerical simulation

Sensor	P_r $[kPa]$	$P_{r,exp}$ $[kPa]$	i_r $[kPas]$	$i_{r,exp}$ $[kPas]$
1	372.46	299.49	37.86	54.30
7	376.20	246.31	31.65	31.90
8	553.75	253.60	21.01	14.83
9	234.77	180.36	4.95	5.42
11	61.99	266.31	1.79	30.03

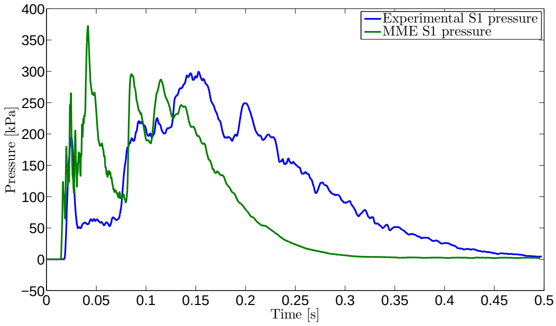

Figure 7.21: Comparison between pressure time histories from the experiment and simulations (2009)

Based on the comparison in table 7.5, and figure 7.21, it is observed a clear correlation between the numerical simulation and the experimental data. This is especially noticeable by comparing the impulses from sensors 7 and 9 in table 7.5, and the peak pressures shown in figure 7.21.

A time-lapse of the simulation is shown in figure 7.22.

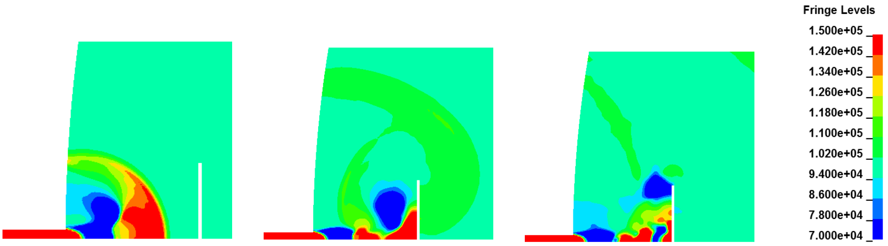

(a) T=0.015s **(b)** T=0.016 **(c)** T=0.017

Figure 7.22: A time-lapse of the airflow in impact chamber for the 2009 simulation [Pa]

By examining the airflow (shown in figure 7.22), it is observed a lot of suction near and around the plate. A time-lapse describing the air evacuating the main tank in the 2009 simulation is shown in figure 7.23.

(a) Pressure tank airflow (T=0.0s)

(b) Pressure tank airflow (T=0.0019999s)

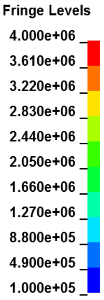

(c) Pressure tank airflow (T=0.0039994s)

(d) Pressure tank airflow (T=0.0059997s)

(e) Pressure tank airflow (T=0.0079996s)

Figure 7.23: Airflow in Pressure tank time-lapse

The peak reflected pressure and impulse from the 2013 simulation are compared alongside the experimental results from section 5.1.1 in table 7.6. A pressure time-history comparison is shown in figure 7.24, employing the same sensor-position as for the 2009 experiments.

Table 7.6: A comparison between experimental data from 2013, and the corresponding numerical simulation

Sensor	P_r $[kPa]$	$P_{r,exp}$ $[kPa]$	i_r $[kPas]$	$i_{r,exp}$ $[kPas]$
1	167.10	164.29	15.75	15.72
7	117.70	144.46	10.56	10.81
8	71.02	67.35	4.13	3.53
9	72.99	23.88	2.88	-4.74
11	157.07	5.87	7.39	-15.58

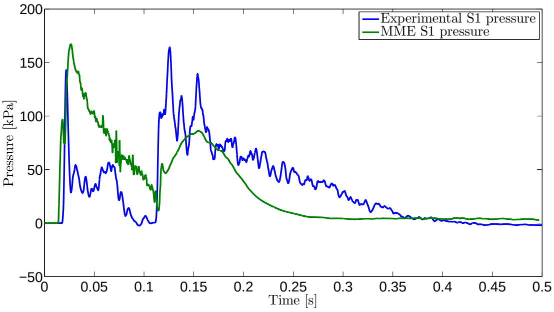

Figure 7.24: Comparison between pressure time histories from the experiment and simulations (2013)

By examining the data in table 7.6 and the plots in figure 7.24 it is observed once again similarities between the simulation and experimental data, which is especially noticeable for sensors 1, 7 and 8.

A time-lapse of the simulation is shown in figure 7.25.

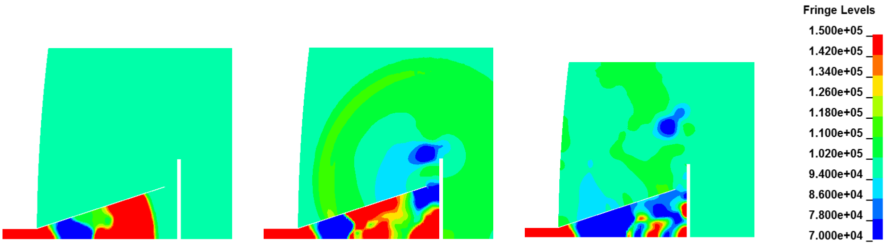

(a) T=0.015s **(b)** T=0.016 **(c)** T=0.017

Figure 7.25: A time-lapse of the airflow in impact chamber for the 2013 simulation [Pa]

By observing the airflow time-lapse in figure 7.25, it is noticed a lot of suction around where sensor 9 and 11 are placed, indicating that there is a lot of turbulence around the plate caused by the funnel. The presence of turbulence could explain the lowered pressure and subsequently lowered impulse recorded by the sensors in the 2013 experiment compared to the 2009 experiment.

Based on the results in this section it is evident that the MME model established in section 6.2 can be utilized with success on a different problem than what the model was calibrated for.

Even though the numerical simulations performed in this section are idealized cases of the experiments, the observed correlation between simulated and experimental data suggests that the gas gun experiments are performed within a controllable environment with manageable error-sources.

In section 5.1.1 it was suggested that some of the sensors in the experiment described in section 4.1.3.1 malfunctioned because it recorded large values of negative pressures with corresponding large values of negative impulses. These numerical simulations helps us to understand why the sensors at the periphery of the plate (see sensor 9 and 11 in figure 4.7 and experimental results in table 7.6) recorded such unexpected values and why the numerical simulations in section 7.2.1 results in such a different behaviour compared to what was observed in the experiments in section 5.1.2. The added funnel described in section 4.1.4 alters the air flow in such a way that in reality the sensors far from the center records the side-on pressure instead of the reflected pressure. This effect is illustrated in figure 7.26.

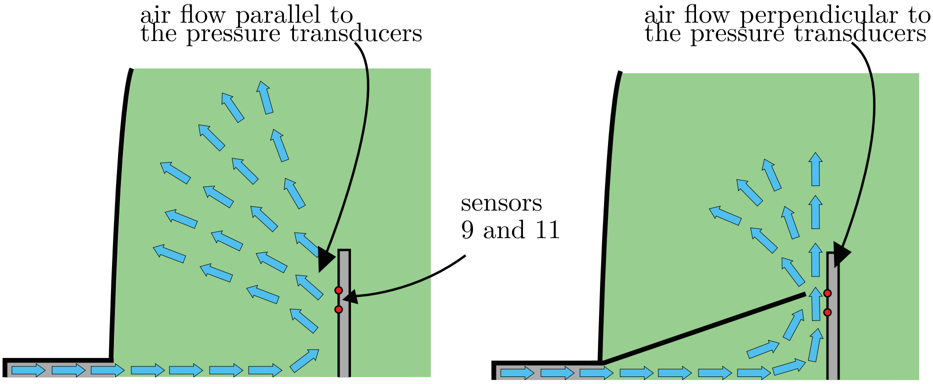

Figure 7.26: Gas gun vacuum

If this should be a subject for further study it is recommended to perform Lagrangian analyses without the loads originating from sensors 9 and 11

7.3 Experiments at RAUFOSS

As mentioned in section 7.1 the experiments at Raufoss described in section 4.2 will be subject to a range of different numerical simulation techniques in this chapter. It starts out with the most basic simulations and ends up with complicated procedures to investigate which of the techniques that best recreates the observed plate deformations.

7.3.1 Lagrangian

Introduction

Initially we want to recreate the deformation by employing a purely Lagrangian approach. The main procedure would normally be to apply measured head-on pressures as loads across the whole exposed area of the plate. However this becomes troublesome in this study because the experiments performed in section 4.2.1 differs in various areas compared to the experimental setup with the plates in section 4.2.2.

Several problems arise if one wanted to employ the experimental pressure data in the plate setup:

- The pressure experiments only recorded the side-on pressure and not head-on pressure. As outlined in section 2.1.2.4 the head-on pressure or so called reflected pressure is substantially higher compared to the side-on pressure.
- The blast load parameters recorded in the side-on experiments are not at the same standoff distances as the plate experiments, such that the highly non-linear blast parameters will change when the standoff is altered.
- The explosives were placed on the ground itself in the side-on pressure experiments, thus ground reflections are amplifying the recorded pressure. In the plate experiments, the standoffs are small relative to the distance between the explosive and the ground. This causes only the incident waves to hit the plate as the waves that are reflected off the ground will not fuse with the original waves before it hits the target plate.

When the pressure-history is not given for a problem, the natural thing to do would be to employ a standard method such as CONWEP or the UFC to estimate the blast load parameters. The values in these standards are fitted from live experiments and will only yield approximate values to the blast load parameters. The numerical simulation with these parameters would then not be a test of the Lagrangian numerical technique, but rather a test of the exactness of the employed standard. To circumvent this problem, the study of the Lagrangian technique will be carried out in two parts:

Part one will employ the UFC standard to estimate the blast load and apply this load on a finite element model. This will test how well the UFC can be employed to recreate the expected deformations in this particular experiment.

Part two will make use of the blast module embedded in LS-DYNA, *LOAD-BLAST-ENHANCED (LBE). The procedure is purely Lagrangian and applies a blast load on specified segments as a pressure load and can be defined to include mach-reflection and surface-effects. The blast load parameters are taken from CONWEP but no pressure data is being processed by the analyst.

Both parts are in essence purely Lagrangian, but it is only the second part that will be a test of the Lagrangian technique as it is LS-DYNA that treats the blast load parameters and not the analyst.

7.3.1.1 Estimating the Deformation with the UFC

In this section the pressure load generated by the explosive agent will be represented by a Friedlander equation for each standoff.

Procedure

As outlined in section (2.1.2.5) the blast load parameters are estimated from plots in the UFC standard. The full calculations of the blast load parameters can be seen in appendix C.1. A short summary of the values in the Friedlander equations are given in the table 7.7 and illustrated in figure 7.27.

Table 7.7: Values used in the Friedlander equations

R $[mm]$	P_r^+ $[kPa]$	i_r^+ $[Pas]$	T^+ $[s]$	b [-]
300	24131.65	6.83E+02	2.17E-04	6.49
400	11445.30	4.55E+02	5.55E-04	12.86
450	8480.55	3.89E+02	8.15E-04	16.70
550	4826.33	2.99E+02	9.78E-04	14.68

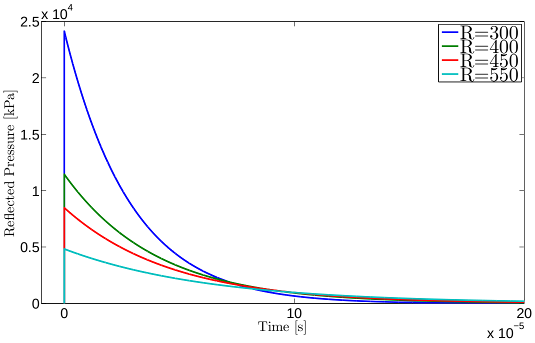

Figure 7.27: Reflected pressure time-history based on calculations from the UFC

The load curves from figure 7.27 are applied to finite element models of the plate with appropriate boundary conditions. The numerical model is depicted in figure 7.28, and the simulations are performed for 15 ms whereas the displacement of the center-node is monitored.

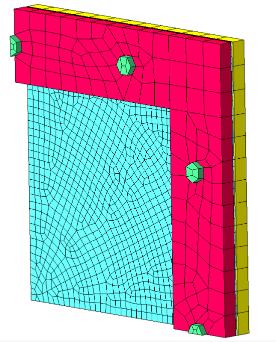

Figure 7.28: Lagrangian model used for all Raufoss simulations

The numerical model is based on the boundary conditions in figure 4.15. As described in section 6.1.1 the frame and clamps are assumed rigid. The newly added bolts are also assumed rigid and restricted from any movement or rotations in any directions. The Lagrangian model is described in section 6.1. The plate is modelled as 2 mm thick with holes to account for the plate being fastened with bolts.

Results

The results are summarized in table 7.8 and time-displacement plots can be seen in figure 7.29. The simulations required a shorter timestep than the standard recommendation from LS-DYNA, thus having to employ a timestep scaling factor of 0.3.

Table 7.8: Lagrangian (UFC) simulations displacement comparison

R $[mm]$	Δ_{max} $[mm]$	Δ_{perm} $[mm]$	Δ_{exp} $[mm]$	CPU time [h:min:s]*	$\frac{\Delta_{perm}}{\Delta_{exp}} \cdot 100\%$
300	34.55	30.50	32.19	[00:10:45]	94.75 %
400	23.96	20.00	26.93	[00:11:41]	74.27 %
450	20.85	17.10	24.07	[00:10:33]	71.04 %
550	16.37	10.90	18.47	[00:07:02]	59.01 %

*Note that the CPU times are affected by the workload on the CPU cluster, thus the numbers are only outlines of what one could expect from such analyses.

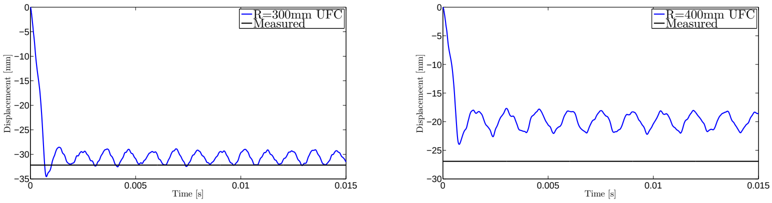

(a) R = 300 mm **(b)** R = 400 mm

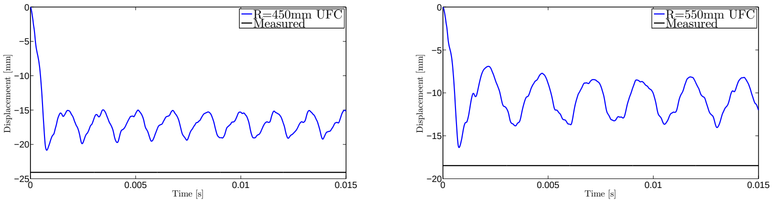

(c) R = 450 mm **(d)** R = 550 mm

Figure 7.29: Lagrangian (UFC) deflection time-history plots by standoff

We observe from the resulting time-displacement plots that the permanent deflection is underestimated for all standoff distances. The underestimation is likely caused by many combining factors, some of them mentioned below:

- The charge geometry is not correct. The UFC only have tables listed for spherical and hemispherical charges such that the load is underestimated. [23] states that the load from a cylindrical charge may exceed the load from a spherical charge by a ratio of five to one, while [22] estimates a scaling factor of 1.5 - 2.0.
- The reflected pressures and impulses in the UFC have an infinitely rigid wall as a reference point. A deformable section will have a relative movement that will lead to a reduction of the pressure load. This is not taken in to account in a purely Lagrangian approach. This will lead to an increased pressure load and offsets the errors in these analyses.
- The pressure loads in the Lagrangian formulation does not follow the deformable geometry (as shown in figure 7.30)
- The method of converting to TNT-equivalency by ratios of detonation heat is as outlined in [23], a bad approximation.

The results were inaccurate but the computational time of the analyses were short and the description of the load conditions were very easy to obtain. The familiarity that most analysts have with the classic Lagrangian approach also minimizes the risk of user-end errors in the setup of the numerical model. This approach might be useful for a concept study where a lower level of accuracy is sufficient.

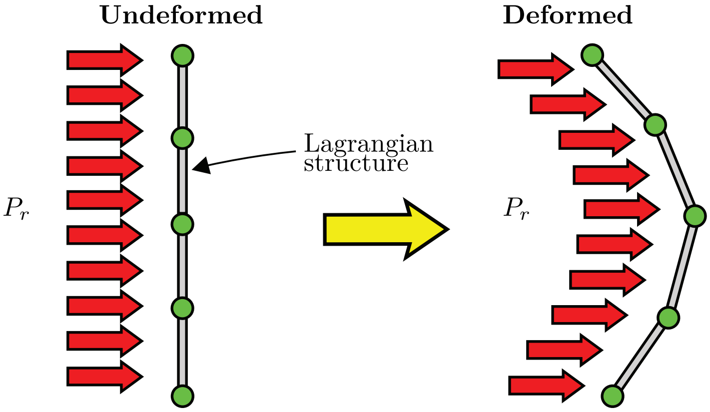

Figure 7.30: Illustration of the pressure orientation in an UEL

7.3.1.2 Estimate the Deformation with LBE

Procedure

The *LOAD_BLAST_ENHANCED (LBE) is based on empirical test data, thus no data for the gas parameters are needed. The LBE can include mach reflections and other ground effects, but this was not employed here, the assumption being that the standoffs are small relative to the height off the ground such that the reflected waves does not fuse to form a mach-front. The only input needed in the LBE is the TNT equivalent weight and the standoff. As to date, no other charge geometries than a spherical or hemispherical charge is included in the LBE. [23] states that the TNT equivalent weight of C4 is a function of the standoff itself. The recommended values being between 1.2 and 1.4. A middle value of 1.3 was chosen in these simulations.

The same numerical model as in the previous section was employed and is depicted in figure 7.28.

Results

Table 7.9: Lagrangian (LBE) simulations displacement comparison

R $[mm]$	Δ_{max} $[mm]$	Δ_{perm} $[mm]$	Δ_{exp} $[mm]$	CPU time [h:min:s]*	$\frac{\Delta_{perm}}{\Delta_{exp}} \cdot 100\%$
300	32.54	28.65	32.19	[00:13:04]	89.00 %
400	24.59	20.40	26.93	[00:13:53]	75.75 %
450	21.73	17.75	24.07	[00:13:33]	73.74 %
550	17.40	12.25	18.47	[00:08:52]	66.32 %

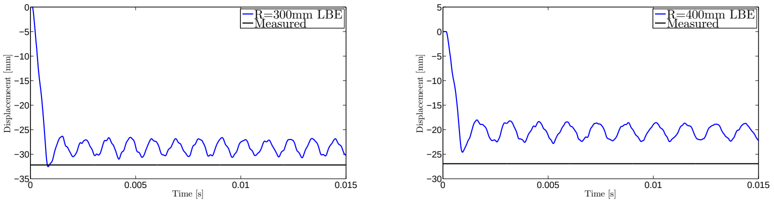

(a) 300 mm **(b)** 400 mm

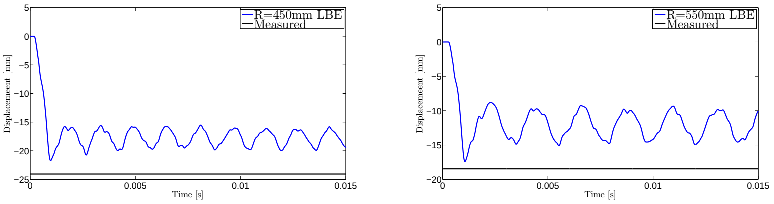

(c) 450 mm **(d)** 550 mm

Figure 7.31: Lagrangian (LBE) deflection time-history plots by standoff

As we observe from the results in table 7.9, the deformations were underestimated in this approach. The LBE simulations have the same pitfalls as the UFC approach outlined in the previous section. An obvious error source is that the TNT equivalency of the C4 were not accurately described as this ratio changes with increased standoffs. The LBE does however take in to account the spatial placement of the explosive, thus having different arrival times of the blast wave to different parts of the plate. This will however be minor alterations to the blast load for small structural parts such as this.

The LBE proved to be slightly more accurate than the UFC approach and is by far the easiest to employ of the two as no hand calculations or approximate chart values were employed. The computational time is about the same, and the risk of user-end errors are minimal as there were only two input parameters. For initial calculations to estimate structural deformation or for concept studies the LBE seems to be the preferable alternative of the two.

7.3.2 Multi-Material Eulerian

Introduction

In this section a numerical simulation of the side-on pressure experiment described in section 4.2.1 will be performed.

Procedure

The numerical model employed is a 2D axisymmetric model based on the recommendations from section 6.2, shown in figure 7.32.

Figure 7.32: Model used in simulating side-on pressure

Tracers are placed along the ground of the model at the same distances as the standoffs in the experiment (shown in table 4.3). See appendix C.2 for the associated keyword file.

Results

The results from the side-on pressure simulation are presented in table 7.10, followed by two pressure time-history comparisons with experimental data for the sensors at $R = 0.6$ m, and $R = 1.4$ m.

Table 7.10: The results from the side-on pressure simulation at Raufoss (2010)

Sensor	P_{so} $[kPa]$	$P_{so,exp}$ $[kPa]$	i_{so} $[Pas]$	$i_{so,exp}$ $[Pas]$	CPU time [h:min:s]
1	2195	1743	161	24.5	[00:13:53]
		1577		24.0	
		3223		20.0	
		1296		19.2	
5	222	128	53	4.0	[00:13:53]
		138		4.1	
		345		4.0	
		214		4.1	

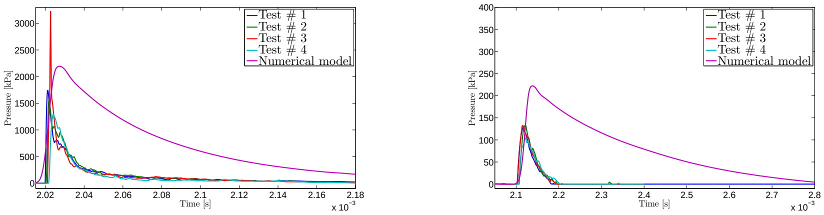

(a) Sensor 1 **(b)** Sensor 5

Figure 7.33: Side-on pressure comparison

A time-lapse of the simulation is shown in figure 7.34.

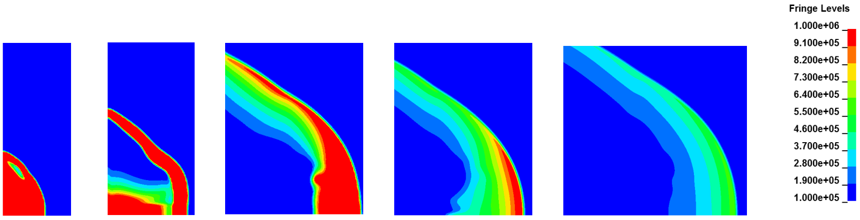

(a) T=4e-5s **(b)** T=8e-5s **(c)** T=2.4e-4s **(d)** T=4.4e-4s **(e)** T=6.8e-4s

Figure 7.34: A time-lapse of the side-on pressure simulation at Raufoss (2010) $[Pa]$

Based on the results in table 7.10 and figure 7.33, it is evident that the impulse and peak side-on pressure is overestimated in the numerical simulation. The study in section 6.2 showed that a further refinement of the mesh converges towards an even higher peak pressure and impulse which would indicate that the chosen element size is not the source of the discrepancy.

Because the experimental and numerical results were so inconsistent a validation of the recorded pressure-data from Raufoss was performed by comparing the data with values calculated with the UFC. The values in the UFC were calculated employing the scaled distance equation (2.15), and a chart in [23] describing positive phase shock wave parameters for ground explosions. Bear in mind that values from the UFC are for hemispherical shaped charges. Cylindrical charges are expected to generate larger peak pressures and impulses according to [29, 22]. The standoff at $R = 600$ mm was used as the benchmark distance. Because the UFC employ imperial units, an initial unit-conversion needs to be performed:

$$\left.\begin{array}{r} W_{C4} = 0.14 \text{ kg} \Rightarrow W_{C4} \approx 0.31 \text{ lb} \\ R = 0.60 \text{ m} \Rightarrow R \approx 1.96 \text{ ft} \end{array}\right\} \tag{7.8}$$

The TNT equivalent mass of C4 used in the experiments are calculated employing a scale factor of 1.3 based on the recommendations from table 2.1 and [31].

$$W_{TNT} = 1.3 * W_{C4} = 1.3 * 0.31 \text{ lb} \approx 0.4 \text{ lb} \tag{7.9}$$

The scaled distance formula (2.15):

$$Z = \frac{1.96 \text{ ft}}{0.4^{\frac{1}{3}} \text{ lb}^{\frac{1}{3}}} \approx 2.66 \frac{\text{ft}}{\text{lb}^{\frac{1}{3}}} \tag{7.10}$$

The values obtained from the UFC are summarized in table 7.11.

Table 7.11: Values obtained from the UFC

Parameter	Imperial units	SI units
$P_{so,UFC}$	195 psi	1345 kPa
$i_{so,UFC}$	19.2 psi-ms	132.1 Pas
$t_{0,UFC}$	1.11 ms	1.11 ms

A Friedlander was created based on the parameters in table 7.11, and it is plotted alongside the pressure time histories from the numerical simulation and an example of the experiments in figure 7.35.

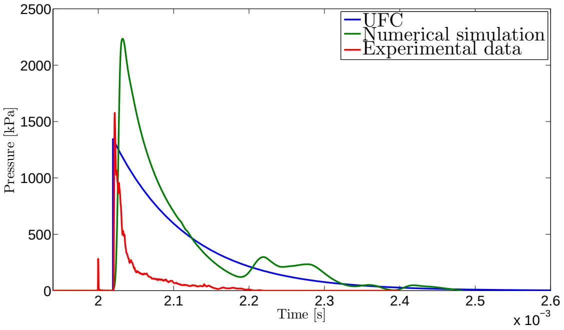

Figure 7.35: Comparison of the data from the UFC, numerical simulation and experimental data

A comparison between the numerical, UFC and experimental data is shown in table 7.12

Table 7.12: The results from the side-on pressure validation for data from Raufoss (2010)

P_{so} $[kPa]$	$P_{so,UFC}$ $[kPa]$	$P_{so,exp}$ $[kPa]$	i_{so} $[Pas]$	$i_{so,UFC}$ $[Pas]$	$i_{so,exp}$ $[Pas]$
2195	1345	1743	161.0	132.1	24.5
		1577			24.0
		3223			20.0
		1296			19.2

By comparing the results in table 7.12, it is observed that the UFC slightly underestimates the peak side-on pressure, and greatly overestimates the impulse compared to the experimental data.

Based on the results in this section it is shown that both the numerical simulations and the UFC overestimates the impulses compared to the experimental data. This indicates that the discrepancies between the experiment and simulation might be explained by inaccuracies in the recorded data. The differences could also be explained by several combining factors, whereas some of them are presented here:

- The influence of friction between the shock front and the ground
- The point of detonation might differ between the experiment and simulation
- The charge mass and geometry
- The horizontal alignment of the charge and sensors in the experiment
- The small steel tap placed in front of the charge might impact the experimental results, and is not accounted for in the simulation
- The possibility of instrumental errors

7.3.3 Uncoupled Eulerian Lagrangian (UEL)

UEL analyses will be employed in order to numerically represent the blast loaded plate experiments described in section 4.2.2.

7.3.3.1 UEL Employing a Discretized Pressure Distribution

Introduction

In an UEL, pure MME simulations are performed in order to generate load curves that subsequently are employed in separate Lagrangian analyses.

Procedure

Because the experiment cannot be represented with rotational symmetry, the recommended 2D to 3D mapping technique from section 6.2.5 is employed. Additional MME analyses employing only 3D elements are performed to further illustrate the benefits of employing this method. The plate is represented in the MME simulations by a set of nodes acting as reflective boundaries, thus modelling the plate as completely rigid shown in figure 7.36b.

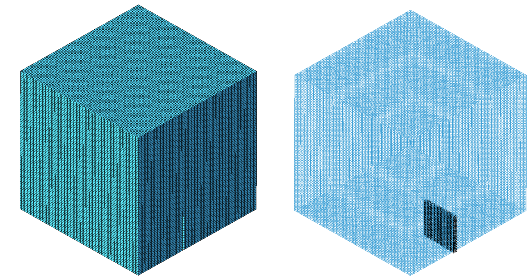
(a) Volume **(b)** Rigid plate

Figure 7.36: Example of MME model geometry employed in UEL ($R = 300$ mm)

Tracers have been positioned in front of the rigid boundaries in the MME analyses (see figure 7.37) such that the pressure time-history can be recorded. The Lagrangian model is identical to the one employed in section 7.3.1 and shown in figure 7.28. The sectioning of the mesh has been adapted to the tracer positions shown in figure 7.37 such that it creates a perfect discretization of the pressure distribution.

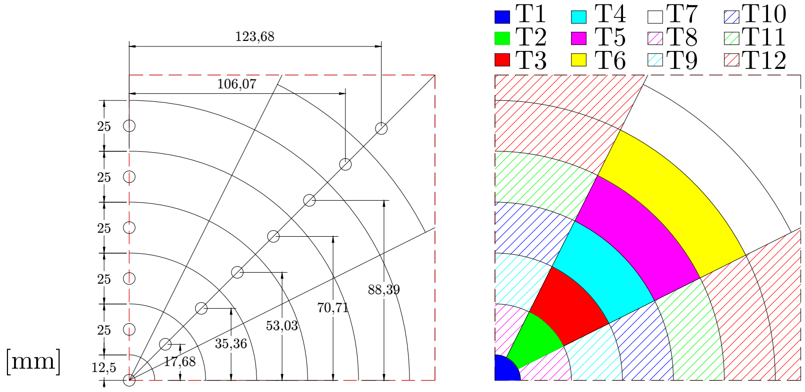

(a) Sensors used for load curve data **(b)** Sensors tributary area

Figure 7.37: Tracer positioning and corresponding tributary area

In the 2D to 3D mapping analyses, the blast wave will be allowed to propagate in the 2D MME domain until it has reached approximately 100 mm from the reflected boundaries representing the rigid plate. This will allow the blast wave propagation to be optimally represented by a fine mesh for as long it is possible without disrupting the airflow around the plate.

Results

The results from the analyses are compared alongside experimental data in table 7.13, and deflection time-histories from all the simulated standoffs are shown in figure 7.38.

Table 7.13: UEL simulations displacement comparison

R $[mm]$	Δ_{max} $[mm]$	Δ_{perm} $[mm]$	Δ_{exp} $[mm]$	CPU time [h:min:s]*	$\frac{\Delta_{perm}}{\Delta_{exp}} \cdot 100\%$
UEL analyses employing mapping from 2D to 3D					
300	30.88	27.40	32.19	[00:58:41]	85.12 %
400	26.85	23.50	26.93	[01:31:42]	87.26 %
450	24.47	21.00	24.07	[01:44:27]	87.25 %
550	18.77	16.20	18.47	[01:43:13]	87.71 %
UEL analyses employing only 3D elements					
300	20.41	17.00	32.19	[00:56:38]	52.81 %
400	16.62	11.50	26.93	[10:25:16]**	42.70 %
450	15.02	9.00	24.07	[03:09:19]	37.39 %
550	13.24	4.00	18.47	[01:06:36]	21.66 %

* Note that the reported CPU-time for the 2D to 3D mapped results are the total time for both MME analyses and the Lagrangian analyses.

** The reported CPU-time is not representative for the analysis, as it probably is due to a heavy work load on the CPU cluster.

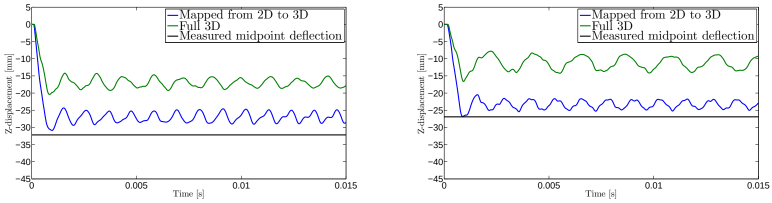

(a) R = 300 mm **(b)** R = 400 mm

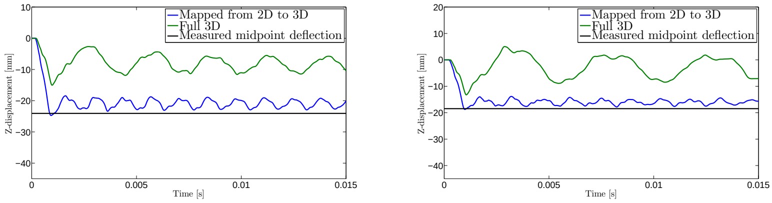

(c) R = 450 mm **(d)** R = 550 mm

Figure 7.38: Deflection time-histories for the UEL analyses

By examining the permanent deflection-results in table 7.13, it is evident that the deformation is underestimated for both the 2D to 3D mapping technique and by employing a full 3D model. It is also observed that the deformation increases when using the mapping technique compared to the full 3D approach. This further supports the results in section 6.2.4 which showed that MME analyses employing 10x10x10 $[mm]$ 3D elements underestimates the impulse and peak pressure. This shows the importance of properly describing the initial blast wave propagation with a sufficiently fine mesh.

A time-lapse describing the gas-plate interaction is presented in figure 7.39 followed by a figure describing how the results from the last cycle in the 2D domain (figure 7.40a) is mapped over to the first cycle in the 3D domain (figure 7.40b).

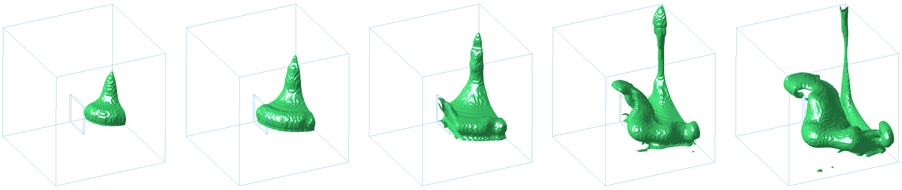

(a) T = 5e-5s **(b)** T = 9.97e-5s **(c)** T = 1.796e-4s **(d)** T = 3.197e-4s **(e)** T = 5.897e-4s

Figure 7.39: A time-lapse of the MME analyses (R = 300 mm)

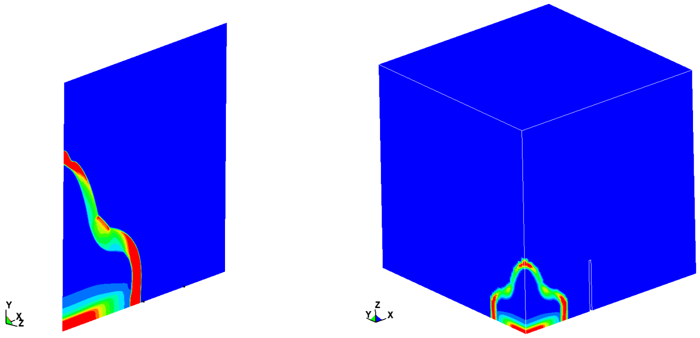

(a) Last 2D cycle **(b)** First 3D cycle

Figure 7.40: Mapping from 2D to 3D explained (300 mm standoff)

By examining figure 7.40b and 7.40a it can be observed that the result mapped from 2D to 3D looses some fidelity. This is expected because the 3D domain employs elements that are ten times larger.

The pressure loads generated in the MME analyses does not consider FSI effects, thus resulting in an underestimation of deflection (see figure 7.30). Another important aspect to consider is that the recorded pressure-histories in the MME simulations are inflated because the plates are assumed rigid, thus resulting in overestimating the applied loads in the Lagrangian analyses. This would counteract the effects from the lack of FSI consideration. An overview of the main causes suspected to be responsible for the discrepancies between numerical and experimental data is listed below:

- The lack of FSI effects
- The discrete pressure distribution
- The coarse mesh employed in the 3D model
- The plate being modelled as completely rigid

In order to perform these analyses with sufficient accuracy, the analyst have to perform three separate simulations;

1. A 2D MME analysis with a fine mesh
2. A 3D MME analysis with a coarse mesh
3. A Lagrangian analysis

The amount of time required to set up these simulations are not covered in the CPU time, and should therefore be kept in mind when comparing this method to the alternatives presented in this thesis.

7.3.3.2 UEL Employing a Continuous Pressure Distribution

Introduction

As explained in section 7.2.1.2 the large discrete pressure variations across the tributary area boundary (shown in figure 7.37) might give rise to unrealistic deformations in the numerical simulations. To eliminate these large discrete changes, a continuous load field can be interpolated from the tracer data and applied to the numerical model as functions of space and time in IMPETUS.

Procedure

The same procedure as in section 7.2.1.2 was applied to create the Friedlander load field. Load curves were fitted from the pressure data obtained from the uncoupled multi-material Euler simulations in section 7.3.3.1. The peak pressure and impulse were kept constant while the decay coefficient and positive duration were varied to obtain the best fit. Examples of the interpolated Friedlander functions are depicted in figure 7.41.

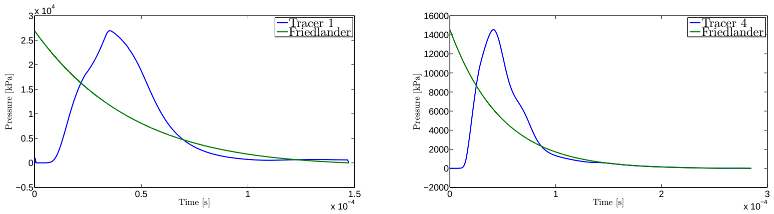

(a) Tracer 1 **(b)** Tracer 4

Figure 7.41: Examples of interpolated Friedlander functions

From the curve-fitted functions the $P_r(x,y)$, $T^+(x,y)$ and $b(x,y)$ variable functions were interpolated with respect to space and augmented in to a Friedlander equation that is identical to equation (7.2.1)

Examples of the interpolated variable functions are depicted in figure 7.42.

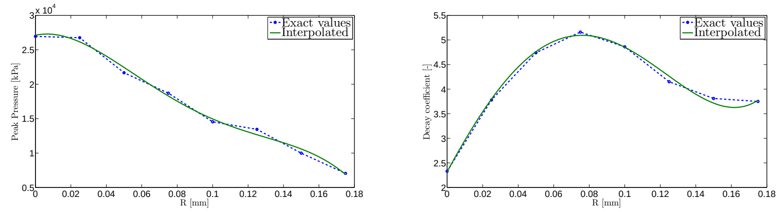

(a) Peak pressure **(b)** Decay coefficient

Figure 7.42: Examples of interpolated Friedlander functions

The Friedlander load field was then applied to a numerical model identical to the one employed for in the Lagrangian simulations in section 7.3.3.1

The data from the numerical simulations in section 7.3 represents a much more ideally shaped blast wave compared to the gas gun experiment. This result is a better fit for the variable functions and should consequently yield a better prediction with respect to deformation.

Results

The results are presented in table 7.14 and time-displacement plots are seen in figure 7.43.

Table 7.14: The results from a UEL simulation employing a continuous pressure distribution

R $[mm]$	Δ_{max} $[mm]$	Δ_{perm} $[mm]$**	Δ_{exp} $[mm]$	CPU-time [h:min:s]*	$\frac{\Delta_{perm}}{\Delta_{exp}} \cdot 100\%$
300	29.75	26.10	32.19	02:15:43	81.08 %
400	27.17	23.20	26.93	02:15:02	86.15 %
450	24.48	19.90	24.07	02:12:19	82.68 %
550	18.88	13.80	18.47	02:12:03	74.72 %

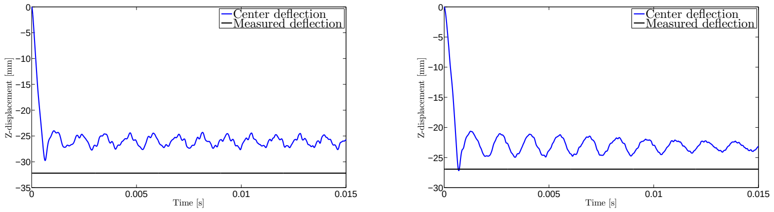

(a) R = 300 mm　　**(b)** R = 400 mm

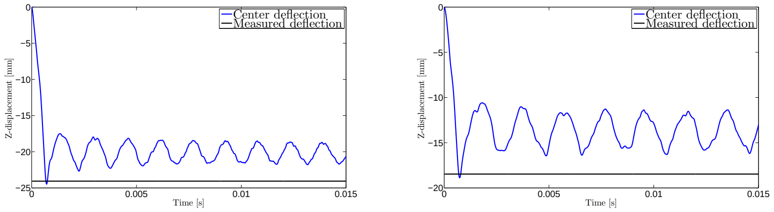

(c) R = 450 mm　　**(d)** R = 550 mm

Figure 7.43: UEL Friedlander displacement time history-plots

This method was specifically designed to investigate if the tributary area approach contribute to noticeable errors in a Lagrangian approach. Concluded from the simulation output the Friedlander field approach does not have a positive impact regarding the correlation between the numerical and experimental results. The error is larger compared to the tributary area approach in section 7.3.3.1, and this implies that the tributary area is not the root of the displacement errors in the uncoupled calculations.

The fact that the Friedlander-field approach gives yields less deflection than the simulations in section 7.3.3.1 probably stems from the following:

- The interpolated field functions does not perfectly fit the sensor data.
- This formulations does not take in to account the time delay at which the pressure hits the different parts of the plate
- The tributary area approach in section 7.3.3.1 overestimates the deflection
- An increased loading rate

7.3.4 Coupled Eulerian Lagrangian (CEL)

Simulations employing a CEL formulation will be used to simulate the blast loading plates experiments at Raufoss (2010) described in section 4.2.

Introduction

The explosive process will be represented with the MME model from section 6.2. The Lagrangian plates and corresponding supports are identical to the ones in section 7.3.3. The different parts are created with separate meshes, and are illustrated in figure 7.44.

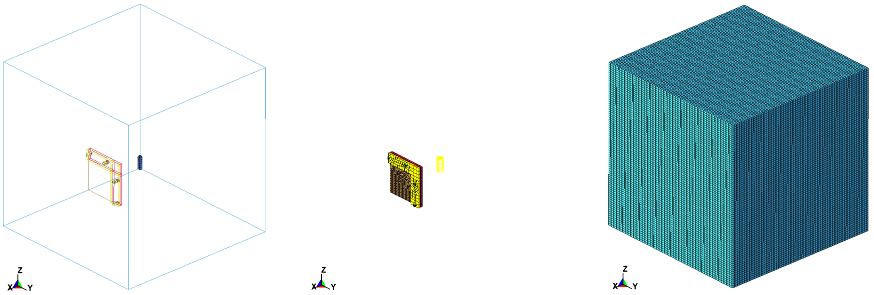

(a) Combined **(b)** Lagrangian model **(c)** MME air volume

Figure 7.44: An overview of the different parts in a CEL analysis (R =300 mm)

Procedure

The same 2D and 3D mapping technique is employed as in the UEL analyses in section 7.3.3. In order to minimize the number of simulations, the same 2D results from section 7.3.3 are mapped in to the 3D domains in this section. Two additional analyses will be performed by employing full 3D models. One with 10x10x10 $[mm]$ elements, and the other with 5x5x5 $[mm]$ elements. Even though MME analyses using 5x5x5 $[mm]$ elements were previously disregarded, it was decided to perform a set of CEL analyses with these element sizes on NTNU's supercomputer VILJE with 16-32 MPP processors allocated.

The coupling between the MME fluids and the Lagrangian parts is the penalty-based method described in section 2.4.6.6 and illustrated in figure 2.30. The corresponding parameters are shown in the keyword file example in appendix C.3. After recommendations from [46], fully integrated shell elements were employed in order to increase the number of contact points for the pressure iteration process. As shown in section 6.1.1, shell elements with full and reduced integration generate sufficiently similar results.

In order to reduce the computational need and avoid the numerical instabilities observed in section 6.2, a simulation time of only 3 ms will be applied. The midpoint deflection will be monitored, and subsequently benchmarked against the experimental results from table 5.5.

Results

The results from the analyses are compared alongside experimental data in table 7.15, and deflection time-histories from all the simulated standoffs are shown in figure 7.45.

Table 7.15: Overview of the results from the CEL simulations

R $[mm]$	El. size $[mm]$	Δ_{max} $[mm]$	Δ_{perm} $[mm]$	Δ_{exp} $[mm]$	CPU time [h:min:s]*	$\frac{\Delta_{perm}}{\Delta_{exp}} \cdot 100\%$
CEL analyses employing the 2D to 3D mapping technique						
300	1,10	40.55	37.00	32.19	[11:26:27]	114.94 %
400	1,10	34.09	30.00	26.93	[11:26:33]	111.40 %
450	1,10	31.08	27.00	24.07	[11:32:33]	112.17 %
550	1,10	23.98	20.00	18.47	[11:47:39]	108.28 %
CEL analyses employing only 3D elements						
300	10	31.53	28.00	32.19	[23:53:00]	86.98 %
	5	33.95	30.70		[05:35:24]**	95.37 %
400	10	24.39	20.50	26.93	[23:38:00]	76.12 %
	5	28.92	25.00		[05:36:20]**	92.83 %
450	10	21.76	17.50	24.07	[22:09:00]	72.70 %
	5	25.93	21.10		[05:41:59]**	87.66 %
550	10	17.91	12.50	18.47	[22:41:00]	67.68 %
	5	21.92	18.10		[02:45:20]***	97.99 %

*The analyses are only performed for 3 ms, which should be kept in mind when comparing the CPU time with the other methods at 15 ms. The reported CPU times for the 2D to 3D mapping results are the total time of both MME analyses and the Lagrangian analyses.

** The analyses were performed employing NTNUs supercomputer VILJE running on 16 MPP processors.

*** The analysis was performed employing NTNUs supercomputer VILJE running on 32 MPP processors.

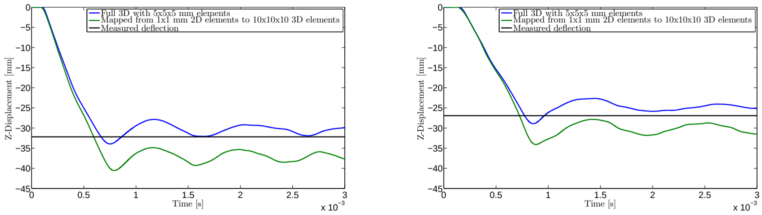

(a) $R = 300$ mm **(b)** $R = 400$ mm

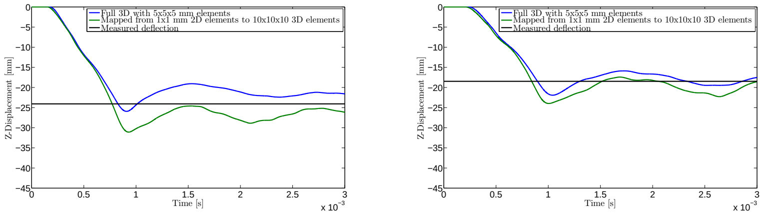

(c) $R = 450$ mm **(d)** $R = 550$ mm

Figure 7.45: Midpoint displacement time history comparison for the full simulation employing 5x5x5 $[mm]$ elements and the 2D to 3D mapping technique

Based on the results in table 7.15 and figure 7.45, it is observed once again that simulations with MME domains consisting of 10x10x10 $[mm]$ elements underestimates the plate deflection. This is confirmed by the results in sections 6.2 and 7.3.3. Comparing these with the results from UEL using similar element size, shows that the inclusion of FSI effects (shown in figure 7.46) increases the permanent plate deflection. The same effect is observed in the 2D to 3D mapping results, which overestimates the deflections compared to the experiments.

This indicates that the coarse mesh not only poorly represents the initial blast wave propagation, but also the air flow around the plate.

By employing the recommended 5x5x5 mm^3 elements in the MME domain, a relatively good representation of the plate deflection from the experiments is achieved. This further illustrate the importance of a sufficiently fine mesh in order to represent the initial blast wave propagation and the air flow around the plate.

An illustration describing the FSI effects on a structure is shown in figure 7.46.

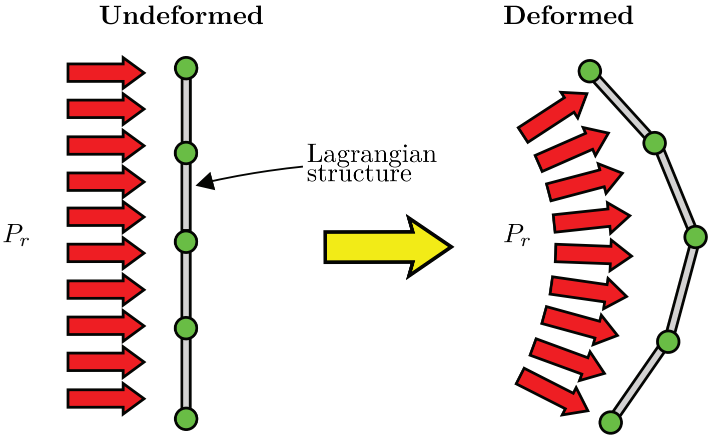

Figure 7.46: Illustration of the pressure orientation in an CEL

A time-lapse showing the gas-plate in the CEL analyses is shown in figure 7.47.

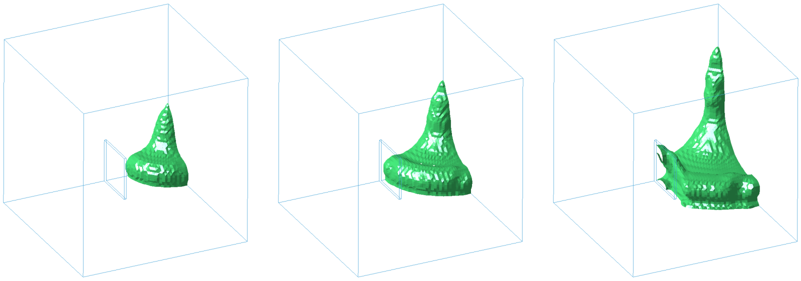

(a) T = 1e-4s (b) T = 3.4983e-4s (c) T = 5.9992e-4s

Figure 7.47: Time-lapse for a CEL at R = 400 mm

An overview of the suspected causes behind the discrepancies between numerical and experimental data is listed below:

- The mesh is too coarse in order to properly describe proper load conditions
- Leaking through the penalty coupling interface
- The approximations in pressure iterations

A lot of work is required by the analyst in order to create a acceptable CEL representation of the experiment. As one would expect a deep understanding of the associated theory presented in section 2.4.5 is required. However the analyst also needs to be aware of and understand the function of every numerical parameter associated with the analysis in question.

7.3.5 The Discrete Particle Method (DPM)

Introduction

As an alternative to the ALE formulation for simulating the fluid-structure interactions there is the DPM. The DPM have several advantages over an ALE formulation, both when it comes to computational effort and to establish a feasible numerical model. The DPM will be employed to try and recreate the displacement in the experiments performed at Raufoss (2010) described in section 4.2.

Procedure

The model geometry was imported from LS-DYNA in to IMPETUS to ensure that the numerical model were identical for both codes. The model is identical to the one employed in section 6.1.3 where the appropriate amount of particles that presented accurate results for a quarter symmetric model was determined. The different cases investigated are presented in table 7.16. The analyses were run for 15ms and the plates midpoint displacements were monitored.

Table 7.16: Case set-up for standoff based particle method simulations

R $[mm]$	C-4 mass $[g]$	Number of particles N_p
300	145	0.25×10^6
400		
450		
550		

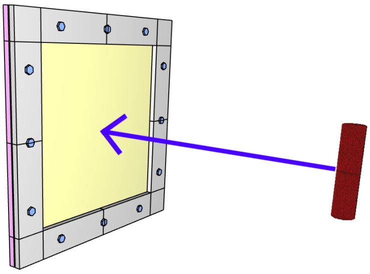

Figure 7.48: Numerical model used in standoff case-study explained

The model is reflected for visualization purposes.

Results

The results from the analyses are compared alongside experimental data in table 7.17, and time-displacement plots for the midpoint are depicted in figure 7.49.

Table 7.17: Standoff results for particle method

R $[mm]$	Δ_{max} $[mm]$	Δ_{perm} $[mm]$	Δ_{exp} $[mm]$	CPU time [h:min:s]*	$\frac{\Delta_{perm}}{\Delta_{exp}} \cdot 100\%$
300.00	36.27	33.30	32.19	[02:59:55]	103.45 %
400.00	30.52	26.95	26.93	[03:08:13]	100.07 %
450.00	27.59	23.90	24.07	[03:09:28]	99.27 %
550.00	21.93	17.25	18.47	[03:13:58]	93.39 %

*Note that the CPU time are somewhat affected by the workload on the CPU cluster, thus it is only the general trend of computational time that are outlined.

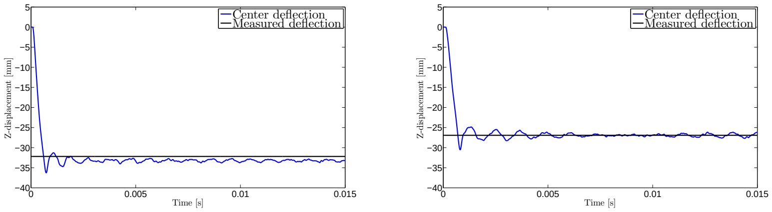

(a) R = 300 mm **(b)** R = 400 mm

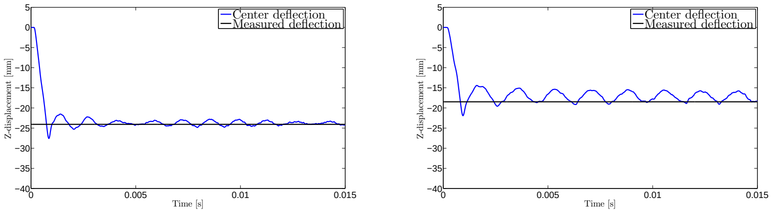

(c) R = 450 mm **(d)** R = 550 mm

Figure 7.49: Standoff Time-displacement history

A time-lapse of the numerical simulation can be seen in figure 7.50. The figure is reflected across both symmetry axes for visualization.

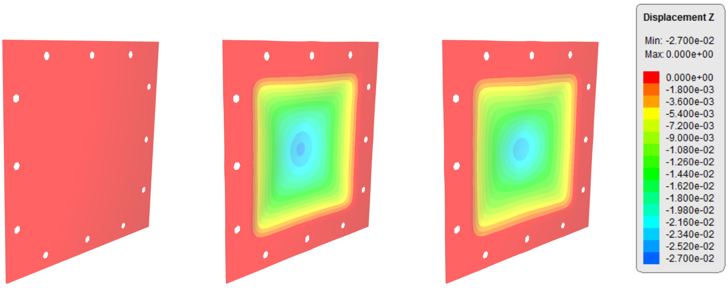

(a) T = 0s **(b)** T = 1e-3s **(c)** T = 6e-3s

Figure 7.50: Time-lapse of numerical simulation at R = 400 mm, $[m]$

As we observe from the results; the permanent deflection of the plate agrees very well with the experimental data, especially for standoff distances at 400 mm and 450mm.

To further validate the DPM, the accumulated blast impulse transferred from the particles to the steel plate is extracted from the numerical simulations. It is important to note that the accumulated impulse that is recorded in IMPETUS is in units Ns and not Pas as one would have grown accustomed to in blast physics. The impulse is divided by the exposed area and differentiated with respect to t to obtain the reflected pressure-time plots.

$$\frac{di}{dt} = P_r(t) \tag{7.11}$$

It is important to note that this pressure is an average over the whole exposed area, and when the plate deforms the exposed area changes. Because of this, the impulse is normally reported in units Ns.

The blast impulse time history and the pressure time history can be seen in figure 7.51 and are summarized in table 7.18.

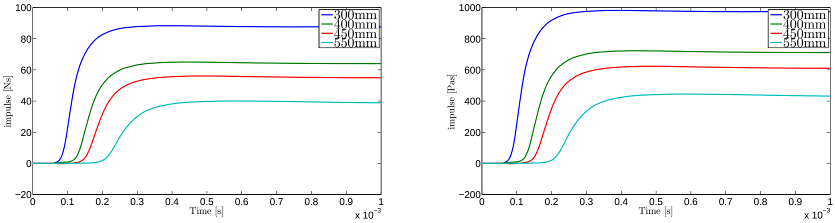

(a) Accumulated impulse $[Ns]$ **(b)** Accumulated impulse $[Pas]$

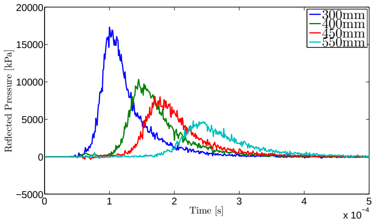

(c) Reflected pressure $[P_r]$

Figure 7.51: Impulse- and pressure-time history in IMPETUS

Table 7.18: Impetus impulse and reflected pressure standoff comparison

R $[mm]$	Peak impulse $[Ns]$*	Peak reflected pressure. P_r $[kPa]$**	Reflected impulse $[Pas]$*
300	88.34	16500.00	982.00
400	65.05	9500.00	722.00
450	56.09	7400.00	620.00
550	40.06	4500.00	445.00

*Because the impulse is deviated from discrete particle collisions and, the peak reflected pressure will be somewhat affected by the interval in which the data are written to the output file. The data should be viewed as approximate.

** The peak pressures are read as approximate values from a central moving average curve with 5 intervals.

The load data extracted from IMPETUS generates results which lies in the proximity of the loads calculated with the UEL. This further validates the simulations carried out with the DPM.

Chapter 8

Comparison and Discussion of Numerical Results

This chapter will sum up and compare the different numerical techniques employed to simulate the experiments at Raufoss in 2010. Figure 8.1 compares the permanent midpoint deflections of the different simulations, and the corresponding results are summarized in table 8.1 and figure 8.1. The most accurate prediction of deflection for each numerical method was chosen for comparison.

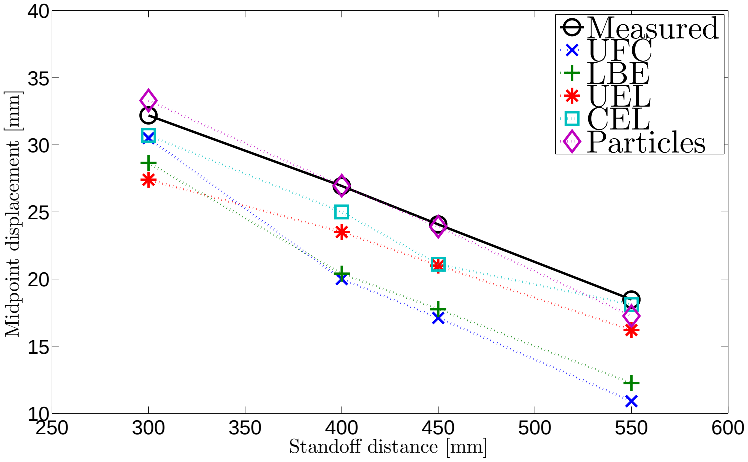

Figure 8.1: Plot of all methods combined

Table 8.1: Complete displacement comparison

Analysis	R $[mm]$	Δ_{perm} $[mm]$	$\frac{\Delta_{perm}}{\Delta_{exp}} \cdot 100\%$	CPU time [h:min:s]*
UFC	300	30.50	94.75 %	[00:10:45]
	400	20.00	74.27 %	[00:11:41]
	450	17.10	71.04 %	[00:10:33]
	550	10.90	59.01 %	[00:07:02]
LBE	300	28.65	89.00 %	[00:13:04]
	400	20.40	75.75 %	[00:13:53]
	450	17.75	73.74 %	[00:13:33]
	550	12.25	66.32 %	[00:08:52]
UEL	300	27.40	85.12 %	[00:58:41]
	400	23.50	87.26 %	[01:31:42]
	450	21.00	87.25 %	[01:44:27]
	550	16.20	87.71 %	[01:43:13]
CEL	300	30.70	95.37 %	[05:35:24]**
	400	25.00	92.83 %	[05:36:20]**
	450	21.10	87.66 %	[05:41:59]**
	550	18.10	97.99 %	[02:45:20]***
Particle	300	33.30	103.45 %	[02:59:55]
	400	26.95	100.07 %	[03:08:13]
	450	23.90	99.27 %	[03:09:28]
	550	17.25	93.39 %	[03:13:58]

*As the analyses in LS-DYNA were performed on a different system than the particle blast simulations in IMPETUS, these CPU times should only be taken as general outlines.

**These analyses were performed on VILJE (16 MPP processors) with a simulation time of 3 ms in contrast to the other analyses at 15 ms.

***This analysis was performed on VILJE (32 MPP processors) with a simulation time of 3 ms in contrast to the other analyses at 15 ms.

While some of the simulations agreed well with experimental results, they are expected to change if friction is chosen to be included in the models. The air-steel friction coefficient is believed to have a negligible effect on the final deflection, but an introduction of a steel-steel friction coefficient is expected to change the results slightly. Structural damping effects are also present in the experiments, but the lack of parameters to properly describe this effect led us to not include this in the simulations. Experimental uncertainties such as errors in the horizontal and vertical alignment of the charge, geometric errors in the components and errors in the charge initiation point are also present. It was chosen not to include the effects of a non-symmetric initiation point and errors in the vertical and horizontal alignment because it would have prevented us from employing quarter symmetry that would in turn drastically increase the computational effort. Small errors might stem from not properly describing the material behaviour, but the extensive work done by Gruben [26] leads us to believe that this error is negligible for small deformations such as this.

Lagrange (UFC and LBE)

Both of the Lagrangian approaches underestimated the blast load, and consequently the resulting deformation. This is mainly believed to stem from the lack of describing FSI effects and a failure to properly describe the charge geometry, thus misrepresenting the blast load parameters. [55] and [29] outlines that an incorrect description of the shape of the explosive agent results in a poor description of the blast load which consequently leads to a failure in describing wanted component behaviour. This is further confirmed by a study in [22] that concludes that the peak pressure and impulse is increased for cylindrically shaped charges. The method of applying the pressure load at discrete zones of tributary area was shown to not be the cause of the inaccuracies.

Uncoupled Euler-Lagrange

The UEL simulations proved to be better than the pure Lagrange simulations, especially when the standoff is increased. The charge geometry was accurately represented and this lead to an increased correlation with experimental data. The blast load obtained by performing the initial calibration of the numerical model underlines the challenges encountered when full scale experiments are performed. This is noticeable as the experiments seems to consistently report underestimated values of the blast load. A drop in accuracy compared to the other methods is observed when the standoff decreases. This is mainly believed to originate in a lack of FSI effects as the plates at low standoffs deform extensively more than the plates further out. The 2D to 3D mapping technique greatly increased the accuracies of the numerical simulations, as the initial detonation and expansion phase proved to be highly mesh sensitive. Additionally by employing this technique, the total model size was reduced while retaining a sufficient level of accuracy, which is supported by the results in [55].

Coupled Euler-Lagrange

The CEL approach further increased the accuracy of the numerical simulations compared to the UEL technique. The gain in accuracy was especially evident for low standoffs as the relatively large deformation of the steel plate was taken in to account. The inclusion of FSI effects was initially thought to only have a small impact on the macroscopic deformation and behaviour of the plate, supported by [45]. A positive effect have been observed for all the CEL simulations compared to the UEL approach. However, despite the increased accuracy the main cause behind a failure to successfully recreate expected deformation is suspected to be a crude discretization of the Eulerian mesh close to the explosive agent. The deflections in table 8.1 are for a full 3D model, as these had the lowest error compared to experimental data. When the 2D to 3D mapping technique was employed with a CEL technique, the simulations overestimated the deflections for all standoffs, indicating that the mesh around the charge was not sufficiently discretized (see results in section 7.3.4). At the largest standoff, the CEL approach achieved the best accuracy of all the methods. This indicates a trend where the CEL would be preferred over a DPM as the Z increase. The experienced numerical instabilities and non-physical disturbance of airflow are also observed in [20].

The Discrete Particle Method

The DPM generally proved to be the most accurate of all the simulation techniques. A drop in accuracy is noticed when the standoff increases, as an increased amount of particles have to be employed for large standoff distances. As outlined by [14] the discrete particle approach have the potential to become a very useful tool for simulating close-range blast effects on structures.

It is evident from all the simulations that the big hurdle in successfully simulating the expected deformation is to accurately describe the load conditions. This is especially evident in the Lagrangian analysis as these failed to properly describe the charge geometry, and consequently the expected blast load parameters were misrepresented. This shows that only relying on CONWEP to define the blast load parameters is a dangerous practice. The deformation of the plates compared to the simulated results with the DPM are illustrated in figures 8.2 to 8.5.

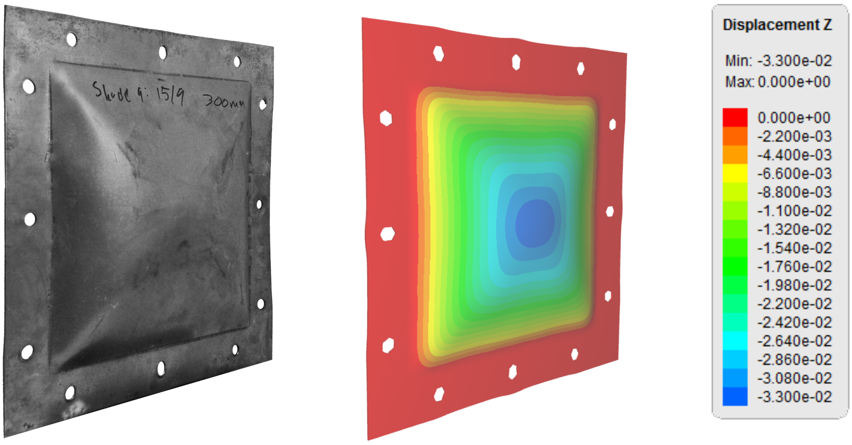

(a) Experiment **(b)** Simulation **(c)** $[m]$

Figure 8.2: R = 300 mm

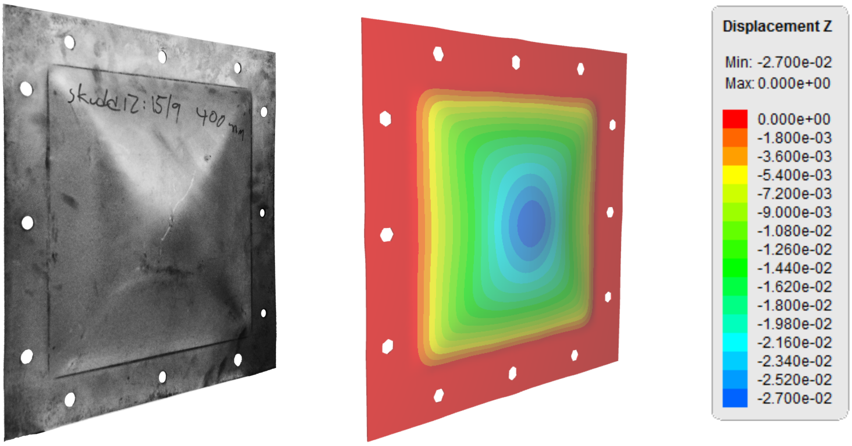

(a) Experiment **(b)** Simulation **(c)** $[m]$

Figure 8.3: R = 400 mm

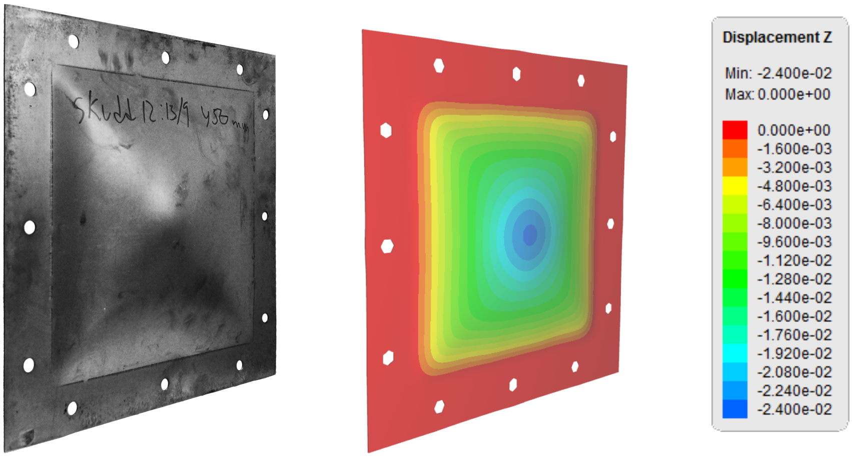

(a) Experiment **(b)** Simulation **(c)** $[m]$

Figure 8.4: R = 450 mm

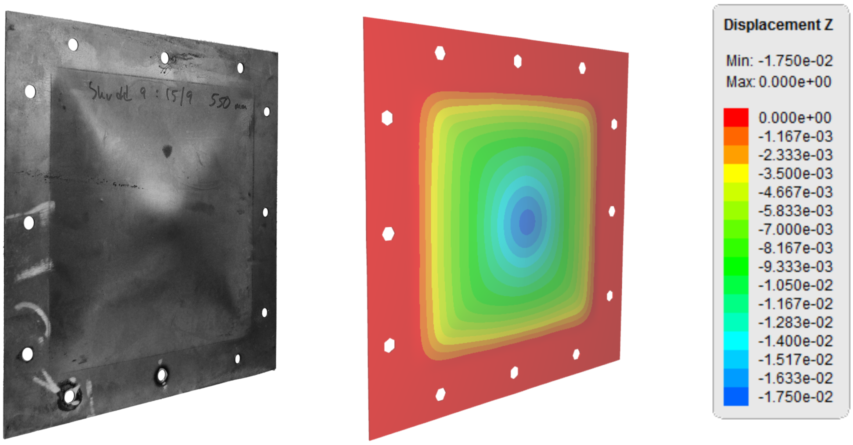

(a) Experiment **(b)** Simulation **(c)** $[m]$

Figure 8.5: R = 550 mm

Remarks Regarding Computational Time

The computational time between the different analyses spanned from minutes to several days. It is important to take this in to account when a simulation technique is to be chosen. This thesis reported the computational time for all the analyses that were run, but the analyses were often run on completely different systems and under different circumstances thus rendering a direct comparison impossible.

Remarks Regarding User Friendliness

It became apparent that defining a feasible numerical model was increasingly hard for the more advanced approaches, the exception being the DPM implemented in IMPETUS. The vast amount of numerical parameters required in LS-DYNA to properly define the CEL simulations was together with the unfamiliarity that structural engineers have with Eulerian FEA the biggest challenges encountered in this thesis. In contrast, the DPM method was so effortlessly defined because of the general purpose of the IMPETUS software. One of the goals of the IMPETUS AFEA software is to minimize the non-physical numerical parameters that have to be tuned in the definition of a numerical model [43], thus together with being the easiest software to employ, it was the most accurate for this particular problem.

Chapter 9

Concluding Remarks

Numerical simulations of several blast-like scenarios have been performed in this thesis; simulations of the gas gun at NTNU, simulations of a ground placed explosive charge and simulations of blast loaded Docol 600 DL steel plates both in the gas gun and with explosives. In the gas gun experiments, the pressure data from performed experiments served as validations, while the permanent midpoint deflection served as the benchmark for the blast loaded plates. In addition to these comparisons, the computational time for the different techniques was outlined to illustrate some of the difficulties engineers have to combat when utilizing different finite element methods.

The experiments involving the gas gun at NTNU proved to be hard to simulate because of the complex geometry of the gas gun itself and the addition of a funnel that disturbed the airflow extensively. Focus was therefore shifted on to simulating experiments performed by Rakvåg at Raufoss in 2010. Experiments of the ground placed charge proved to be difficult to validate because the numerical simulations consistently overestimated both the peak pressure and the impulse. This is probably a result of many combining factors, but the largest contributor is most likely a failure in properly describing the gas dynamics in the simulations and properly measuring the side on pressure in the experiment. Deviations in the experimental setup such as a slight variation in the charge geometry and the spatial placement of the charge are also likely to cause some of errors in the numerical analyses.

Numerical simulations of the experiments with the blast loaded Docol 600 DL steel plates from Raufoss was performed with a pure Lagrangian approach, an uncoupled Lagrangian-Eulerian approach, a coupled Lagrangian-Eulerian formulation and a discrete particle method. All of the numerical techniques were performed at four different standoffs in the experiment, and almost all of the simulations presented non-conservative results. The pure Lagrangian approach was the least accurate because of an inability to properly describe the geometry of the charge, and consequently misrepresenting the blast load. The uncoupled simulations properly described the blast load, but the lack of fluid-structure interaction effects and a crude discretization of the Eulerian mesh near the explosive agent are expected to be the main source of error. To isolate the main source of the discrepancy, a 2D to 3D mapping technique was employed and it was successfully concluded that a sufficiently fine discretization of the Eulerian mesh around the explosive agent yielded a larger blast load and consequently increased expected deformation. Coupled Eulerian-Lagrangian simulations were performed and the inclusion of fluid-structure interaction had positive results in regards of correlation between numerical and experimental results. The computational demand of the coupled calculations was successfully reduced by introducing a mapping of the 2D Eulerian solutions from the uncoupled simulations in to the coupled domain. A sufficiently discretized Eulerian mesh near the charge and the inclusion of FSI effects resulted in conservative results regarding plate deflection. The discrete particle method was the most accurate of all the methods, while being very easy to define numerically. A proper description of the charge geometry and fluid-structure interaction effects combined in a purely Lagrangian domain resulted in good experimental-numerical correlation together with an efficient computational time.

Several different numerical techniques were utilized to simulate the deformation of blast loaded steel plates at four different standoffs. A discrete particle method proved as the most accurate while being the easiest to define numerically. Results in this thesis indicate that the main culprit in the inability to recreate expected deformations lies in a failure to properly describe the load conditions. It shows that it is a dangerous practice to rely solemnly on standards such as CONWEP or the UFC to describe the blast load parameters.

Chapter 10

Further Work

The advancements made within computer-aided engineering has created an abundance of methods and techniques of simulating blast loading. The intention behind writing this thesis was to create an overview of methods presently used to simulate blast loading, and showcase each methods strengths and weaknesses.

The experiments used as benchmarks in this thesis are relatively simple, so the numerical methods presented in this paper have not been utilized to their full potential. Therefore the following studies could be subject for further work:

- Use the numerical model created in section 7.2.2 in order to optimize the gas cannon experiment with respect to both penetration studies and using air-pressure to emulate blast loading.
- Investigate the various methods of reducing the computational expense while retaining accuracy for MME analyses in LS-DYNA, such as mesh biasing, element erosion, mapping from 1D or 2D to 3D.
- Further explore the causes behind the observed numerical instabilities.
- Perform more full scale experiments with explosives to gather more blast load data, thus further increase the foundation in which the numerical simulations can be validated against.
- Investigate how different charge geometries affect the blast load parameters.
- Employ the particle based approach to see how it performs for more complex blast scenarios.
- Investigate how the introduction of a steel-steel friction coefficient and structural damping affect the component response.
- Explore the method of combined empirical loading with a reduced ALE domain.

Bibliography

[1] J. B. Aarseth. Numeriske beregningsmetoder - numerical computational methods. *Department of Structural Engineering - Norwegian University of Science and Technology*, page 186, 2011.

[2] A. Alia and M. Souli. High explosive simulation using multi-material formulations. *Applied Thermal Engineering*, 26(10):1032–1042, 2006.

[3] N. Aquelet and M. Souli. 2d to 3d ale mapping, 10th international ls-dyna users conference (fluid/structure), 2008.

[4] W. E. Baker. *Explosions in air.* Wilfred Baker Engineering, San Antonio, 1983.

[5] W. E. Baker. *Explosion hazards and evaluation.* Elsevier, Amsterdam, 1983.

[6] Y. Bao and T. Wierzbicki. On fracture locus in the equivalent strain and stress triaxiality space. *International Journal of Mechanical Sciences*, 46 (1):81–98, 2004.

[7] T. Belytschko, W. K. Liu, and B. Moran. *Nonlinear finite elements for continua and structures.* Wiley, Chichester, 2000.

[8] D. Bernoulli. Hydrodynamica sive de viribus et motibus fluidorum commentarii. *Reinholdi Dulseckeri, Argentorati*, Strasbourg: Joh., 1738.

[9] D. Bernoulli and J. Bernoulli. Hydrodynamics. *Dover Publications*, 1968.

[10] D. Bjerketvedt, J. R. Bakke, and K. Van Wingerden. Gas explosion handbook. *Journal of Hazardous Materials*, 52(1):1–150, 1997.

[11] T. Børvik, M. Langseth, and K. A. Malo. A compressed gas gun for impact testing. 1997.

[12] T. Børvik, O. S. Hopperstad, T. Berstad, and M. Langseth. A computational model of viscoplasticity and ductile damage for impact and penetration. *European Journal of Mechanics - A/Solids*, 20(5):685–712, 2001.

[13] T. Børvik, A. G. Hanssen, M. Langseth, and L. Olovsson. Response of structures to planar blast loads – a finite element engineering approach. *Computers and Structures*, 87(9–10):507–520, 2009.

[14] T. Børvik, L. Olovsson, A. G. Hanssen, K. P. Dharmasena, H. Hansson, and H. N. G. Wadley. A discrete particle approach to simulate the combined effect of blast and sand impact loading of steel plates. *Journal of the Mechanics and Physics of Solids*, 59(5):940–958, 2011.

[15] G. T. Camacho and M. Ortiz. Adaptive lagrangian modelling of ballistic penetration of metallic targets. *Computer Methods in Applied Mechanics and Engineering*, 142(3–4):269–301, 1997.

[16] M. S. Chafi, G. Karami, and M. Ziejewski. Numerical analysis of blast-induced wave propagation using fsi and alemulti-material formulations. *International Journal of Impact Engineering*, 36(10–11):1269–1275, 2009.

[17] N. L. Coleburn. Chapman-jouget pressures of several pure and mixed explosives. *United States Naval Ordnance Laboratory*, 64-58, 1964.

[18] R. D. Cook. *Concepts and applications of finite element analysis.* Wiley, New York, 2002.

[19] S. Curtze, V. T. Kuokkala, M. Hokka, and P. Peura. Deformation behavior of trip and dp steels in tension at different temperatures over a wide range of strain rates. *Materials Science and Engineering: A*, 507(1–2):124–131, 2009.

[20] A. Dacko and J. Toczyski. Vulnerability analysis of aircraft fuselage subjected to internal explosion. *Archive of Mechanical Engineering*, 58(4): 393–406, 2011.

[21] J. M. Dewey. The rankine-hugoniot equations: Their extensions and inversions related to blast waves. *Dewey McMillin and Associates Ltd*, pages 1–15, 2006.

[22] H. S. Eide and E. A. Melby. *Blast Loaded Aluminium Plates - Experiments and Numerical Simulations.* Master's thesis, Norwegian University of Science and Technology, 2013.

[23] U.S. Army Corps of Engineers, Naval Facilities Engineering Command (Preparing Activity), and Air Force Civil Engineering Support Agency. Unified facilities criteria (ufc) structures to resist the effects of accidental explosions. UFC 3-340-02, 2008.

[24] Livermore Software Technology Corporation (LSTC) Inc Gmbh and Dynamore. Ls-dyna examples, . URL `http://www.dynaexamples.com/`. [03.02.2013].

[25] Livermore Software Technology Corporation (LSTC) Inc Gmbh and Dynamore. Ls-dyna support, . URL `http://www.dynasupport.com/`. [03.02.2013].

[26] G. Gruben. Ductile fracture in dual-phase steel; theoretical, experimental and numerical study. *Norwegian University of Science and Technology, Department of Structural Engineering*, 2012.

[27] S. Hallset and J. S. Haagenrud. *Combined blast and fragment loading on plates.* Master's thesis, Norwegian University of Science and Technology, 2011.

[28] A. Hirth, A. Haufe, and L. Olovsson. Airbag simulation with ls-dyna. past-present-future. *6th European LS-DYNA Users' Conference. Keynote 6*, 2007.

[29] C. Knock and N. Davies. Blast waves from cylindrical charges. *Shock Waves*, pages 1–7, 2013.

[30] A. F. Liu. *Mechanics and mechanisms of fracture: an introduction.* ASM International, Materials Park, Ohio, 2005.

[31] P. M. Locking. The trouble with tnt equivalence. *26th International ballistics symposium, paper 11770*, 2011.

[32] Livermore Software Technology Corporation (LSTC). Ls-dyna theory manual. 2006.

[33] Livermore Software Technology Corporation (LSTC). Ls-dyna keyword user's manual - volume i [version: 971 r6.1.0]. 2012.

[34] Livermore Software Technology Corporation (LSTC). Ls-dyna keyword user's manual - volume ii: Material models [version: 971 r6.1.0]. 2012.

[35] K. M. Mathisen. Lecture 7: Solution of the dynamic equilibrium equations by explicit direct integration. *Lecture Notes in TKT4197 - Nonlinear Finite Element Analysis*, pages 1–19, 2012.

[36] K. M. Mathisen. Lecture 9: Solution of the nonlinear dynamic equilibrium equations. *Lecture Notes in TKT4197 - Nonlinear Finite Element Analysis*, pages 1–8, 2012.

[37] J. C. Maxwell. Illustrations of the dynamical theory of gases. *Philosophical Magazine*, 19:19–32, 1860.

[38] W. Nian, K. Subramaniam, and Y. Andreopoulos. Response of an elastic structure subject to air shock considering fluid-structure interaction. *Journal of Aerospace Engineering*, 23(3):176–185, 2009.

[39] G. N. Nurick and G. C. Shave. The deformation and tearing of thin square plates subjected to impulsive loads—an experimental study. *International Journal of Impact Engineering*, 18(1):99–116, 1996.

[40] L. Olovsson. Ls-dyna - training class in ale and fluid-structure interaction. *LSTC*, 2004.

[41] L. Olovsson. Corpuscular method for airbag deployment simulations in ls-dyna. *Impetus Afea Technical Publications*, page 80, 2007.

[42] L. Olovsson, A. G. Hanssen, T. Børvik, and M. Langseth. A particle-based approach to close-range blast loading. *European Journal of Mechanics - A/Solids*, 29(1):1–6, 2010.

[43] L. Olovsson, Vistnes H., and A. G. Hanssen. Introduction course to the impetus afea solver. 2013.

[44] K. G. Rakvåg. *Combined blast and fragment loading on plates*. Master's thesis, Norwegian University of Science and Technology, 2009.

[45] K. G. Rakvåg, N. J. Underwood, G. K. Schleyer, T. Børvik, and O. S. Hopperstad. Transient pressure loading of clamped metallic plates with pre-formed holes. *International Journal of Impact Engineering*, 53(0):44–55, 2013.

[46] L. Schwer. Personal correspondance via unofficial ls-dyna user group forum. URL `http://tech.groups.yahoo.com/group/LS-DYNA/`. [10.03.2013].

[47] Swedish steel AB SSAB. Docol dp/dl cold reduced dual phase steels. URL `http://www.ssab.com/Global/DOCOL/datasheets_docol/en/201_Docol%20DP%20DL.pdf`. [04.02.2013].

[48] L. Stewart. Airblast environment. *Lecture Notes in SE207 Introduction to Blast Loading and Design. Department of Structural Engineering. University of California, San Diego*, pages 1–6, 2012.

[49] L. Stewart. Blast forces acting on structures. *Lecture Notes in SE207 Introduction to Blast Loading and Design. Department of Structural Engineering. University of California, San Diego*, pages 1–18, 2012.

[50] L. Stewart. Blast waves. *Lecture Notes in SE207 Introduction to Blast Loading and Design. Department of Structural Engineering. University of California, San Diego*, pages 1–12, 2012.

[51] L. Stewart. Explosive threats. *Lecture Notes in SE207 Introduction to Blast Loading and Design. Department of Structural Engineering. University of California, San Diego*, pages 1–13, 2012.

[52] K. V. Subramaniam, W. Nian, and Y. Andreopoulos. Blast response simulation of an elastic structure: Evaluation of the fluid–structure interaction effect. *International Journal of Impact Engineering*, 36(7):965–974, 2009.

[53] V. Tarigopula, M. Langseth, O. S. Hopperstad, and A. H. Clausen. Axial crushing of thin-walled high-strength steel sections. *International Journal of Impact Engineering*, 32(5):847–882, 2006.

[54] R. G. Teeling-Smith and G. N. Nurick. The deformation and tearing of thin circular plates subjected to impulsive loads. *International Journal of Impact Engineering*, 11(1):77–91, 1991.

[55] B. Zakrisson, B. Wikman, and H. Å. Häggblad. Numerical simulations of blast loads and structural deformation from near-field explosions in air. *International Journal of Impact Engineering*, 38(7):597–612, 2011.

Appendix A

Experimental Results (Ch. 5)

A.1 NTNU Pressure History (Section 5.1.1)

In the following graphs only results from pressure transducer in position 1 are shown. Both raw data and filtered results are shown.

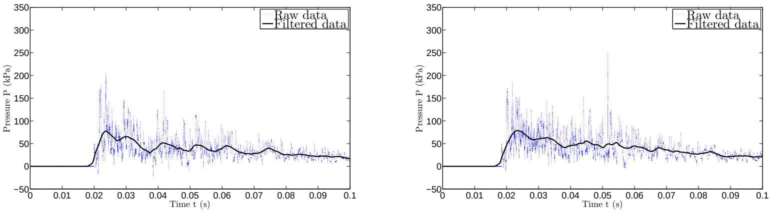

(a) 5 Bar pressure test 2 **(b)** 5 Bar pressure test 4

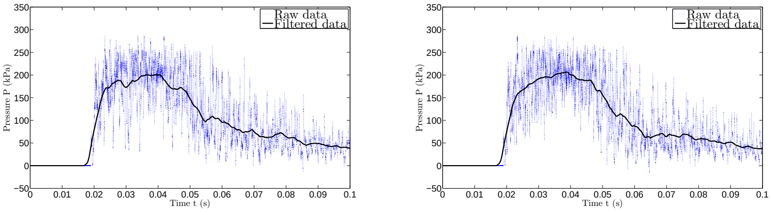

(c) 10 Bar pressure test 1 **(d)** 10 Bar pressure test 2

Figure A.1: Pressure Histories 5-30 Bar test 1

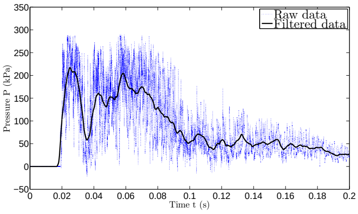

(e) 15 Bar pressure test 1

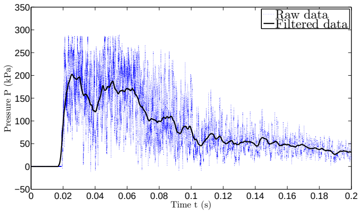

(f) 15 Bar pressure test 2

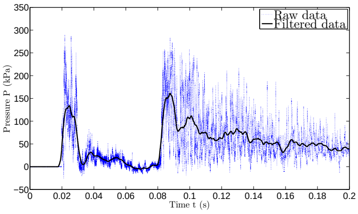

(g) 20 Bar pressure test 1

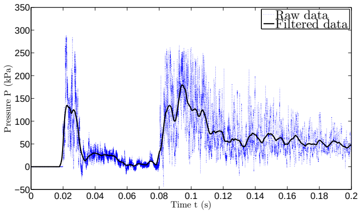

(h) 20 Bar pressure test 2

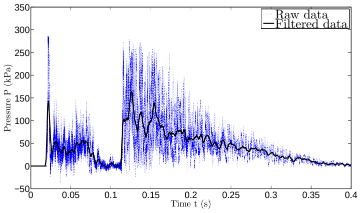

(i) 30 Bar pressure test 1

Notice that peak pressures does not increase for 10 bar and up. However the impulse increases as expected. In order to investigate the effect of using only main chamber or just the small chamber an additional 4 tests were performed

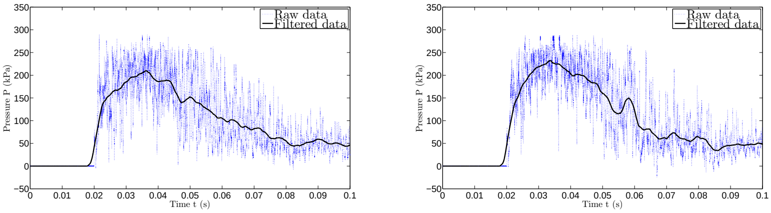

(a) 10 Bar in main tank only test 1 **(b)** 10 Bar in main tank only test 2

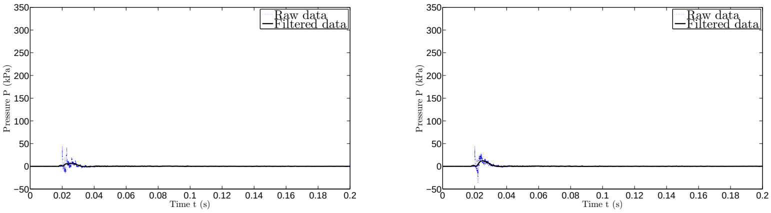

(c) 10 Bar in small tank only test 2 **(d)** 10 Bar in small tank only test 3

Figure A.2: Pressure history 10 bar in main and small tank only

The experiments performed using the small tank only proved to be of small value. Apparently the volume of air in the small chamber is not enough to propagate with the same amount of speed along the barrel.

A.2 Matlab Script (Section 5.1.1)

```
%
%   Master Thesis "Blast loaded steel plates"
%   By Andersen, Kristoffer H. and Hernandez, Fredrik B.
%
close all
clear all
clc
%
%   Pressure Histories
%
MaxP = 350;                                     % Maximum plotted pressure [kPa]
MinP = -50;                                     % Minimum plotted pressure [kPa]
Maxt = 0.2;                                     % Maximum plotted time-interval [s]
set(0,'defaulttextinterpreter','latex')         % Enable latex fonts
set(0,'DefaultAxesFontSize', 25)                % Set up font size
%
%   Gather data from sensor # 1
%
load 10barsmall002.txt                          % Load raw data
S2(:,1) = X10barsmall002(:,1);                  % Set up time history in vector S2 [s]
S2(:,2) = X10barsmall002(:,2);                  % Set up pressure history in vector S2 [kPa]
%
% Set up Butterworth algorithm
%
cutF = 100;                                     % Cutoff frequency [Hz]
samplR = 500000;                                % Sampling rate [Hz]
cutN = cutF*2/samplR;                           % Normalized cutoff frequency [-]
[b,a]=butter(2,cutN);                           % Initialize Butterworth algorithm
%
% Employ Butterworth algorithm
%
filt=filter(b,a,S2);                            % Use Butterworth on vector S2
%
% Plot
%
h=plot(S2(:,1),S2(:,2),'b:',...                 % Plot both filtered and raw data
    filt(:,1),filt(:,2),'k');
xlabel('Time t (s)');                           % Name x-axis
ylabel('Pressure P (kPa)');                     % Name y-axis
axis([0 Maxt MinP MaxP]);                       % Select axis-range
Leg=legend('Raw data','Filtered data');         % Create legend
set(Leg,'Fontsize',35)                          % Set up legend font size
set(h(1),'linewidth',1.5)                       % Set up custom linewidt for raw data
set(h(2),'linewidth',3)                         % Set up custom linewidt for filtered data
A=trapz(filt(:,1),filt(:,2))                    % Check integrated value of filtered data
B=trapz(S2(:,1),S2(:,2))                        % Check integrated value of raw data

save 10BarS2F.txt -ascii filt                   % Save filtered data vector in ASCII file
```

A.3 Raufoss Side-on Pressure History (Section 5.2.1)

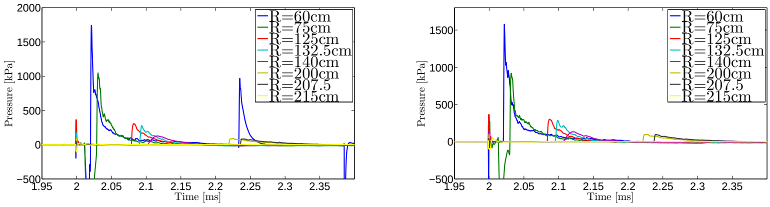

(a) Test 1 **(b)** Test 2

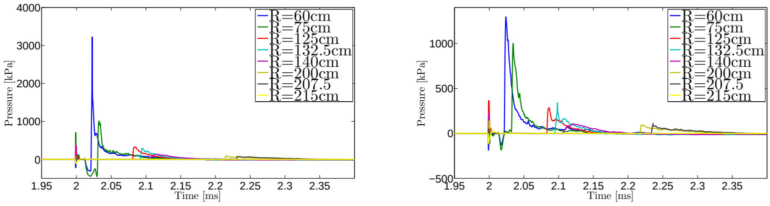

(c) Test 3 **(d)** Test 4

Figure A.2: Side-on pressure histories for test 1-4

Appendix B

Preliminary Numerical Study (Ch. 6)

B.1 LS-DYNA Keyword (Section 6.1.1)

```
*KEYWORD
*INCLUDE
SUPPORTS.k
PLATE_SH_M5_FR.k
CLAMPS.k
*TITLE
$# title
Andersen and Hernandez Master Thesis 2013
$$$$$$$$$$$$$$$$$$$$$$$$$$$$$$$$$$$$$$$$$$$$$$$$$$$$$$$$$$$$$$$$$$$$$$$$$$$$$$$$
$
$ CONTROL SETTINGS
$
$$$$$$$$$$$$$$$$$$$$$$$$$$$$$$$$$$$$$$$$$$$$$$$$$$$$$$$$$$$$$$$$$$$$$$$$$$$$$$$$
*CONTROL_ACCURACY
$#     osu       inn    pidosu
         1         4         0
*CONTROL_ENERGY
$#    hgen      rwen    slnten     rylen
         2         2         1         1
*CONTROL_SHELL
$#  wrpang     esort     irnxx    istupd    theory       bwc     miter      proj
     0.000         0         0         1         2         2         1         0
$# rotascl    intgrd    lamsht    cstyp6    tshell    nfail1    nfail4   psnfail
  1.000000         1         0         1         0         0         0         0
$# psstupd    irquad     cntco    itsflg    irquad
         0         0         0         0         2
*CONTROL_TERMINATION
$#  endtim    endcyc     dtmin    endeng    endmas
  0.05000         0     0.000     0.000     0.000
*CONTROL_TIMESTEP
0,0.5
$$$$$$$$$$$$$$$$$$$$$$$$$$$$$$$$$$$$$$$$$$$$$$$$$$$$$$$$$$$$$$$$$$$$$$$$$$$$$$$$
$
$ OUTPUT PARAMETERS
$
$$$$$$$$$$$$$$$$$$$$$$$$$$$$$$$$$$$$$$$$$$$$$$$$$$$$$$$$$$$$$$$$$$$$$$$$$$$$$$$$
*DATABASE_GLSTAT
$#      dt    binary      lcur     ioopt
 1.0000E-5         0         0         1
*DATABASE_MATSUM
$#      dt    binary      lcur     ioopt
 1.0000E-5         0         0         1
*DATABASE_NODOUT
```

```
$#      dt    binary      lcur     ioopt      dthf     binhf
 1.0000E-5         0         0         1     0.000         0
*DATABASE_BINARY_D3PLOT
$#      dt      lcdt      beam     npltc    psetid
 0.0100000         0         0         0         0
$#   ioopt
         0
*DATABASE_HISTORY_NODE
$#     id1       id2       id3       id4       id5       id6       id7       id8
      6560      6579      6599         0         0         0         0         0
$$$$$$$$$$$$$$$$$$$$$$$$$$$$$$$$$$$$$$$$$$$$$$$$$$$$$$$$$$$$$$$$$$$$$$$$$$$$$$$$
$
$ SECTION PROPERTIES
$
$$$$$$$$$$$$$$$$$$$$$$$$$$$$$$$$$$$$$$$$$$$$$$$$$$$$$$$$$$$$$$$$$$$$$$$$$$$$$$$$
*SECTION_SHELL_TITLE
PLATE
$#   secid    elform      shrf       nip     propt   qr/irid     icomp     setyp
         1         2  1.000000         5         1         0         0         1
$#      t1        t2        t3        t4      nloc     marea      idof    edgset
 7.0000E-4 7.0000E-4 7.0000E-4 7.0000E-4     0.000     0.000     0.000         0
*SECTION_SOLID_TITLE
SOLIDS
$#   secid    elform       aet
         2         1         0
$$$$$$$$$$$$$$$$$$$$$$$$$$$$$$$$$$$$$$$$$$$$$$$$$$$$$$$$$$$$$$$$$$$$$$$$$$$$$$$$
$
$ MATERIAL PROPERTIES
$
$$$$$$$$$$$$$$$$$$$$$$$$$$$$$$$$$$$$$$$$$$$$$$$$$$$$$$$$$$$$$$$$$$$$$$$$$$$$$$$$
*MAT_MODIFIED_JOHNSON_COOK_TITLE
STEEL DOCOL 600DL
$#     mid        ro         e        pr      beta       xsi        cp     alpha
         1 7850.00002.1000E+11  0.330000     0.000  0.900000 452.00000 1.2000E-5
$#   e0dot        tr        tm        t0     flag1     flag2
  1.000E-3 293.00000 1800.0000 293.00000     0.000  1.000000
$#  a/siga       b/b   n/beta0   c/beta1      m/na
 2.8330E+8         0  0.000000  0.005000  1.000000
$#    q1/a      c1/n q2/alpha0 c2/alpha1
 2.6830E+8    39.380 3.9660e+8     5.000
$#   dc/dc     pd/wc     d1/na     d2/na     d3/na     d4/na     d5/na
  1.000000   7.48E+8     0.000     0.000     0.000     0.000     0.000
$#      tc      tauc
 1650.00001.0000E+20
*MAT_RIGID_TITLE
Steel
$#     mid        ro         e        pr         n    couple         m     alias
         5 7850.00002.1000E+11  0.330000     0.000     0.000     0.000
$#     cmo      con1      con2
  1.000000         7         7
$# lco or a1       a2        a3        v1        v2        v3
     0.000     0.000     0.000     0.000     0.000     0.000
$$$$$$$$$$$$$$$$$$$$$$$$$$$$$$$$$$$$$$$$$$$$$$$$$$$$$$$$$$$$$$$$$$$$$$$$$$$$$$$$
$
$ LOAD PROPERTIES
$
$$$$$$$$$$$$$$$$$$$$$$$$$$$$$$$$$$$$$$$$$$$$$$$$$$$$$$$$$$$$$$$$$$$$$$$$$$$$$$$$
*DEFINE_CURVE_FUNCTION_TITLE
```

```
LOAD_CURVE
$#    lcid      sidr       sfa       sfo      offa      offo    dattyp
        10         0  1.000000  1.000000     0.000     0.000         0
$# function
300000.*(1-time/0.02)*exp(-2*time/0.02)
*LOAD_SEGMENT_SET_ID
$#      id                                                                 heading
         1Load
$#    ssid      lcid        sf        at        dt
        47        10  1.000000     0.000     0.000
$$$$$$$$$$$$$$$$$$$$$$$$$$$$$$$$$$$$$$$$$$$$$$$$$$$$$$$$$$$$$$$$$$$$$$$$$$$$$$$$
$
$ CONTACT PROPERTIES
$
$$$$$$$$$$$$$$$$$$$$$$$$$$$$$$$$$$$$$$$$$$$$$$$$$$$$$$$$$$$$$$$$$$$$$$$$$$$$$$$$
*CONTACT_AUTOMATIC_SURFACE_TO_SURFACE
$#     cid                                                                 title
$#    ssid      msid     sstyp     mstyp    sboxid    mboxid       spr       mpr
         2        46         3         2         0         0         0         0
$#      fs        fd        dc        vc       vdc    penchk        bt        dt
     0.000     0.000     0.000     0.000     0.000         0     0.0001.0000E+20
$#     sfs       sfm       sst       mst      sfst      sfmt       fsf       vsf
  1.000000  1.000000     0.000     0.000  1.000000  1.000000  1.000000  1.000000
$$$$$$$$$$$$$$$$$$$$$$$$$$$$$$$$$$$$$$$$$$$$$$$$$$$$$$$$$$$$$$$$$$$$$$$$$$$$$$$$
$
$ SEGMENTS AND SETS
$
$$$$$$$$$$$$$$$$$$$$$$$$$$$$$$$$$$$$$$$$$$$$$$$$$$$$$$$$$$$$$$$$$$$$$$$$$$$$$$$$
*SET_PART_LIST_TITLE
Contact_Supports_and_Clamps
$#     sid       da1       da2       da3       da4    solver
        46     0.000     0.000     0.000     0.000MECH
$#    pid1      pid2      pid3      pid4      pid5      pid6      pid7      pid8
         4         6         0         0         0         0         0         0
*SET_SEGMENT_GENERAL_TITLE
contact_slave_segment
$#     sid       da1       da2       da3       da4    solver
         2     0.000     0.000     0.000     0.000MECH
$# option        e1        e2        e3        e4        e5        e6        e7
PART               2         0         0         0         0         0         0
*SET_SEGMENT_GENERAL_TITLE
contact_master_segment
$#     sid       da1       da2       da3       da4    solver
        46     0.000     0.000     0.000     0.000MECH
$# option        e1        e2        e3        e4        e5        e6        e7
PART               4         6         0         0         0         0         0
$$$$$$$$$$$$$$$$$$$$$$$$$$$$$$$$$$$$$$$$$$$$$$$$$$$$$$$$$$$$$$$$$$$$$$$$$$$$$$$$
$
$ PART DESCRIPTION
$
$$$$$$$$$$$$$$$$$$$$$$$$$$$$$$$$$$$$$$$$$$$$$$$$$$$$$$$$$$$$$$$$$$$$$$$$$$$$$$$$
*PART
$# title
Plate
$#     pid     secid       mid     eosid      hgid      grav    adpopt      tmid
         2         1         1         0         0         0         0         0
*PART
$# title
```

```
Supports
$#     pid     secid       mid     eosid      hgid      grav    adpopt      tmid
         4         2         5         0         0         0         0         0
*PART
$# title
Clamps
$#     pid     secid       mid     eosid      hgid      grav    adpopt      tmid
         6         2         5         0         0         0         0         0
$$$$$$$$$$$$$$$$$$$$$$$$$$$$$$$$$$$$$$$$$$$$$$$$$$$$$$$$$$$$$$$$$$$$$$$$$$$$$$$$
$
$    BOUNDARY CONDITIONS
$
$$$$$$$$$$$$$$$$$$$$$$$$$$$$$$$$$$$$$$$$$$$$$$$$$$$$$$$$$$$$$$$$$$$$$$$$$$$$$$$$
*BOUNDARY_SPC_SET_ID
$#      id                                                               heading
         0BC_FIXED
$#    nsid       cid      dofx      dofy      dofz     dofrx     dofry     dofrz
        30         0         1         1         1         1         1         1
*SET_NODE_GENERAL_TITLE
Fixed_Supports_Clamps
$#     sid       da1       da2       da3       da4    solver
        30     0.000     0.000     0.000     0.000MECH
$# option         e1        e2        e3        e4        e5        e6        e7
PART               4         6         0         0         0         0         0
*END
```

B.2 LS-DYNA Keyword (Section 6.2)

The parameter choices are commented on in table B.1. The parameters not shown, are not tampered with, and left to the default values.

Table B.1: Parameters used in LS-DYNA comments

Card	Parameter	Comment
*CONTROL_ALE	dct = -1	Recommended by [33]. See B.2.1.1
	meth = -2	Recommended by [33]. See B.2.1.2
	prit = 1	Recommended by [33]. See B.2.1.3
	pref = 1E5	Assumed 1 bar atmospheric pressure
	checkr = 0.1	Recommended by [33]. See B.2.1.4

B.2.1.1 CONTROL_ALE Remark 9 in [33]

DCT is an obsolete (unused) flag in pre-R5 releases of 971 but can be used starting with the R5 release to invoke an alternate advection scheme. DCT=-1 is recommended over the default scheme, especially for simulating explosives and includes the following major changes:
(a) Relaxes an artificial limit on the expansion ratio limit. The default limit improves stability in some situations but can overestimate the explosive impulse.
(b) Corrects redundant out-flux of material at corner elements. The redundancy can lead to negative volume.
(c) Removes several artificial constraints in the advection which were originally implemented to assist in stability but are no longer needed.

B.2.1.2 CONTROL_ALE Remark 10 in [33]

The METH=-2 advection type is the same as METH=2 with only one exception. It employs a looser constraint on monotonicity requirement during ALE advection. When METH=2, for each advection process along three directions (front/back, top/bottom, left/right), the maximum/minimum values for advected history variables in the three elements along that direction are capped. METH=-2 relaxed the monotonicity condition so that the advected value is capped at the maximum/minimum value in the element itself and its neighboring 26 elements. This option, in certain conditions, can better preserve the material interface for materials defined with *MAT_HIGH_EXPLOSIVE_BURN.

B.2.1.3 CONTROL_ALE Remark 1 in [33]

By default, all materials in a multi-material element are assumed to undergo the same element averaged strain rates. This assumption may not be robust when mixing materials with very different compressibility. In this case, an assumption of pressure equilibrium (PRIT=1) in the element may be more appropriate.

B.2.1.4 CONTROL_ALE Remark 4 in [33]

```
Due to one point integration, ALE elements may experience a spatial instability in the
pressure field referred to as checker boarding. CHECKR is a scale for diffusive flux
calculation to alleviate this problem.
```

Appendix C

Numerical Methods (Ch. 7)

C.1 UFC (Section 7.3.1)

The full calculations to estimate the blast load parameters in section 7.3.1 are shown here. The UFC stems from the US military where imperial units still governs such that a conversion to SI units are needed in order to compare with our results.

Table C.1: UFC calculations, unit conversions

R $[mm]$	R $[ft]$	W_{C4} $[kg]$	W_{C4} $[lb]$
300	0.984251969	0.1425	0.31415835
400	1.312335958		
450	1.476377953		
550	1.804461942		

Table C.2: C4 TNT equivalence per standoff

R $[mm]$	Q_{C4} $[ft-lb/lb]$	Q_{TNT} $[ft-lb/lb]$	$\frac{Q_{C4}}{Q_{TNT}}$ [-]*	$W_{EQ,TNT}$ $[lb]$
300	2.22E+06	1.97E+06	1.13E+00	3.54E-01
400				
450				
550				

*As shown in [31] and [50] the TNT equivalence factor for C4 is a function of the scaled distance, typically in the range of 1.2-1.4. The recommended value in the UFC underestimate the TNT-equivalent weight.

Table C.3: Scaled distance per standoff

R $[mm]$	Z $[\frac{ft}{lbs^{1/3}}]$
300	1.39E+00
400	1.86E+00
450	2.09E+00
550	2.55E+00

With the scaled distance we can find the blast load parameters. As mentioned in section 7.3.1 it is impossible to find a blast load scenario in the UFC that are completely identical to the experiments performed in this thesis. The closest match is to employ the chart in figure 2.9. Here it is assumed that the explosive is placed in free air because the standoff is so small that the waves reflected from the ground will not fuse with the original incident waves before they hit the target plate. The blast wave parameters from the chart are summarized in table C.4.

Table C.4: Friedlander input data based on UFC

R $[mm]$	P_r^+ $[psi]$	i_r^+ $[\frac{psi-ms}{lbs^{1/3}}]$	T^+ $[\frac{ms}{lbs^{1/3}}]$
300	3500	140.1	0.307
400	1660	93.3	0.784
450	1230	79.7	1.152
550	700	61.3	1.382

The data is converted to SI units:

Table C.5: Friedlander input data based on UFC, SI units

Standoff, R $[mm]$	P_r^+ $[kPa]$	i_r^+ $[Pas]$	T^+ $[s]$
300	24131.65	6.83E+02	2.17E-04
400	11445.30	4.55E+02	5.55E-04
450	8480.55	3.89E+02	8.15E-04
550	4826.33	2.99E+02	9.78E-04

Corresponding Friedlander functions are created from the data in table C.5. The decay coefficients are found by integrating the Friedlander function such that:

$$\int_0^{T^+} P_r^+ \left(1-\frac{t}{T^+}\right) e^{\frac{-bt}{T^+}}\, dt = i_r^+ \tag{C.1}$$

Table C.6: Decay coefficients per standoff

R $[mm]$	b [-]
300	6.49
400	12.86
450	16.70
550	14.68

C.2 LS-DYNA Keyword (Section 7.3.2)

```
*KEYWORD 200000000
*INCLUDE
VOLUME.k
*TITLE
$# title
Side-on pressure simulation Raufoss
$$$$$$$$$$$$$$$$$$$$$$$$$$$$$$$$$$$$$$$$$$$$$$$$$$$$$$$$$$$$$$$$$$$$$$$$$$$$$$$$
$
$ CONTROL SETTINGS
$
$$$$$$$$$$$$$$$$$$$$$$$$$$$$$$$$$$$$$$$$$$$$$$$$$$$$$$$$$$$$$$$$$$$$$$$$$$$$$$$$
*CONTROL_ALE
$#     dct      nadv      meth      afac      bfac      cfac      dfac      efac
        -1         1        -2         0     0.000     0.000     0.000     0.000
$#   start       end     aafac     vfact      prit       ebc      pref   nsidebc
     0.000     1.000     0.000     0.000         1         0    1.0e+5         0
$#    ncpl      nbkt    imascl    checkr
         1        50         0     0.100
*CONTROL_TERMINATION
$#  endtim    endcyc     dtmin    endeng    endmas
  0.004000         0     0.000     0.000     0.000
*CONTROL_TIMESTEP
$#  dtinit    tssfac      isdo    tslimt     dt2ms      lctm     erode     ms1st
     1.E-8  0.600000         0     0.000     0.000         0         0         0
$#  dt2msf   dt2mslc     imscl
     0.000         0         0
*CONTROL_ENERGY
$#    hgen      rwen    slnten     rylen
         2         2         2         2
```

```
$$$$$$$$$$$$$$$$$$$$$$$$$$$$$$$$$$$$$$$$$$$$$$$$$$$$$$$$$$$$$$$$$$$$$$$$$$$$$$$$
$
$ OUTPUT PARAMETERS
$
$$$$$$$$$$$$$$$$$$$$$$$$$$$$$$$$$$$$$$$$$$$$$$$$$$$$$$$$$$$$$$$$$$$$$$$$$$$$$$$$
*DATABASE_TRHIST
$#      dt    binary      lcur     ioopt
 1.0000E-7         0         0         1
*DATABASE_GLSTAT
$#      dt    binary      lcur     ioopt
 5.0000E-6         0         0         1
*DATABASE_MATSUM
$#      dt    binary      lcur     ioopt
 5.0000E-6         0         0         1
*DATABASE_BINARY_D3PLOT
$#      dt      lcdt      beam     npltc    psetid
 4.0000E-4         0         0         0         0
$#   ioopt
         0
$
$******** DEFINE FIXED TRACER TRACER POINTS FOR OUTPUT ********
$
*DATABASE_TRACER
$#    time     track         x         y         z      ammg       nid
     0.000         1  0.300000  0.001000  0.000000         0         0
     0.000         1  0.400000  0.001000  0.000000         0         0
     0.000         1  0.450000  0.001000  0.000000         0         0
     0.000         1  0.550000  0.001000  0.000000         0         0
     0.000         1  0.600000  0.001000  0.000000         0         0
     0.000         1  0.750000  0.001000  0.000000         0         0
     0.000         1  1.250000  0.001000  0.000000         0         0
     0.000         1  1.325000  0.001000  0.000000         0         0
     0.000         1  1.400000  0.001000  0.000000         0         0
     0.000         1  2.000000  0.001000  0.000000         0         0
     0.000         1  2.075000  0.001000  0.000000         0         0
     0.000         1  2.150000  0.001000  0.000000         0         0
$$$$$$$$$$$$$$$$$$$$$$$$$$$$$$$$$$$$$$$$$$$$$$$$$$$$$$$$$$$$$$$$$$$$$$$$$$$$$$$
$
$ SECTION PROPERTIES
$
$$$$$$$$$$$$$$$$$$$$$$$$$$$$$$$$$$$$$$$$$$$$$$$$$$$$$$$$$$$$$$$$$$$$$$$$$$$$$$$
*SECTION_ALE2D
$#   secid   aleform       aet    elform
         1        11         0        14
$$$$$$$$$$$$$$$$$$$$$$$$$$$$$$$$$$$$$$$$$$$$$$$$$$$$$$$$$$$$$$$$$$$$$$$$$$$$$$$
$
$ MATERIAL PROPERTIES
$
$$$$$$$$$$$$$$$$$$$$$$$$$$$$$$$$$$$$$$$$$$$$$$$$$$$$$$$$$$$$$$$$$$$$$$$$$$$$$$$
$ rho = 125.2  kg/m^3 @ 100 bar @ 5 degrees
$ rho = 75.1  kg/m^3 @ 60 bar @ 5 degrees
$ rho = 50.1  kg/m^3 @ 40 bar @ 5 degrees
$ rho = 37.6  kg/m^3 @ 30 bar @ 5 degrees
$ rho = 25.0  kg/m^3 @ 20 bar @ 5 degrees
$ rho = 12.5  kg/m^3 @ 10 bar @ 5 degrees
$ rho = 1.27  kg/m^3 @ 1 bar @ 5 degrees
*MAT_HIGH_EXPLOSIVE_BURN
$#     mid        ro         d       pcj      beta         k         g      sigy
```

```
         1 1601.0000 8190.0000  2.80E+10     2.000     1.000     1.000     0.000
*MAT_NULL
$#     mid        ro        pc        mu     terod     cerod        ym        pr
         2  1.270000     0.000     0.000     0.000     0.000     0.000     0.000
$$$$$$$$$$$$$$$$$$$$$$$$$$$$$$$$$$$$$$$$$$$$$$$$$$$$$$$$$$$$$$$$$$$$$$$$$$$$$$$$
$
$ EQUATIONS OF STATE
$
$$$$$$$$$$$$$$$$$$$$$$$$$$$$$$$$$$$$$$$$$$$$$$$$$$$$$$$$$$$$$$$$$$$$$$$$$$$$$$$$
$ e0 = 2.5e+7  N/m^2 @ 100 bar @ 5 degrees
$ e0 = 1.5e+7  N/m^2 @ 60 bar @ 5 degrees
$ e0 = 1e+7  N/m^2 @ 40 bar @ 5 degrees
$ e0 = 7.5e+6  N/m^2 @ 30 bar @ 5 degrees
$ e0 = 5e+6  N/m^2 @ 20 bar @ 5 degrees
$ e0 = 2.5e+6  N/m^2 @ 10 bar @ 5 degrees
$ e0 = 2.5e+5  N/m^2 @ 1 bar @ 5 degrees
*EOS_JWL
$#   eosid         a         b        r1        r2      omeg        e0        vo
         15.9740E+111.3900E+10  4.500000  1.500000  0.320000    8.7E+9  1.000000
*EOS_LINEAR_POLYNOMIAL
$#   eosid        c0        c1        c2        c3        c4        c5        c6
         2     0.000     0.000     0.000     0.000  0.400000  0.400000     0.000
$#      e0        v0
 2.5000E+5     1.000
$$$$$$$$$$$$$$$$$$$$$$$$$$$$$$$$$$$$$$$$$$$$$$$$$$$$$$$$$$$$$$$$$$$$$$$$$$$$$$$$
$
$ DETONATION DESCRIPTION
$
$$$$$$$$$$$$$$$$$$$$$$$$$$$$$$$$$$$$$$$$$$$$$$$$$$$$$$$$$$$$$$$$$$$$$$$$$$$$$$$$
*INITIAL_DETONATION
$#     pid         x         y         z        lt
         0     0.000     0.000     0.000     0.000
$$$$$$$$$$$$$$$$$$$$$$$$$$$$$$$$$$$$$$$$$$$$$$$$$$$$$$$$$$$$$$$$$$$$$$$$$$$$$$$$
$
$ ALE GROUP
$
$$$$$$$$$$$$$$$$$$$$$$$$$$$$$$$$$$$$$$$$$$$$$$$$$$$$$$$$$$$$$$$$$$$$$$$$$$$$$$$$
*ALE_MULTI-MATERIAL_GROUP
$#     sid    idtype    gpname
         1         1
         2         1
$$$$$$$$$$$$$$$$$$$$$$$$$$$$$$$$$$$$$$$$$$$$$$$$$$$$$$$$$$$$$$$$$$$$$$$$$$$$$$$$
$
$ PART DESCRIPTION
$
$$$$$$$$$$$$$$$$$$$$$$$$$$$$$$$$$$$$$$$$$$$$$$$$$$$$$$$$$$$$$$$$$$$$$$$$$$$$$$$$
*PART
$# title
Explosive
$#     pid     secid       mid     eosid      hgid      grav    adpopt      tmid
         1         1         1         1         0         0         0         0
*PART
$# title
Air
$#     pid     secid       mid     eosid      hgid      grav    adpopt      tmid
         2         1         2         2         0         0         0         0
*END
```

C.3 LS-DYNA Keyword (Section 7.3.4)

```
*KEYWORD 200000000
*INCLUDE
VOLUME.k
CLAMPS.k
BOLTS.k
PLATE.k
SUPPORTS.k
*TITLE
$# title
Pressure simulation Raufoss
$$$$$$$$$$$$$$$$$$$$$$$$$$$$$$$$$$$$$$$$$$$$$$$$$$$$$$$$$$$$$$$$$$$$$$$$$$$$$$$$$$$$$$$$$$$$$
$
$ CONTROL SETTINGS
$
$$$$$$$$$$$$$$$$$$$$$$$$$$$$$$$$$$$$$$$$$$$$$$$$$$$$$$$$$$$$$$$$$$$$$$$$$$$$$$$$$$$$$$$$$$$$$
*CONTROL_ALE
$#     dct      nadv      meth      afac      bfac      cfac      dfac      efac
        -1         1        -2         0     0.000     0.000     0.000     0.000
$#   start       end     aafac     vfact      prit       ebc      pref   nsidebc
     0.000     1.000     0.000     0.000         1         0    1.0e+5         0
$#    ncpl      nbkt    imascl    checkr
         1        50         0     0.100
*CONTROL_TERMINATION
$#  endtim    endcyc     dtmin    endeng    endmas
  0.005000         0     0.000     0.000     0.000
*CONTROL_TIMESTEP
$#  dtinit    tssfac      isdo    tslimt     dt2ms      lctm     erode     ms1st
      1E-8  0.600000         0     0.000     0.000         0         0         0
$#  dt2msf   dt2mslc     imscl
     0.000         0         0
*CONTROL_SHELL
$#  wrpang     esort     irnxx    istupd    theory       bwc     miter      proj
     0.000         0         0         1         2         2         1         0
$# rotascl    intgrd    lamsht    cstyp6    tshell    nfail1    nfail4   psnfail
  1.000000         1         0         1         0         0         0         0
$# psstupd    irquad     cntco    itsflg    irquad
         0         0         0         0         2
*HOURGLASS
$#    hgid       ihq        qm       ibq        q1        q2    qb/vdc        qw
         1         1  0.001000         0  1.500000  0.060000  0.100000  0.100000
*CONTROL_ENERGY
$#    hgen      rwen    slnten     rylen
         2         2         2         2
$$$$$$$$$$$$$$$$$$$$$$$$$$$$$$$$$$$$$$$$$$$$$$$$$$$$$$$$$$$$$$$$$$$$$$$$$$$$$$$$$$$$$$$$$$$$$
$
$ OUTPUT PARAMETERS
$
$$$$$$$$$$$$$$$$$$$$$$$$$$$$$$$$$$$$$$$$$$$$$$$$$$$$$$$$$$$$$$$$$$$$$$$$$$$$$$$$$$$$$$$$$$$$$
*DATABASE_NODOUT
$#      dt    binary      lcur     ioopt      dthf     binhf
 1.0000E-7         0         0         1     0.000         0
*DATABASE_GLSTAT
$#      dt    binary      lcur     ioopt
 5.0000E-7         0         0         1
*DATABASE_MATSUM
```

```
$#      dt    binary      lcur     ioopt
 5.0000E-7         0         0         1
*DATABASE_BINARY_D3PLOT
$#      dt      lcdt      beam     npltc    psetid
 2.5000E-4         0         0         0         0
$#   ioopt
         0
*DATABASE_HISTORY_NODE
$#     id1       id2       id3       id4       id5       id6       id7       id8
      5000      5209      5189         0         0         0         0         0
$$$$$$$$$$$$$$$$$$$$$$$$$$$$$$$$$$$$$$$$$$$$$$$$$$$$$$$$$$$$$$$$$$$$$$$$$$$$$$$$$$$$$$$$$$$$$$
$
$ SECTION PROPERTIES
$
$$$$$$$$$$$$$$$$$$$$$$$$$$$$$$$$$$$$$$$$$$$$$$$$$$$$$$$$$$$$$$$$$$$$$$$$$$$$$$$$$$$$$$$$$$$$$$
*SECTION_SOLID
AIR_EXPL
$#   secid    elform
         1        11
*SECTION_SOLID_TITLE
RIGID_SUPPORTS
$#   secid    elform       aet
         2         1         0
*SECTION_SHELL_TITLE
PLATE
$#   secid    elform      shrf       nip     propt   qr/irid     icomp     setyp
         3        16  1.000000         5         1         0         0         1
$#      t1        t2        t3        t4      nloc     marea      idof    edgset
 2.0000E-3 2.0000E-3 2.0000E-3 2.0000E-3     0.000     0.000     0.000         0
*CONTACT_AUTOMATIC_SURFACE_TO_SURFACE
$#     cid                                                                 title
$#    ssid      msid     sstyp     mstyp    sboxid    mboxid       spr       mpr
        10       468         3         2         0         0         0         0
$#      fs        fd        dc        vc       vdc    penchk        bt        dt
     0.000     0.000     0.000     0.000     0.000         0     0.0001.0000E+20
$#     sfs       sfm       sst       mst      sfst      sfmt       fsf       vsf
  1.000000  1.000000     0.000     0.000  1.000000  1.000000  1.000000  1.000000
*SET_PART_LIST_TITLE
Contact_Supports_and_Clamps
$#     sid       da1       da2       da3       da4    solver
       468     0.000     0.000     0.000     0.000MECH
$#    pid1      pid2      pid3      pid4      pid5      pid6      pid7      pid8
         4         6         8         0         0         0         0         0
*SET_PART_LIST_TITLE
All_Contact
$#     sid       da1       da2       da3       da4    solver
       500     0.000     0.000     0.000     0.000MECH
$#    pid1      pid2      pid3      pid4      pid5      pid6      pid7      pid8
         4         6         8        10         0         0         0         0
*SET_SEGMENT_GENERAL_TITLE
contact_slave_segment
$#     sid       da1       da2       da3       da4    solver
        10     0.000     0.000     0.000     0.000MECH
$# option         e1        e2        e3        e4        e5        e6        e7
PART              10         0         0         0         0         0         0
*SET_SEGMENT_GENERAL_TITLE
contact_master_segment
$#     sid       da1       da2       da3       da4    solver
```

```
       468     0.000     0.000     0.000     0.000MECH
$# option         e1        e2        e3        e4        e5        e6        e7
PART               4         6         8         0         0         0         0
$$$$$$$$$$$$$$$$$$$$$$$$$$$$$$$$$$$$$$$$$$$$$$$$$$$$$$$$$$$$$$$$$$$$$$$$$$$$$$$$$$$$$$$$$$$$$
$
$ MATERIAL PROPERTIES
$
$$$$$$$$$$$$$$$$$$$$$$$$$$$$$$$$$$$$$$$$$$$$$$$$$$$$$$$$$$$$$$$$$$$$$$$$$$$$$$$$$$$$$$$$$$$$$
$ rho = 125.2  kg/m^3 @ 100 bar @ 5 degrees
$ rho = 75.1  kg/m^3 @ 60 bar @ 5 degrees
$ rho = 50.1  kg/m^3 @ 40 bar @ 5 degrees
$ rho = 37.6  kg/m^3 @ 30 bar @ 5 degrees
$ rho = 25.0  kg/m^3 @ 20 bar @ 5 degrees
$ rho = 12.5  kg/m^3 @ 10 bar @ 5 degrees
$ rho = 1.27  kg/m^3 @ 1 bar @ 5 degrees
*MAT_HIGH_EXPLOSIVE_BURN
$#     mid        ro         d       pcj      beta         k         g      sigy
         1 1601.0000 8190.0000  2.80E+10     2.000     1.000     1.000     0.000
*MAT_NULL
$#     mid        ro        pc        mu     terod     cerod        ym        pr
         2  1.270000     0.000     0.000     0.000     0.000     0.000     0.000
*MAT_RIGID_TITLE
Steel
$#     mid        ro         e        pr         n    couple         m     alias
         3 7850.00002.1000E+11  0.330000     0.000     0.000     0.000
$#     cmo      con1      con2
  1.000000         7         7
$# lco or a1      a2        a3        v1        v2        v3
     0.000     0.000     0.000     0.000     0.000     0.000
*MAT_MODIFIED_JOHNSON_COOK_TITLE
STEEL DOCOL 600DL
$#     mid        ro         e        pr      beta       xsi        cp     alpha
         4 7850.00002.1000E+11  0.330000     0.000  0.900000 452.00000 1.2000E-5
$#   e0dot        tr        tm        t0     flag1     flag2
  1.000E-3 293.00000 1800.0000 293.00000     0.000  1.000000
$#  a/siga       b/b   n/beta0   c/beta1      m/na
 2.8330E+8         0  0.000000  0.005000  1.000000
$#    q1/a      c1/n q2/alpha0 c2/alpha1
 2.6830E+8    39.380 3.9660e+8     5.000
$#   dc/dc     pd/wc     d1/na     d2/na     d3/na     d4/na     d5/na
  1.000000   7.48E+8     0.000     0.000     0.000     0.000     0.000
$#      tc      tauc
 1650.00001.0000E+20
$$$$$$$$$$$$$$$$$$$$$$$$$$$$$$$$$$$$$$$$$$$$$$$$$$$$$$$$$$$$$$$$$$$$$$$$$$$$$$$$$$$$$$$$$$$$$
$
$ EQUATIONS OF STATE
$
$$$$$$$$$$$$$$$$$$$$$$$$$$$$$$$$$$$$$$$$$$$$$$$$$$$$$$$$$$$$$$$$$$$$$$$$$$$$$$$$$$$$$$$$$$$$$
$ e0 = 2.5e+7  N/m^2 @ 100 bar @ 5 degrees
$ e0 = 1.5e+7  N/m^2 @ 60 bar @ 5 degrees
$ e0 = 1e+7  N/m^2 @ 40 bar @ 5 degrees
$ e0 = 7.5e+6  N/m^2 @ 30 bar @ 5 degrees
$ e0 = 5e+6  N/m^2 @ 20 bar @ 5 degrees
$ e0 = 2.5e+6  N/m^2 @ 10 bar @ 5 degrees
$ e0 = 2.5e+5  N/m^2 @ 1 bar @ 5 degrees
*EOS_JWL
$#   eosid         a         b        r1        r2      omeg        e0        vo
         15.9740E+111.3900E+10  4.500000  1.500000  0.320000    8.7E+9  1.000000
```

```
*EOS_LINEAR_POLYNOMIAL
$#   eosid        c0        c1        c2        c3        c4        c5        c6
         2     0.000     0.000     0.000     0.000  0.400000  0.400000     0.000
$#      e0        v0
 2.5000E+5     1.000
$$$$$$$$$$$$$$$$$$$$$$$$$$$$$$$$$$$$$$$$$$$$$$$$$$$$$$$$$$$$$$$$$$$$$$$$$$$$$$$$$$$$$$$$$$$$$
$
$   2D to 3D mapping initialization, ALE GROUP and COUPLING parameters
$
$$$$$$$$$$$$$$$$$$$$$$$$$$$$$$$$$$$$$$$$$$$$$$$$$$$$$$$$$$$$$$$$$$$$$$$$$$$$$$$$$$$$$$$$$$$$$
*INITIAL_ALE_MAPPING
100,0,200
0,0,0,300
*SET_PART
100
1,2
*SET_MULTI_MATERIAL_GROUP_LIST
200
1,2
*DEFINE_VECTOR
300,0,0,0,0,0,1
*ALE_MULTI-MATERIAL_GROUP
$#     sid    idtype    gpname
         1         1
         2         1
*CONSTRAINED_LAGRANGE_IN_SOLID
$#   slave    master     sstyp     mstyp     nquad     ctype     direc     mcoup
       500         2         0         1         3         4         2         0
$#   start       end      pfac      fric    frcmin      norm   normtyp      damp
     0.000     1.000     0.000     0.000     0.000         0         0     0.000
$#      cq      hmin      hmax     ileak     pleak   lcidpor     nvent  blockage
     0.000     0.000     0.000         1     0.100         0         0         0
$$$$$$$$$$$$$$$$$$$$$$$$$$$$$$$$$$$$$$$$$$$$$$$$$$$$$$$$$$$$$$$$$$$$$$$$$$$$$$$$$$$$$$$$$$$$$
$
$ PART DESCRIPTION
$
$$$$$$$$$$$$$$$$$$$$$$$$$$$$$$$$$$$$$$$$$$$$$$$$$$$$$$$$$$$$$$$$$$$$$$$$$$$$$$$$$$$$$$$$$$$$$
*PART
$# title
Explosive
$#     pid     secid       mid     eosid      hgid      grav    adpopt      tmid
         1         1         1         1         0         0         0         0
*PART
$# title
Air
$#     pid     secid       mid     eosid      hgid      grav    adpopt      tmid
         2         1         2         2         0         0         0         0
*PART
$# title
Supports
$#     pid     secid       mid     eosid      hgid      grav    adpopt      tmid
         4         2         3         0         0         0         0         0
*PART
$# title
Clamps
$#     pid     secid       mid     eosid      hgid      grav    adpopt      tmid
         6         2         3         0         0         0         0         0
*PART
```

```
$# title
Bolts
$#     pid     secid       mid     eosid      hgid      grav    adpopt      tmid
         8         2         3         0         0         0         0         0
*PART
$# title
Plate
$#     pid     secid       mid     eosid      hgid      grav    adpopt      tmid
        10         3         4         0         0         0         0         0
$$$$$$$$$$$$$$$$$$$$$$$$$$$$$$$$$$$$$$$$$$$$$$$$$$$$$$$$$$$$$$$$$$$$$$$$$$$$$$$$$$$$$$$$$$$$$
$
$    BOUNDARY CONDITIONS
$
$$$$$$$$$$$$$$$$$$$$$$$$$$$$$$$$$$$$$$$$$$$$$$$$$$$$$$$$$$$$$$$$$$$$$$$$$$$$$$$$$$$$$$$$$$$$$
*BOUNDARY_SPC_SET_ID
$#      id                                                               heading
         OBC_FIXED
$#    nsid       cid      dofx      dofy      dofz     dofrx     dofry     dofrz
        30         0         1         1         1         1         1         1
*SET_NODE_GENERAL_TITLE
Fixed_Supports_Clamps
$#     sid       da1       da2       da3       da4    solver
        30     0.000     0.000     0.000     0.000MECH
$# option        e1        e2        e3        e4        e5        e6        e7
PART               4         6         8         0         0         0         0
*END
```

C.4 IMPETUS Keyword (Section 7.3.5)

```
#Andersen and Hernandez Master Thesis 2013
#IMPETUS keyword example
#450mm standoff with 250 000 particles

*KEYWORD

#Include geometry from LS-DYNA
*INCLUDE
RQ_CLAMPS_2.k
*INCLUDE
RQ_PLATE_M15_2.k
*INCLUDE
RQ_SUPPORTS_2.k
*INCLUDE
RQ_BOLTS_SMALLER_CUT.k

#Define unit system
*UNIT_SYSTEM
SI

#Analysis control parameters
*TIME
[%analysis_termination_time]
*OUTPUT
[%analysis_termination_time/20],1e-5
*OUTPUT_NODE
```

```
NS,10
*SET_NODE
10,0
5278,5322

#Define parameters
*PARAMETER
analysis_termination_time=0.01 #Analysis runtime
s0=2.833e8 #Yield stress
Q1=2.683e8 #Voce coefficient Q1
Q2=3.966e8 #Voce coefficient Q2
C1=39.38 #Voce coefficient C1
C2=5.0 #Voce coefficient C2
rho_steel=7850.0 #Material density
E_steel=2.1e11 #Material elastic module
pr_steel=0.33 #Material Poisson ratio
C_mat=0.005 #Strain rate hardening parameter
ref_strainrate=0.001 #Reference strain rate
friction=0.0 #Steel-Steel friction coefficient

#Particle blast parameters
nParticles=1000000 #Number of particles
c4_length=0.13 #Height of the C4-charge
c4_radius=0.015 #Radius of the C4-charge
standoff=0.45 #Standoff
d_p_x=0 #X-coordinate of initiation point
d_p_y=0 #Y-coordinate of initiation point
d_p_z=[%standoff] #Z-coordinate of initiation point

#Define element order and symmetry axes
*CHANGE_P-ORDER
ALL,0,3
*BC_SYMMETRY
XY

#Define contact algorithm
*CONTACT
1
ALL,0,ALL,0,[%friction],-1.0e13

#Define materials
*MAT_PWL
5,[%rho_steel],[%E_steel],[%pr_steel],
1,0,0,[%C_mat],[%ref_strainrate],
*FUNCTION
1
%s0 + %Q1*(1-exp(-%C1*epsp)) + %Q2*(1-exp(-%C2*epsp))
*MAT_RIGID
1,7850
*PART
2,5
4,1
6,1
8,1
*SET_PART
1
4,6,8
```

```
#Define boundary conditions for the frame
*BC_MOTION
PS,1,XYZ,XYZ

#Particle-blast parameters
#Global domain
*GEOMETRY_BOX
2
0,0,[%standoff+%c4_radius],0.2,0.2,-0.05
#HE Domain
*GEOMETRY_CYLINDER
3
0,[-%c4_length/2],[%standoff],0,[%c4_length/2],[%standoff],[%c4_radius],0
#Define particle-blast simulation
*PBLAST
ALL,0,1,0,c4,[%nParticles/4]
1,0,1,0,0,0
2,0,3,[%d_p_x],[%d_p_y],[%standoff],0,[%analysis_termination_time]
*END
```